PHYSIK-DEPARTMENT

Spin waves in periodically patterned thin yttrium iron garnet films with lattice constants down to 100 nm produced by helium ion microscopy

Dissertation
von
Stefan Harald Matthias Mändl

TECHNISCHE UNIVERSITÄT
MÜNCHEN

Technischen Universität München
Fakultät für Physik
Lehrstuhl für Physik funktionaler Schichtsysteme, E10

Spin waves in periodically patterned thin yttrium iron garnet films with lattice constants down to 100 nm produced by helium ion microscopy

Stefan Harald Matthias Mändl

Vollständiger Abdruck der von der Fakultät für Physik der Technischen Universität München zur Erlangung des akademischen Grades eines

Doktors der Naturwissenschaften

genehmigten Dissertation.

Vorsitzender:	Prof. Dr. Frank Pollmann
Prüfer der Dissertation:	1. Prof. Dr. Dirk Grundler
	2. Prof. Dr. Peter Böni (schriftliche Beurteilung) Priv.-Doz. Dr. Christoph P. Hugenschmidt (mündliche Prüfung)

Die Dissertation wurde am 10.10.2017 bei der Technischen Universität München eingereicht und durch die Fakultät für Physik am 23.11.2017 angenommen.

Abstract

We investigate spin waves (SW) in yttrium iron garnet (YIG) films grown by liquid phase epitaxy on the waferscale. The YIG film was nanostructured using electron beam lithography and helium ion microscopy (HIM). Using HIM the minimum periodicity of the lattice was 100 nm. The decay length amounted to 0.86 mm, and we found a group velocity up to 5.4 km/s in the bare YIG film. The magnonic grating coupler effect induced by the HIM patterning allowed us to excite SWs with a wavelength down to 80 nm.

Zusammenfassung

Wir untersuchen Spin Wellen in Yttrium Eisengranat (YEG) Filmen gewachsen mit Fluessigphasen Epitaxie in Wafergroeße. Für die Nanostrukturierung haben wir Elektronenstrahl Lithographie und Helium Ionen Mikroskopie (HIM) verwendet. Die kleinste Periodizitaet war 100 nm. Die Abklinglaenge betrug 0.86 mm und die Gruppengeschwindigkeit betrug bis zu 5.4 km/s im unbehandelten YEG Film. Durch den Magnonischen Gitter Koppler Effekt konnten wir Spin Wellen mit einer minimalen Wellenlänge von 80 nm erzeugen.

Contents

1 Introduction

In the future complementary metal-oxide-semiconductor technology might face technological problems and further miniaturization of metal-oxide-semiconductor field effect transistors might be inefficient due to power dissipation problems [KBW10]. Therefore the research field of magnonics attracted a lot of interest. Magnonics might pave the road to low power consumption devices. The miniaturization is possible, because in magnonic devices the wavelength for spin waves can be tuned down to nanometer for the gigahertz (GHz) frequency range. Due to low power consumption magnonic devices can be scaled down further than electronic devices.

To most promising material for such devices up to now is yttrium iron garnet (YIG). It was recently found that thin films of the insulating ferrimagnet YIG exhibit small SW damping [HBM$^+$11, dKAB$^+$13, YdKC$^+$14, JZJ$^+$15, HRH$^+$16, LKB$^+$16, DSL$^+$17]. For a 20 nm thick YIG film a large decay length of up to 0.58 mm was found for SWs [YdKC$^+$14]. The films were produced using pulsed laser deposition (PLD) on small substrates of (111) gadolinium gallium garnet (GGG) with a lateral size of about $10\ \mathrm{mm} \times 10$ mm. Magnetic materials exhibiting low damping is important for coherent nanomagnonics, low power consumption and devices such as magnonic holography memory, non-linear cellular networks and SW interferometers [YdKC$^+$14, CVSH15, KBW10, EWKW12, GKFK15]. Further devices on the nanoscale have been proposed in Ref. [KBW$^+$08, KBL$^+$08, KNB$^+$07, KOW02] using interference effects for SW manipulation. Using nonreciprocal characteristics of SWs gives further possibilities for logic applications [JKS$^+$13]. To increase the substrate sizes, PLD is however very challenging. For large substrate sizes the growth methods of magnetron sputtering [CLZ$^+$14] and liquid phase epitaxy (LPE) [DSL$^+$17, CVvWY12] are more suitable. But up to now commercially grown YIG films using LPE had a thickness of 1 μm or beyond [SCH10] not suitable for application in nanomagnonics.

For future SW architecture three properties are of great interest: short spin-wave wavelength, large decay length and large group velocity [KBW10, GKFK15]. For the creation of SWs with short wavelengths magnonic crystals (MC) are a promising candidate. MCs consist of a magnetic material that is patterned periodically. The simplest MC is periodically patterned in one dimension. Already a lot of publications have been demonstrated the properties of such a device [WZL+09, CSHK08, Hub13, NTT01]. It was even possible to reprogram a one dimensional MC [THKG10, HSG13]. To continue the development two dimensional MCs were introduced [GZG+00, NBB+08, NDB+10]. A special type of MC is the magnonic grating-coupler (MGC) recently introduced in Ref. [YDH+13] consisting of a thin magnetic film and bi-component magnetic lattices. Using broadband spin-wave spectroscopy (BSWS) based on coplanar waveguides (CPWs), it was shown that two-dimensional (2D) periodic lattices of Permalloy (Py, $Ni_{80}Fe_{20}$) nanodisks prepared on CoFeB thin films provoked back-folding of spin-wave dispersion relations by the reciprocal lattice vector. Thereby, SWs were excited in different spatial directions with wavelengths λ that were much shorter compared to direct excitation by the same CPW. MGCs are of great interest, because MGC can be used as microwave-to-magnon transducers and are of relevance when one aims at interconnecting GHz electronics with the non-charged based logic devices explored in magnonics [KBW10]. Recently a MGC fabricated of YIG was introduced exhibiting SW wavelength of few nanometer with enlarged group velocity [YdKC+16]. In this thesis we continue with this type of device. The MGC samples are prepared from a YIG film grown at wafer-scale with LPE. The YIG film has a thickness of 200 nm providing convincing magnetic characteristics. We aim to further optimize the design of the MGC using electron beam lithography (EBL). By using helium ion microscopy (HIM) for nanostructuring we further reduced the periodicity of the magnetic lattice compared with EBL and achieved a periodicity of 100 nm. The utilization of the HIM allowed us to investigate a different type of MGC mode not investigated so far in literature to the best knowledge of the author. For the investigation of such devices BSWS is usually used for the analysis of SWs on the macroscale [KBBG02, BOFD01, CKD+04, Gie05, NDT+11, Bil07, Dür12]. For the analysis on the microscale micro-focused Brillouin light scattering (μBLS) is employed [DDH+04, DD08, DHS01, SSO+15]. By utilization of theses tools we are able to investigate SWs in the dipolar and dipole-exchange regime.

Organization of the thesis

In chapter 2 we give a introduction to the theoretical background of ferromagnetism including SW properties and basics about micro-magnetic simulations. The experimental methods and preparation techniques used throughout this thesis are described in chapter 3 and 4. In chapter 5 we present micro-magnetic simulations conducted for different structures to investigate the MGC effect on the microscale. Experiments on a 20 nm YIG film grown with PLD are presented in chapter 6. We compare the results to experiments already published in literature. In chapter 7 we investigate a bare 200 nm thick YIG film grown with LPE. SWs originating from the MGC effect are discussed in chapter 8 and 9. The SWs are generated by a nanostructured lattice using EBL [chapter 8] and HIM [chapter 9]. A summary and outlook in chapter 10 completes the thesis.

Scientific collaboration

By scientific collaboration with researchers from other universities parts of this thesis profited. The collaborating researchers are:

- 20 nm YIG thin films fabricated by Christoph Hauser and Prof. Dr. Georg Schmidt at Martin-Luther-Universität in Halle-Wittenberg, Germany. They provided high quality YIG films for nanostructuring.
- Support in fabrication of samples with HIM by Paul Seifert, Marcus Altzschner and Prof. Dr. Alexander Holleitner at Technische Universität München in München, Germany. HIM was used to fabricate nanolattices in a 200 nm thick YIG film.
- Setting up of the μBLS experiment used throughout this thesis by Dr. Vladislav Demidov at Universität Münster in Münster, Germany.

The author would like to express his gratitude to all collaborators for their support.

2 Theory

In this chapter we introduce important terms about magnetism and SWs necessary for the understanding of the results discussed in the scope of this work. We start with basic definitions and equations describing the physics of ferromagnets. Subsequent we introduce the equation of motion for SWs in a magnetic field and end up with a formalism describing properties of SWs in magnetic films. The equations are used to extract magnetic parameters and SW properties from data sets. At the end of this chapter we give an introduction about the working principle of micro-magnetic simulations performed in this thesis.

2.1 Ferro- and ferrimagnetism

Applying an external magnetic field **H** to materials leads to a magnetization **M** that is described with

$$\mathbf{M} = \overline{\overline{\chi}}\mathbf{H}. \tag{2.1}$$

Generally $\overline{\overline{\chi}}$ is a complex valued susceptibility tensor describing the anisotropic behavior of the magnetization in an external magnetic field. Assuming $\overline{\overline{\chi}} = \chi$ we can classify solid materials as shown in Tab. 2.1

The last three classes exhibit a spontaneous magnetic ordering without external magnetic field for temperature $T < T_\mathrm{c}$. T_c is a critical tempera-

Diamagnetism	$\chi < 0$
Paramagnetism	$\chi > 0$
Ferromagnetism	$\chi \gg 0$
Ferrimagnetism	$\chi \gg 0$
Antiferromagnetism	$\chi \approx 0$

Table 2.1: Classification for magnetic solids

ture and for ferromagnetic solids also known as Curie-Temperature.
Within the scope of this work we focus on ferro- and ferrimagnetic solids. In the periodic table different elements are known to be ferromagnetic: iron, nickel, cobalt and various Lanthanides. The later ones are usually neglected due to a small T_c around room temperature or lower. It is also common to use alloys made of ferromagnetic materials. The most prominent alloy is Py consisting of nickel and iron. An example for ferrimagnetic materials are the ferrits. Ferrits are composed of mainly iron oxide. The ferrimagnet we use is YIG with the elemental formula ($\mathrm{Y_3F_5O_{12}}$).
The magnetic flux **B** is described by

$$\mathbf{B} = \mu_0(\mathbf{M} + \mathbf{H}) = \mu_0(\overline{\overline{\chi}} + 1)\mathbf{H} \tag{2.2}$$

with μ_0 being the vacuum permeability. The permeability $\overline{\overline{\mu}}$ is defined by $(\overline{\overline{\chi}} + 1)$.

2.2 Total energy in ferromagnets

The total energy is crucial for the understanding of the magnetostatics and magnetodynamics in a ferromagnet. The total energy is determined by summing different interactions acting in a ferromganet. We assume in the following a magnetization **M** given by the number of magnetic moments and their enclosing volume and relate the energy terms to a mesoscopic level. Therefore theory can also be applied to ferrimagnets.

- **Exchange energy**
  The exchange energy is driven by two effects: The Coulomb interaction and the Pauli exclusion principle declaring two fermions cannot exist in the same state. The consequence becomes apparent in a hydrogen molecule. For a hydrogen molecule the parallel and antiparallel alignment of the spins have different energy levels. Together with the Heisenberg model and assuming N atoms, we obtain the following energy contribution due to exchange coupling of electrons [Aha00]:

$$E_\mathrm{ex} = -\sum_{n=\mathrm{i,j}}^{N} J_\mathrm{ij}(\mathbf{S}_\mathrm{i} \cdot \mathbf{S}_\mathrm{j}) = -2\sum_{n=\mathrm{i<j}}^{N} J_\mathrm{ij}(\mathbf{S}_\mathrm{i} \cdot \mathbf{S}_\mathrm{j}) \tag{2.3}$$

J_{ij} denotes the exchange integral. For ferromagnetic ordering $J_{\mathrm{ij}} > 0$ is valid and therefore the parallel alignment has a lower energy contribution than antiparallel alignment. In Eq. 2.3 all spins are taken into account, but the interaction decreases with increasing distance [Kit05] and only the wave functions of next neighbor show a reasonable overlap. Therefore only next neighbor are usually taken into account in Eq. 2.3 for calculation. Nevertheless due to the large magnitude of the exchange interaction we obtain a long range ordering and the so called exchange splitting of spin-up and spin-down bands.

Eq. 2.3 accounts for the quantum mechanical representation. The classical description is obtained using [HS98]

$$\epsilon_{\mathrm{ex}} = \frac{A}{V} \int dV (\nabla \mathbf{m})^2. \tag{2.4}$$

Here $\mathbf{m} = \mathbf{M}/M_{\mathrm{S}}$ indicates the normalized magnetization with M_{S} the saturation magnetization. The exchange constant A is calculated with $A = nJS^2/a$. S is the magnitude of the spin, a the lattice constant and n depends on the crystal structure [Chi99]. Eq. 2.4 is valid as long as the lengthscale is much larger than the interatomic distance.

- **Zeeman Energy**

When applying an external magnetic field $\mathbf{H}_{\mathrm{ext}}$to a ferromagnet, $\mathbf{H}_{\mathrm{ext}}$ interacts with magnetization. The energy of this interaction is described with [HS98]

$$\epsilon_{\mathrm{zee}} = -\frac{\mu_0}{V} \int dV \mathbf{M} \cdot \mathbf{H}_{\mathrm{ext}} \tag{2.5}$$

The energy contribution in Eq. 2.5 is minimized when the magnetization and the external magnetic field are aligned parallel.

- **Demagnetization field energy**

The magnetic moments interact via their dipolar field. Every magnetic moment is influenced by the dipolar field of the other magnetic moments and induces a non-local energy contribution. The so called demagnetization field H_{dem} is defined by [HS98]

$$\epsilon_{\mathrm{dem}} = -\frac{\mu_0}{2V} \int dV \mathbf{M} \cdot \mathbf{H}_{\mathrm{dem}}. \tag{2.6}$$

The effective magnetic field $\mathbf{H}_{\mathrm{dem}}$ originates from the divergence of the magnetization and can be calculated using Maxwell's equation

$$\nabla \cdot \mathbf{B} = \mu_0 \nabla \cdot (\mathbf{H}_{\mathrm{dem}} + M) = 0 \Rightarrow \nabla \cdot \mathbf{H}_{\mathrm{dem}} = -\nabla \cdot \mathbf{M}. \tag{2.7}$$

For an arbitrary body this kind of calculation can be very complicated. Therefore we assume an uniformly magnetized ellipsoid [Aha00]

$$\mathbf{H}_{\mathrm{dem}} = -\overline{\overline{N}}\mathbf{M}. \tag{2.8}$$

Here demagnetization field scales linear with the non-local demagnetization tensor $\overline{\overline{N}}$ and we can rewrite Eq. 2.6 in the following form

$$\epsilon_{\mathrm{dem}} = \frac{\mu_0}{2}\mathbf{M}\overline{\overline{N}}\mathbf{M}. \tag{2.9}$$

Without loss of generality we align the principle axes of the ellipsoid with the coordinate system to obtain the following expression

$$\overline{\overline{N}} = \begin{pmatrix} N_{\mathrm{x}} & 0 & 0 \\ 0 & N_{\mathrm{y}} & 0 \\ 0 & 0 & N_{\mathrm{z}} \end{pmatrix} \tag{2.10}$$

The tensor $\overline{\overline{N}}$ has no dimensions and the trace is $N_{\mathrm{x}} + N_{\mathrm{y}} + N_{\mathrm{z}} = 1$. In the scope of this work we mainly work with thin ferri- and ferromagnetic films. The values for a infinite thin film with the z-axis perpendicular to the film surface are: $N_{\mathrm{x}} = N_{\mathrm{y}} = 0$ and $N_{\mathrm{z}} =$

1. With this values the demagnetization field and the energy density simplifies to

$$\mathbf{H}_{\mathrm{dem}} = -\mathbf{e}_{\mathrm{z}}(\mathbf{e}_{\mathrm{z}} \cdot \mathbf{M}); \epsilon = \frac{\mu_0}{2}(\mathbf{e}_{\mathrm{z}} \cdot \mathbf{M})^2. \tag{2.11}$$

The vector $\mathbf{e}_{\mathrm{z}}$ is the unit vector along the z axis.

Adding up the different contributions of the energy we obtain the total energy density

$$\epsilon_{\mathrm{tot}} = \epsilon_{\mathrm{ex}} + \epsilon_{\mathrm{zee}} + \epsilon_{\mathrm{dem}}. \tag{2.12}$$

Minimization of the total energy density can be used to calculate the magnetostatic equilibrium and therefore the configuration of the magnetic moments. Further we can calculate the effective magnetic field H_{eff} [Gil55, Gil04]

$$\mathbf{H}_{\mathrm{eff}} = -\frac{1}{\mu_0}\nabla_{\mathbf{M}}\epsilon_{\mathrm{tot}}. \tag{2.13}$$

The effective magnetic field H_{eff} is calculated, because the magnetization precesses around the axis of H_{eff}, as we show in the next section.

2.3 Magnetization dynamics

In the last section we introduced all important parameters to define the magnetostatic equilibrium configuration of the magnetization in a ferri- or ferromagnet. The dynamic properties of the magnetization can be described by the Landau Lifshitz (LL) equation [LL35]

$$\frac{\partial \mathbf{M}}{\partial t} = -\gamma\mu_0 \mathbf{M} \times \mathbf{H}_{\mathrm{eff}} - \frac{\lambda}{M_{\mathrm{S}}^2}\mathbf{M} \times (\mathbf{M} \times \mathbf{H}_{\mathrm{eff}}) \tag{2.14}$$

with $\gamma = g|e|/(2m_e)$ the gyromagnetic ratio, m_{e} and e are the mass and the charge of the electron and g is the g-factor. A phenomenological damping is introduced with λ. Equation 2.14 describes a torque equation of motion. From this equation a precessional motion of the magnetization follows. The more common representation of the LL equation is the so called Landau-Lifshitz-Gilbert (LLG) equation [Gil55]

$$\frac{\partial \mathbf{M}}{\partial t} = -\gamma\mu_0 \mathbf{M} \times \mathbf{H}_{\text{eff}} + \frac{\alpha}{M_S}(\mathbf{M} \times \frac{\partial \mathbf{M}}{\partial t}). \tag{2.15}$$

Here α describes the phenomenological damping with $\lambda = \alpha\gamma\mu_0 M_{\text{S}}$. But we note that this accounts only for small α. Important to mention is that the LL equation leaves the length of the vector **M** unchanged. By scalar multiplication of both sides with **M** gives $\frac{\partial}{\partial t}\mathbf{M}^2 = 0$.

2.3.1 Dynamic susceptibility

Now we discuss a solution for Eq. 2.15 assuming distinct conditions [Bil07], because it exists no analytical solution in general form.

1. Infinite extended film in x-y plane with $N_{\text{x}} = N_{\text{y}} = 0$ and $N_{\text{z}} = 1$.
2. Homogeneous external magnetic field $\mathbf{H} = H\mathbf{e}_{\text{y}}$ applied along *y* axis.
3. Additional to **H** a uniform excitation field $\mathbf{h} = h\mathbf{e}_{\text{x}}$ is applied and thus perpendicular to H. We assume $\mathbf{h} \ll \mathbf{H}$.
4. Uniform magnetization aligned with **H**.
5. The change of the length of **M** due to precession can be neglected $|\mathbf{m}| \ll |\mathbf{M}|$.
6. We do not allow spatial variation of the magnetization and assume the macrospin model [MAT02].

The excitation leads to a precessing **M**. Due to $|\mathbf{m}| \ll |\mathbf{M}|$ we can write $M \approx m_{\text{x}}\mathbf{e}_{\text{x}} + M_{\text{S}}\mathbf{e}_{\text{y}} + m_{\text{z}}\mathbf{e}_{\text{z}}$ and split the magnetization into a static and dynamic part. Combining this assumption with Eq. 2.15 we obtain the following set of coupled linear differential equations

$$\begin{aligned} (\omega_{\text{H}} + i\alpha\omega)\tilde{m}_{\text{x}} - i\omega\tilde{m}_{\text{z}} &= \omega_{\text{M}}\tilde{h}_{\text{x}} \\ (\omega_{\text{H}} + i\alpha\omega + \omega_{\text{M}})\tilde{m}_{\text{z}} + i\omega\tilde{m}_{\text{x}} &= 0 \end{aligned} \tag{2.16}$$

We made the following definitions and assumptions:

1. $\omega_{\text{M}} = \mu_0\gamma M_{\text{S}}$; $\omega_{\text{H}} = \mu_0\gamma H$

2. Oscillating motion of $m_\mathrm{i} = \mathcal{R}(\tilde{m}_\mathrm{i} e^{i\omega t})$ induced by the excitation field $h_\mathrm{i} = \mathcal{R}(\tilde{h}_\mathrm{i} e^{i\omega t})$

For convenience Eq. 2.16 is depicted in matrix form

$$\begin{pmatrix} \omega_\mathrm{H} + i\alpha\omega & -i\omega \\ i\omega & \omega_H + i\alpha\omega + \omega_\mathrm{M} \end{pmatrix} \begin{pmatrix} \tilde{m}_\mathrm{x} \\ \tilde{m}_\mathrm{z} \end{pmatrix} = \begin{pmatrix} \tilde{h} \\ 0 \end{pmatrix} \omega_M \tag{2.17}$$

The dynamic magnetization is coupled with the complex valued high frequency susceptibility to the dynamic magnetic field [Pol48]

$$\begin{pmatrix} \tilde{m}_x \\ \tilde{m}_z \end{pmatrix} = \mathbf{m} = \overline{\overline{\chi}}\mathbf{h} = \begin{pmatrix} \chi_\mathrm{xx} & \chi_\mathrm{xz} \\ \chi_\mathrm{zx} & \chi_\mathrm{zz} \end{pmatrix} \begin{pmatrix} \tilde{h} \\ 0 \end{pmatrix} \tag{2.18}$$

By making use of Eq. 2.18 we find for the susceptibility $\overline{\overline{\chi}}$:

$$\begin{aligned} \overline{\overline{\chi}} = & \frac{\omega_\mathrm{M}}{\omega_\mathrm{H}(\omega_\mathrm{M} + \omega_\mathrm{H}) - \omega^2 + i\alpha\omega(\omega_\mathrm{M} + 2\omega_\mathrm{H})} \times \\ & \begin{pmatrix} \omega_\mathrm{H} + \omega_\mathrm{M} + i\alpha\omega & i\omega \\ -i\omega & \omega_\mathrm{H} + i\alpha\omega \end{pmatrix} \end{aligned} \tag{2.19}$$

From Eq. 2.19 we obtain the components $\overline{\overline{\chi'}}$ and $\overline{\overline{\chi''}}$ defined as the real and imaginary part, respectively, of $\overline{\overline{\chi}}$ [Bil07]:

$$\begin{aligned} {\chi'}_\mathrm{xx} &= \frac{\omega_\mathrm{M}(\omega_\mathrm{H} + \omega_\mathrm{M})(\omega_\mathrm{res}^2 - \omega^2)}{(\omega_\mathrm{res}^2 - \omega^2)^2 + \alpha^2\omega^2(2\omega_\mathrm{H} + \omega_\mathrm{M})^2} \\ {\chi''}_\mathrm{xx} &= \frac{\alpha\omega\omega_\mathrm{M}[\omega^2 + (\omega_\mathrm{M} + \omega_\mathrm{H})^2]}{(\omega_\mathrm{res}^2 - \omega^2)^2 + \alpha^2\omega^2(2\omega_\mathrm{H} + \omega_\mathrm{M})^2} \end{aligned} \tag{2.20}$$

where ω_res indicates the resonance frequency

$$\omega_\mathrm{res}^2 = \omega_\mathrm{H}(\omega_\mathrm{M} + \omega_\mathrm{H}). \tag{2.21}$$

A more detailed calculation of the susceptibility is found in Ref. [Bil07]. Similar to $\overline{\overline{\chi}}_\mathrm{xx}$ we can also calculate the other components of the susceptibility [Bil07]:

$$\begin{aligned} {\chi'}_{\mathrm{xz}} = \chi'_{\mathrm{zx}} &= \frac{\alpha\omega\omega_{\mathrm{M}}(\omega_{\mathrm{M}}+2\omega_{\mathrm{H}})^2}{(\omega_{\mathrm{res}}^2-\omega^2)^2+\alpha^2\omega^2(2\omega_{\mathrm{H}}+\omega_{\mathrm{M}})^2} \\ {\chi''}_{\mathrm{xz}} = \chi''_{\mathrm{zx}} &= \frac{\omega\omega_{\mathrm{M}}(\omega_{\mathrm{res}}^2-\omega^2)}{(\omega_{\mathrm{res}}^2-\omega^2)^2+\alpha^2\omega^2(2\omega_{\mathrm{H}}+\omega_{\mathrm{M}})^2} \end{aligned} \tag{2.22}$$

$$\begin{aligned} {\chi'}_{\mathrm{zz}} &= \frac{\omega_{\mathrm{M}}\omega_{\mathrm{H}}(\omega_{\mathrm{res}}^2-\omega^2)}{(\omega_{\mathrm{res}}^2-\omega^2)^2+\alpha^2\omega^2(2\omega_{\mathrm{H}}+\omega_{\mathrm{M}})^2} \\ {\chi''}_{\mathrm{zz}} &= \frac{\alpha\omega\omega_{\mathrm{M}}(\omega^2+{\omega_{\mathrm{H}}}^2)}{(\omega_{\mathrm{res}}^2-\omega^2)^2+\alpha^2\omega^2(2\omega_{\mathrm{H}}+\omega_{\mathrm{M}})^2} \end{aligned} \tag{2.23}$$

Knowing all components of the susceptibility allows for the calculation of the ellipticity [Bil07]. Therefore we can correlate the maxima of m_{x} and m_{z}

$$\frac{\max[m_{\mathrm{x}}(t)]}{\max[m_{\mathrm{z}}(t)]} = \frac{\max[\mathcal{R}(m_{\mathrm{x}}e^{i\omega t})]}{\max[\mathcal{R}(m_{\mathrm{z}}e^{i\omega t})]} = \frac{|m_{\mathrm{x}}|}{|m_{\mathrm{z}}|} = \frac{|\chi_{\mathrm{xx}}|}{|\chi_{\mathrm{zx}}|} \approx \frac{\omega_{\mathrm{H}}+\omega_{\mathrm{M}}}{\omega} \tag{2.24}$$

The out-of-plane component m_{z} increases for increasing excitation frequency, but at resonance frequency the in-plane component m_{x} is larger. The imaginary part of the susceptibility ${\chi''}_{\mathrm{xx}}$ has a line shape that can be approximated by a Lorentzian function. The function has a maximum at ω_{res}. The full width at half maximum (FWHM) of ${\chi''}_{\mathrm{xx}}$ defines the frequency linewidth by [Bil07]

$$\Delta\omega = \alpha(2\omega_H+\omega_M). \tag{2.25}$$

2.3.2 Kittel equation

We derived the equation for the ferromagnetic resonance (FMR) for the case of an infinite film. Using Eq. 2.8 for calculation of the susceptibility we obtain for the resonance frequency

$$f_{\mathrm{res}} = \frac{1}{2\pi}\gamma\mu_0\sqrt{[H+(N_{\mathrm{y}}-N_{\mathrm{x}})M_{\mathrm{S}}][H+(N_{\mathrm{z}}-N_{\mathrm{x}})M_{\mathrm{S}}]}. \tag{2.26}$$

This equations correlates a magnetic body of ellipsoidal shape to the resonance frequency [Kit48].

2.3.3 Spin-waves in thin films

In the last sections we derived the properties of a uniform precessing magnetization. All magnetic moments are in-phase and therefore the uniform precession is described with an infinite wavelength $\lambda \to \infty$ or wave vector $k = 0$. Taking small wave vectors into account the spin waves are dominated by dipolar interaction. This SWs can be described in the magnetostatic limit using Maxwell equations assuming the absence of currents [Sta93]:

$$\nabla \times \mathbf{H} = 0, \nabla \cdot \mathbf{B} = 0, \nabla \times \mathbf{E} = -\dot{B}. \tag{2.27}$$

We define the magnetostatic scalar potential ψ with $\mathbf{H} = -\nabla\psi$. Using the definition of **B** in Eq. 2.2 we can derive Waklers's equation [Wal57]:

$$(1+\chi)\left[\frac{\partial\psi}{\partial x^2} + \frac{\partial\psi}{\partial y^2}\right] + \frac{\partial\psi}{\partial z^2} = 0. \tag{2.28}$$

To obtain a dispersion relation we assume an uniform plane wave propagation with $\psi \propto e^{i\mathbf{k}\cdot\mathbf{r}}$. This leads to

$$(1+\chi)({k^2}_x + {k^2}_y) + {k^2}_z = 0. \tag{2.29}$$

Equation 2.29 assigns the wave vector with the frequency, because χ depends on the frequency. For a more detailed description we recommend Ref. [Wal57].

A more general description of SWs was developed by Kalinikos and Slavin [KS86] for an arbitrary wave vector **k** assuming an infinite extended magnetic film with thickness t. This formalism contains both dipolar and exchange interaction. The wave vector consists of an out-of-plane component κ_p

$$\kappa_\mathrm{p} = \frac{p\pi}{t}, p = 0, 1, 2, ... \tag{2.30}$$

referred to as perpendicular standing spin wave (PSSW) and an in-plane component k_ζ so that $k = k_\zeta + \kappa_\mathrm{p}$. The in-plane component is decomposed in two further components parallel and perpendicular to the in-plane magnetization $k_\zeta = k_{\|} + k_\perp$. Equation 2.31 to 2.33 describe the dispersion relation for the magnetization aligned with the surface of the magnetic film and without damping:

$$\omega_{\mathrm{res}}^2(k, H)|_{\mathrm{p}} = (\omega_{\mathrm{H}} + A_{\mathrm{ex}}\omega_{\mathrm{M}}k^2)[\omega_{\mathrm{H}} + \omega_{\mathrm{M}}(A_{\mathrm{ex}}k^2 + F_{\mathrm{pp}}(k))]. \quad (2.31)$$

For large wave vectors the SWs are dominated by the exchange term $A_{\mathrm{ex}}k^2$. But for small wave vectors this contribution is small. Then the dipolar interaction dominates described by $F_{\mathrm{pp}}(k)$.

$$F_{\mathrm{pp}}(k) = 1 - P_{\mathrm{pp}}cos\vartheta^2 + \omega_{\mathrm{M}}\frac{P_{\mathrm{pp}}(1 - P_{\mathrm{pp}})sin\vartheta^2}{\omega_{\mathrm{H}} + A_{\mathrm{ex}}\omega_{\mathrm{M}}k^2}. \quad (2.32)$$

These SWs are called magnetostatic waves. In Eq. 2.32 ϑ is defined as the in-plane angle enclosed by the wave vector of the SW and the magnetization. The term P_{pp} is calculated following

$$P_{\mathrm{pp}} = \frac{k_\zeta^2}{k^2} - \frac{2k_\zeta^3}{tk^4}\frac{1}{1 + \delta_{0\mathrm{p}}}[1 - (-1)^p exp(-k_\zeta t)]. \quad (2.33)$$

For small wave vectors we give three different configurations for magnetostatic SWs [Sta93]. The wave vector is in the sample plane for these configurations.

For the magnetostatic surface wave (MSSW) configuration the in-plane wave vector is perpendicular to the magnetization. As the name already indicates the SW amplitude is highest on the surface and decays exponentially. The dispersion relation is described with [Sta93]

$$\omega_{\mathrm{MSSW}}{}^2 = \omega_H(\omega_H + \omega_M) + \frac{\omega_M{}^2}{4}(1 - exp(-2k_\perp d)). \quad (2.34)$$

Damon and Eshbach were the first describing this SW mode [DE61].

For the magnetostatic backward volume wave (MSBVW) the wave vector and the magnetization are aligned parallel. This SW mode shows a phase and a group velocity with opposing direction. The dispersion relation is described with [Sta93]

$$\omega_{\mathrm{MSBVW}}{}^2 = \omega_H[\omega_H + \omega_M(\frac{1 - exp(-k_{\|}d)}{k_{\|}d})]. \tag{2.35}$$

If the magnetization is parallel to the normal of the sample surface the dispersion relation of magnetostatic forward volume wave (MSFVW) can be described using [Sta93]

$$\omega^2_{\mathrm{MSFVW}} = \omega_{\mathrm{H}}[\omega_{\mathrm{H}} + \omega_{\mathrm{M}}(1 - \frac{1 - exp(-k_{\zeta}d)}{k_{\zeta}t})]. \tag{2.36}$$

For this type of SW the properties do not depend on the direction of the wave vector k_{ζ}. Assuming in Eq. 2.36 that $k_{\zeta} \to 0$ and $H \geq M_{\mathrm{S}}$ we obtain

$$\omega_{\mathrm{MSFVW}} = \omega_{\mathrm{H}} = \mu_0\gamma(H - M_{\mathrm{S}}). \tag{2.37}$$

In case of $H < M_{\mathrm{S}}$ the ground state of the magnetization changes continuously with the applied magnetic field.
The group velocity v_{g} of SWs is defined with

$$v_{\mathrm{g}} = \frac{\partial\omega}{\partial k}. \tag{2.38}$$

In Fig. 2.1 we show the dispersion relation for $\vartheta = 0$ deg (MSBVW) and $\vartheta = 90$ deg (MSSW) and the corresponding group velocity. The decay length l_{d} for propagating SWs is defined as follows

$$l_{\mathrm{d}} = v_{\mathrm{g}}\tau \tag{2.39}$$

with τ the relaxation time.

2.3.4 Parallel parametric pumping

The process of parallel parametric pumping occurs when energy is transferred parallel to the magnetization. For parallel parametric pumping the exciting alternating magnetic field needs to be frequency doubled. The physical process of parallel parametric pumping can be imagined as a photon that creates two SWs. Due to energy and momentum conservation the following relation applies [SCH10]:

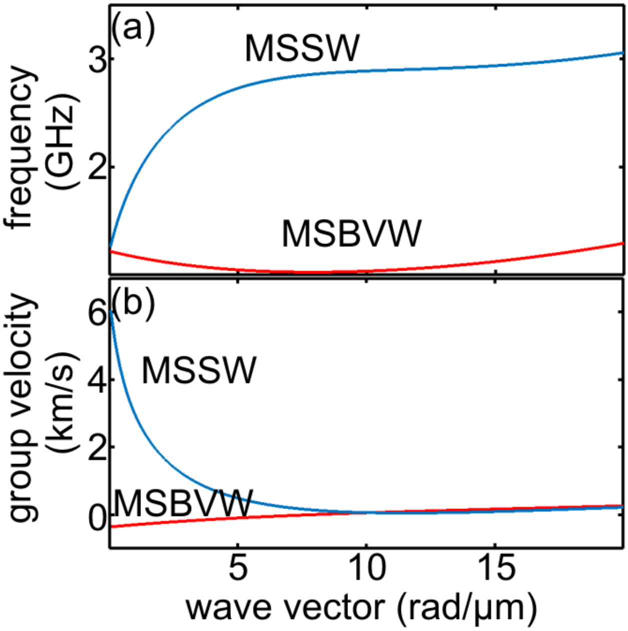

Figure 2.1: (a) Dispersion relation for MSSW and MSBVW configuration calculated with the formalism of Ref. [KS86]. (b) Group velocity for MSSW and MSBVW configuration. We applied $M_{\mathrm{S}} = 140$ kA/m, $A = 3.32 \cdot 10^{-12}$ J/m, $t = 200$ nm and $\mu_0 H = 10$ mT.

$$\begin{aligned} f_{\mathrm{m1}} + f_{\mathrm{m2}} &= f_{\mathrm{pu}} \\ k_{\mathrm{m1}} + k_{\mathrm{m2}} &= k_{\mathrm{pu}} \end{aligned} \tag{2.40}$$

with $f_{\mathrm{m1}}, f_{\mathrm{m2}}$ and $k_{\mathrm{m1}}, k_{\mathrm{m2}}$ the frequency and wave vector of the two SWs. The energy and momentum of the pumping system is described with $f_{\mathrm{pu}}, k_{\mathrm{pu}}$. The most simple case occurs when $f_{\mathrm{m1}} = f_{\mathrm{m2}} = f_{\mathrm{pu}}/2$. For the wave vector of the SW we approximate $k_{\mathrm{m1}} = -k_{\mathrm{m2}}$, because the wave vector of the photon is small compared to the wave vector of the SW $k_{\mathrm{pu}} \ll k_{\mathrm{m1}}, k_{\mathrm{m2}}$ [SCH10]. More details to parallel parametric pumping are given in Ref. [GM96].

Following this approach for parallel parametric pumping we will calculate the pump frequency in the next sections using the equation:

$$f_{\mathrm{p}u} = \omega^2_{\mathrm{res}}/2\pi + \omega^2_{\mathrm{res}}/2\pi \tag{2.41}$$

where ω^2_{res} is taken from Eq. 2.31. We point out that parallel parametric pumping is also found for PSSW modes [SCA$^+$07].

2.3.5 Calculation of nonreciprocity of magnetic thin film combined with an antenna

For the calculation of the intrinsic nonreciprocity of the magnetic thin film we applied equation (6) of Ref. [MVC$^+$06]:

$$m_r(z) = m_l(-z) = \zeta e^{kz} - e^{-kz} \tag{2.42}$$

$$\zeta = \sqrt{\frac{\omega_{max} + \omega_k}{\omega_{max} - \omega_k}} \tag{2.43}$$

$$\omega^2_k = \omega^2_{max} - (\frac{\omega_M}{2})^2 e^{-2kd} \tag{2.44}$$

using the definitions $\omega_{max} = \omega_H + \frac{\omega_{M_{\mathrm{s}}}}{2}$ and $\omega_H = \gamma\mu_0 H, \omega_{M_{\mathrm{s}}} = \gamma\mu_0 M_{\mathrm{s}}$ (H is the external magnetic field and M_{s} is the saturation magnetization). To obtain the amplitudes at the surfaces of the film we set $d/2$ and $-d/2$ for z.

For the calculation of the nonreciprocity c of the SW excitation by the CPW we applied equation (1) of Ref. [DKR$^+$09] in combination with the formalism of Ref. [KS86] to calculate the resonance frequency f:

$$c_{l\backslash r} = [\frac{f}{\gamma} \pm \frac{1}{M_{\mathrm{s}}}(H^2 - \frac{f^2}{\gamma^2})]. \tag{2.45}$$

We assume that dynamic components pointing to the left (l) or right (r) hand side interfere destructively or constructively, respectively. For calculation of the combined nonreciprocity we applied the following equation:

$$\beta_{\mathrm{l}\backslash\mathrm{r}} = \frac{c_{\mathrm{l}\backslash\mathrm{r}} m_{\mathrm{l}\backslash\mathrm{r}}}{c_{\mathrm{l}\backslash\mathrm{r}} m_{\mathrm{l}\backslash\mathrm{r}} + c_{\mathrm{r}\backslash\mathrm{l}} m_{\mathrm{r}\backslash\mathrm{l}}} \tag{2.46}$$

Using this notation, we implicate that the intrinsic nonreciprocity of the magnetic film and the nonreciprocity originating of the CPW have the same symmetry. This is taken from a microscopic analysis and in agreement with Ref. [SYS$^+$10].

2.3.6 Empty lattice model

The empty lattice model is already used for decades in physics, in the beginning to calculate electronic bands [Sla34]. We employ the empty lattice model to calculate the energies of SWs in a magnetic film induced by a magnetic lattice. The authors in Ref. [YDH$^+$13] already used this formalism in magnonics.
At first we assume the dispersion relation for a MSSW as in Fig. 2.1 (a). In the empty lattice model the dispersion relation is back-folded by the reciprocal lattice vector **G**. We illustrate the empty lattice model for a magnetic film with a lattice in one dimension. For the periodicity a we choose 700 nm corresponding to a reciprocal lattice vector of $G_\mathrm{i} = i \cdot 9$ rad/μm with $i = 0, 1, ...$ We have chosen 700 nm, because we use this value for samples investigated in simulation and experiment. The resulting band structure is depicted in Fig. 2.2 (a). In Fig. 2.2 (b) we show the reduced zone scheme. The blue line depicts a wave vector of $k_\mathrm{I} = 0.9$ rad/μm used in experiment (section 3.1.5) to excite the magnetic film and the magnetic lattice. Due to the backfolding several SWs are excited along the arbitrary wave vector.

For the empty lattice model the 'full' wave vector of the SW **k** is composed of three individual parts:

1. The wave vector $\mathbf{k}_\zeta$ aligned parallel to the sample surface.
2. The 2D reciprocal lattice vector $\mathbf{G}_\mathrm{ij} = \sqrt{(i \cdot 2\pi/a_\mathrm{x})^2 + (j \cdot 2\pi/a_\mathrm{y})^2}$ with $i, j \in \mathbb{N}$ aligned parallel to the sample surface. We define that G_i0 points along the *x* axis and G_{0j} along the *y* axis.
3. The wave vector $\boldsymbol{\kappa}_\mathrm{p}$ defined in Eq. 2.30 is pointing out-of-plane.

The definitions of the directions of the wave vectors are depicted in Fig. 2.3. To obtain the 'full' wave vector one has to use vector addition and take into account the orientation of the individual wave vectors $\mathbf{k}_\zeta$, $\mathbf{G}_\mathrm{ij}$ and $\boldsymbol{\kappa}_\mathrm{p}$. Due to the out-of-plane component $\boldsymbol{\kappa}_\mathrm{p}$ the 'full' wave vector can be rotated out-of-plane denoted by the angle γ [Fig. 2.3]. For completeness the reciprocal lattice vector G_{00} is defined with the value 0 rad/μm within this thesis.

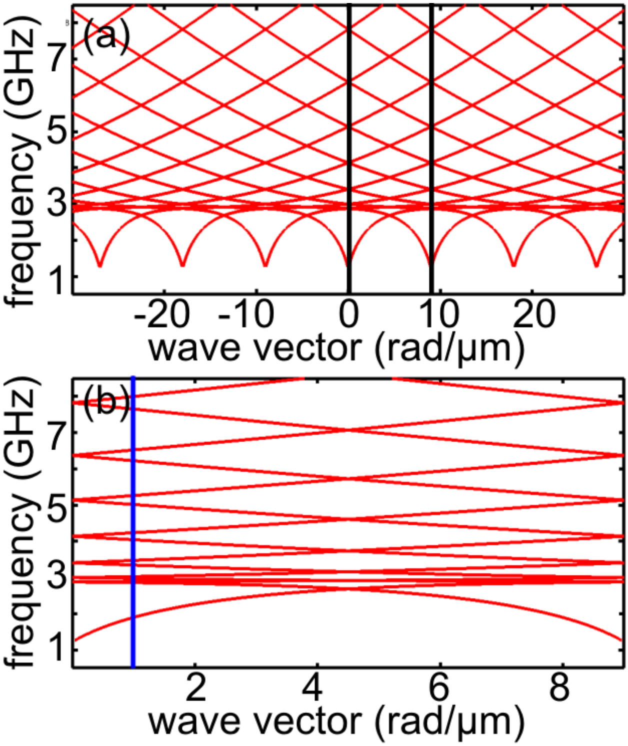

Figure 2.2: (a) Band structure for MSSW configuration calculated with the formalism in Ref. [KS86] and assuming $G_\mathrm{i} = i \cdot 9$ rad/μm with $i = -10, -9, ..., 9, 10$. (b) Reduced zone scheme for band structure extracted from (a) between the black lines. The blue line depicts a wave vector $k_\mathrm{I} = 0.9$ rad/μm used in experiment (section 3.1.5). We applied $M_\mathrm{S} = 140$ kA/m, $A = 3.32 \cdot 10^{-12}$ J/m, $t = 200$ nm and $\mu_0 H = 10$ mT.

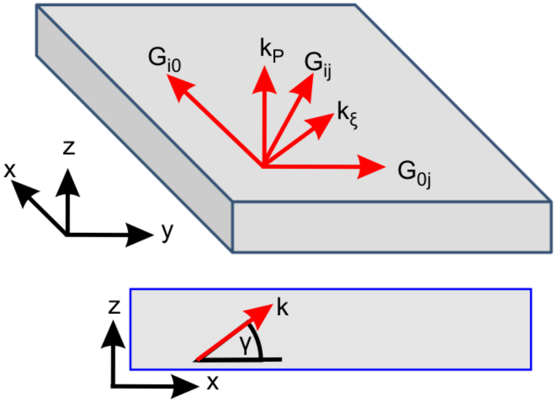

Figure 2.3: Definition of orientation of different wave vectors: $\mathbf{k}_\varsigma$ (in-plane), reciprocal lattice vectors $\mathbf{G}_\mathrm{ij}$, G_i0, G_0j (in-plane), $\boldsymbol{\kappa}_\mathrm{p}$ (out-of-plane). If $\boldsymbol{\kappa}_\mathrm{p} \neq 0$ the 'full' wave vector points out-of-plane denoted by the angle γ. The definition is used in chapter 9.

2.4 Micro-magnetic simulation

Throughout this work micro-magnetic simulations are applied to provide insight to the physical properties of SWs on the microscale. We use the software package MicroMagus [BG]. This tool allows to calculate the ferromagnetic ground state and simulate the dynamic properties of propagating SWs. It is also possible to include a ferromagnetic lattice due to periodic boundary conditions. To conduct the simulations the structure is subdivided in a mesh of N cells. Each cell from $i = 1, .., N$ contains an uniform magnetization vector $\mathbf{M}_\mathrm{i}$ and effective magnetic field $\mathbf{H}_\mathrm{eff,i}$.

2.4.1 Magnetostatic configuration

To obtain the magnetostatic configuration the total energy of each cell is minimized. We obtain a minimum if $\mathbf{M}_\mathrm{i}$ and $\mathbf{H}_\mathrm{eff,i}$ are collinear in the N cells

$$\mathbf{H}_\mathrm{eff,i} \times \mathbf{M}_\mathrm{i} = 0 \tag{2.47}$$

This is obtained by integrating the LLG equation 2.15 for each cell. Doing so we calculate the integral torque and compare the result to a certain threshold value. For an integral torque below the threshold value we obtain the equilibrium configuration.

2.4.2 Magnetodynamic behavior

The magnetostatic configuration in section 2.4.1 is used as initial configuration for the magnetodynamic simulations. We apply a magnetic field pulse or a oscillating dynamic magnetic field to disturb the magnetization of L cells with $(L \leq N)$. Due to the excitation the magnetization $\mathbf{M}_\mathrm{i}$ precesses around $\mathbf{H}_{\mathrm{eff},\mathrm{i}}$ with damping included and relaxes towards equilibrium configuration. Using discrete time steps of few picoseconds the precession of the magnetization $\mathbf{M}_\mathrm{i}(\mathbf{r}, t)$ in each cell is simulated. We apply a least-squares spectral analysis (Lomb method) to evaluate the frequency spectrum $P(f, \mathbf{r})$, because of uneven temporal spacing of the data. Finally we analyze the out-of-plane component of the discrete cells.

2.4.3 Excitation parameter and geometric layout of micro-magnetic simulations

In this section we describe the excitation parameter and geometric layout used for micro-magnetic simulations.
The static magnetic field is applied in the sample plane. The in-plane component of the dynamic magnetic field is applied perpendicular to the static magnetic field. The applied out-of-plane component has the same value as the in-plane component. Thus the dynamic magnetic field is pointing 45 deg out-of-plane.
In Fig. 2.4 we show how the investigated area is subdivided in the direction of the different axes. The pixel edge length in x and y direction is 5.5 nm. In z direction the pixel edge length varies between 5 and 80 nm and the number of pixels in z direction varies between 3 and 5 for the different simulations. The damping α was set to 0.0001. The investigated area is continued by periodic boundary conditions and we used a periodicity of 700 nm for the magnetic disks. For the gyromagnetic ratio the value $\gamma/2\pi$ = 28.5 GHz/T is set by MicroMagus and cannot be changed.

Now we define so called simulation types used to perform the micro-magnetic simulation:

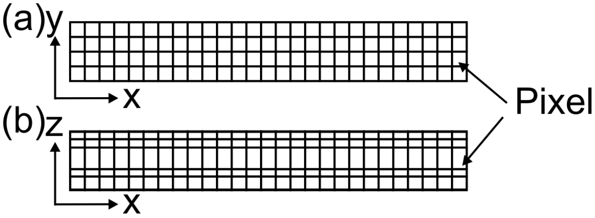

Figure 2.4: In (a) and (b) we show how the area investigated is subdivided by pixels in the direction of the different axes. The pixel edge length in *x* and *y* direction is 5.5 nm. In *z* direction the pixel edge length varies between 5 and 80 nm and the number of pixels in *z* direction varies between 3 and 5 for the different simulations.

Simu1 The investigated area has a size of 0.7 x 0.7 μm^2 subdivided by 128 x 128 pixel in *x*-*y* direction containing one magnetic disk. A sketch of the structure is shown in Fig. 2.5 (a). We use a magnetic field pulse with a maximum amplitude of 8.0 mT homogenous distributed over the whole sample area to excite SW dynamics [green cuboid in Fig. 2.5 (a)]. Within the micro-magnetic simulation the SWs precession is simulated for a timescale of 6 ns.

Simu2 The investigated area has a size of 22.4 x 0.7 μm^2 subdivided by 4096 x 128 pixel in *x*-*y* direction. We use a dynamic magnetic field spatial confined in one direction to 1.75 μm highlighted by a green cuboid in Fig. 2.5 (b) and (c). Due to enlarged geometry propagating SWs can be studied. For the excitation we use either a constant oscillating dynamic magnetic field or a dynamic magnetic field pulse with an amplitude of 0.28 mT to excite SW dynamics. Within the micro-magnetic simulation the SWs propagation is simulated for a timescale of 10 ns. The SWs are excited at 0 ns and we take a snapshot at 10 ns for data evaluation.

To perform simulation with spatial confined dynamic magnetic field we use different geometries [Fig. 2.5 (b) and (c)]. The structure in Fig. 2.5 (c) is subdivided in 2 region. Region 1 consists of a thin film with magnetic disks and region 2 of a bare magnetic film. The transition region between region 1 and 2 is termed as SW interface for the following chapters. This accounts also for experimental results.

Simu2a We study propagating SWs in a MGC. In this case the ge-

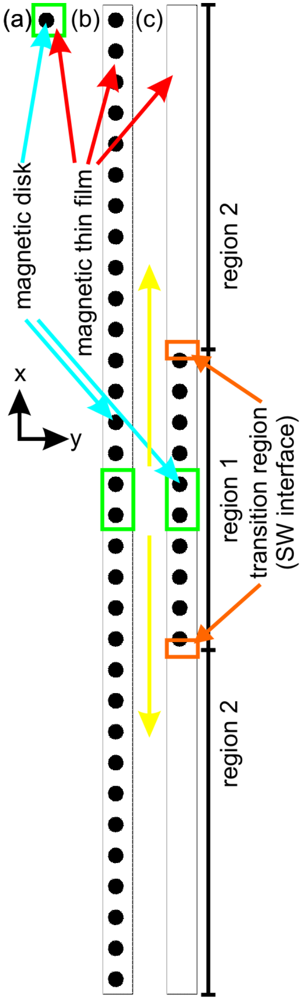

Figure 2.5: Sketch of the different simulation geometries used throughout this chapter. The depicted geometries are continued by periodic boundary conditions. (a) Simulation geometry used for the magnetic field pulse. (b) and (c) Simulation geometry used for oscillating dynamic magnetic field and magnetic field pulse. The yellow arrows show the propagation direction of the SWs. In (b) we use 32 magnetic disks to simulate a MGC and in (c) we use 10 magnetic disks to simulate the transition of MGC to a bare magnetic film. The structure in (c) is subdivided in 2 region. Region 1 consists of a thin film with magnetic disks and region 2 of a bare magnetic film. The transition region between region 1 and 2 is termed as SW interface.

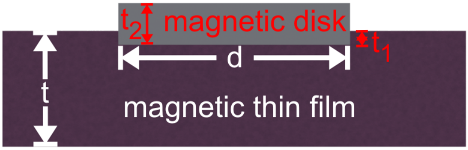

Figure 2.6: Basic sketch of the sample geometry defining important parameters.

ometry contains 32 magnetic disks. A sketch of the structure is shown in Fig. 2.5 (b).

Simu2b We study propagating SWs at the transition of a MGC and a magnetic thin film. The transition region is defined as SW interface for the following chapters. In this case the geometric structure contains 10 magnetic disks. A sketch of the structure is shown in Fig. 2.5 (c).

Simu2c We apply a dynamic magnetic field pulse. The geometry contains 32 magnetic disks. A sketch of the structure is shown in Fig. 2.5 (b).

2.4.4 Geometric and magnetic parameters

In chapter 5 simulations for two different sets of geometric and magnetic parameters will be presented. The two different sets of geometric and magnetic parameters are given here:

Set1 Geometric parameters: $t = 200$ nm, $t_1 = 5$ nm, $t_2 = 15$ nm, $d = 350$ nm and periodicity $a = 700$ nm [Fig. 2.6].
Magnetic parameters of the thin film: saturation magnetization M_F = 140 kA/m and exchange constant A_F = $3.32 \cdot 10^{-12}$ J/m.
Magnetic parameters of the disks: M_D = 810 kA/m and A_D = $10.0 \cdot 10^{-12}$ J/m.

Set2 Geometric parameters: $t = 20$ nm, $t_1 = 8$ nm, $t_2 = 16$ nm, $d = 350$ nm and periodicity $a = 700$ nm [Fig. 2.6].
Magnetic parameters of the thin film: saturation magnetization M_F = 140 kA/m and exchange constant A_F = $3.32 \cdot 10^{-12}$ J/m.
Magnetic parameters of the disks: M_D = 735 kA/m and A_D = $10.0 \cdot 10^{-12}$ J/m.

As already mentioned the gyromagnetic ratio in MicroMagus is $\gamma/2\pi$ = 28.5 GHz/T. When modeling a magnetic film composed of YIG in simulation this value is reasonable, because YIG exhibits a gyromagnetic ratio of 28.3 GHz/T [CLZ$^+$14]. But for modeling a magnetic disk composed of Py the value of $\gamma/2\pi$ = 28.5 GHz/T might lead to a lower resonance frequency in simulation than expected in experiment, because Py exhibits a gyromagnetic ratio of 29.3 GHz/T [SPS88]. Therefore we increased the saturation magnetization of the magnetic disks in Set1 in simulation compared to the saturation magnetization determined for Py used in experiment (section 4.2.1). Calculating the resonance frequency of an infinite magnetic film with Ref. [KS86] and using M_D = 810 kA/m and $\gamma/2\pi$ = 28.5 GHz/T we obtain a similar field dependence as for M_D = 770 kA/m and $\gamma/2\pi$ = 29.3 GHz/T (not shown).

The geometric and magnetic parameters chosen for Set2 were optimized for the investigation of MGC modes and are therefore different to the parameters of Set1.

3 Experimental setup and techniques

For the preparation and investigation of samples different techniques were utilized. In this chapter we give an overview of the following techniques: BSWS, μBLS and HIM. EBL or optical lithography used for sample preparation are not presented in this chapter, because this techniques are well-known.

3.1 Broadband spin-wave spectroscopy

In this section we give an introduction to BSWS. We introduce the setup and address basic terms as design and signal generation and detection of CPWs.

3.1.1 Experimental setup

The setup for BSWS consists of the following elements also shown in Fig. 3.1:

1. For experiments we use a vector network analyzer (VNA) of Agilent either the model 2 Port or the model 4 Port. The VNA provides a continuous frequency f from 10 MHz to 26.5 GHz at distinct microwave power usually ranging from -20 dBm to 0 dBm. The ports act independently as a source or drain for electromagnetic waves. Thereby the VNA records the scattering parameters (see section 3.1.2).

2. To guide the electromagnetic wave from the VNA to the sample we use microwave cables and high frequency tips (microprobes). These components are impedance matched to minimize reflections of the electromagnetic wave.

3. (a) An external magnetic field $|\mathbf{H}|$ up to 100 mT can be applied in the sample plane in all directions. The magnetic field is generated by coils connected to bipolar power sources, allowing for

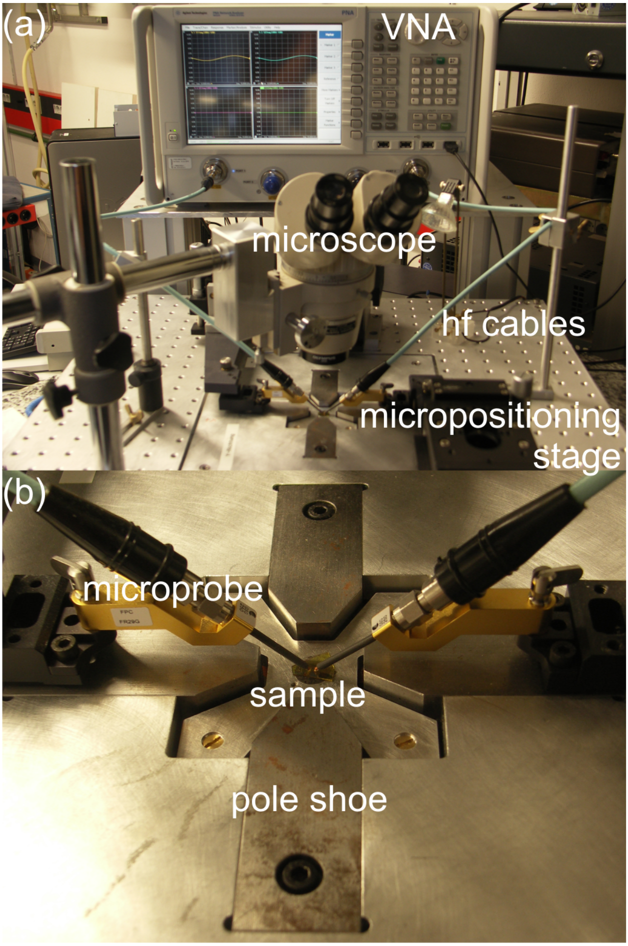

Figure 3.1: Photograph of the BSWS setup. In (a) the VNA 4 Port and the coaxial microwave cables connecting the microprobes with the VNA are depicted. The VNA is used as source for high frequency electromagnetic waves. In (b) the microprobes are shown that are used to connect the sample. The microprobes are positioned with micrometerstages.

continuous sweeps or constant current. The perpendicular arranged pole shoes are used to create a homogeneous magnetic field at the position of the sample.

   (b) An out-of-plane field up to 2.5 T and a temperature ranging from 4 to 400 K can be applied by an cryostat with a superconductive coil.

4. Hall sensors are used to read out the magnetic field. The voltage signal provided by the Hall sensors is amplified by lock-in detectors. We use a 3-axis Gaussmeter to calibrate the Hall sensors before the measurement by connecting a distinct voltage signal to an absolute value of the magnetic field. This is done individually for both axes in the sample plane.

5. A computer program is used to control the external magnetic field and the VNA. The voltage of the Hall sensors is used in feedback circuit to stabilize the external magnetic field **H**. Data acquisition is done automatically.

6. To remove vibrational noise from the experimental setup we use a shock absorber for the critical components as the VNA and the magnetic field coils.

3.1.2 Scattering parameter

To investigate the properties of high frequency devices we use the so called scattering parameters [Mav96]. For electrical circuits we define the high frequency electromagnetic wave scattering by a set of S-parameters

$$\begin{pmatrix} b_1 \\ b_2 \end{pmatrix} = \begin{pmatrix} S_{11} & S_{12} \\ S_{21} & S_{22} \end{pmatrix} \begin{pmatrix} a_1 \\ a_2 \end{pmatrix} \tag{3.1}$$

The incident amplitude is denoted by a_i and the reflected power by b_j with $i, j = 0, 1$. Thus the S-parameters measured by the VNA consist of the ratio between reflected and incident amplitude as indicated by Eq. 3.1. The S-parameters are characterized either by magnitude $Mag(S_{\mathrm{ij}})$ and phase $\phi(S_{\mathrm{ij}})$ or real part $\mathcal{R}(S_{\mathrm{ij}})$ and imaginary part $\mathcal{I}(S_{\mathrm{ij}})$. Because we use a 2 port geometry the reflected wave is given by S_{11} and S_{22}, respectively. The S-parameters S_{12} and S_{21} are used to characterize the

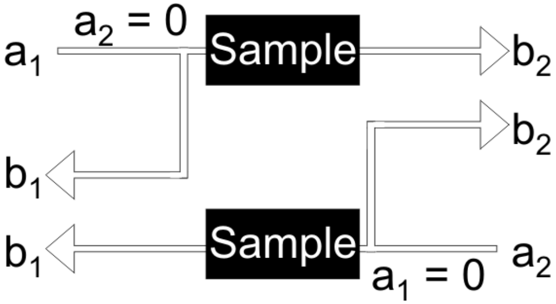

Figure 3.2: Definiton of the S-parameters in Eq. 3.1

transmission of the electromagnetic signal. For S_{21} (S_{12}) the signal is transmitted from port 1 to port 2 (from port 2 to port 1).

3.1.3 Design of the coplanar waveguide

For guiding a high frequency electromagnetic wave on a substrate we utilize a CPW [Sim01]. A CPW is a metallic structure composed of three electrically conducting lines aligned parallel. To obtain the desired excitation spectrum the CPW is placed on top of an insulating substrate. The geometrical parameters are defined by the width w, the gap r and the thickness t_{s} of the CPW. The CPWs consisted of a taper region (1) used to contact the sample by the microwave tips and to guide the electromagnetic wave to the excitation region (2) [Fig. 3.3]. The excitation region is designed to excite specific wave vectors k.

We assume that along the CPW a transversal electromagnetic wave propagates. For an ideal CPW the impedance $Z_{\mathrm{c}} = \sqrt{\frac{L}{C}}$ matches $Z_{\mathrm{c}} = 50\ \Omega$ with $L = \mu_0/4f(r,w)$, $C = 4\tilde{\epsilon}/f(r,w)$ and $f(r,w)$ an involved function. The variable $\tilde{\epsilon}$ denotes the effective permittivity. Following [WO90] we obtain

$$Z_{\mathrm{c}} = 1/4\sqrt{\frac{\mu_0}{\tilde{\epsilon}}f(s,w)}. \tag{3.2}$$

If the impedance deviates from Z_{c} the electromagnetic wave is scattered.

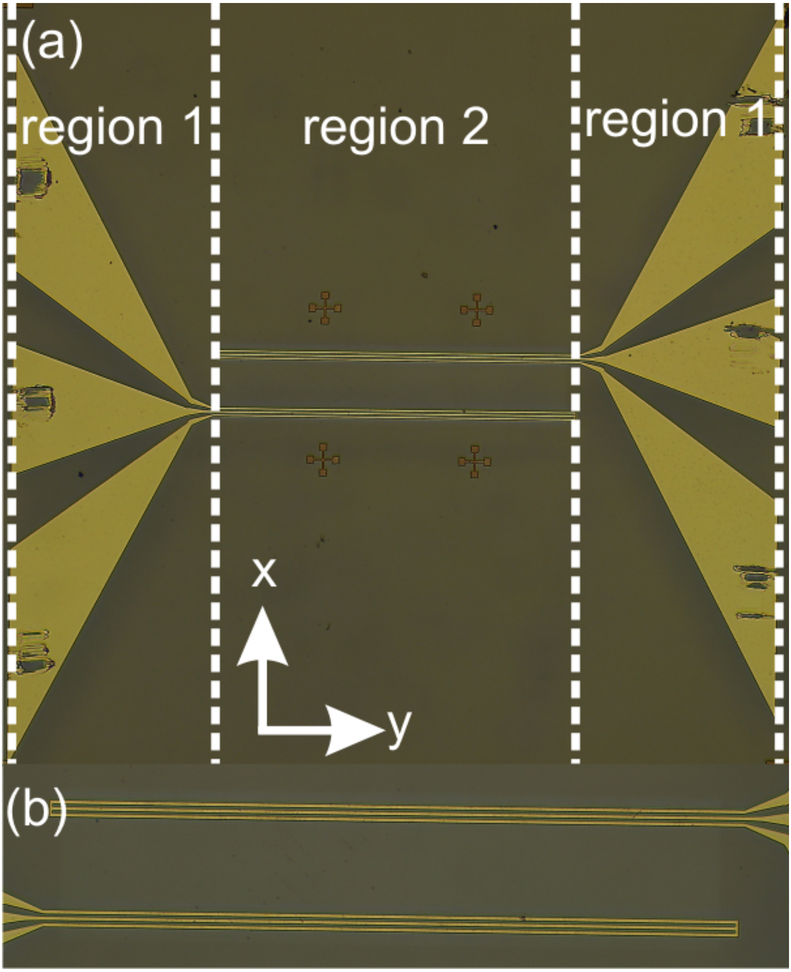

Figure 3.3: (a) Image of the CPW design obtained with a optical microscope. Region 1 and region 2 highlight the taper and excitation region, respectively. (b) The antennas of the CPWs consist of two ground lines (outer conductor) and one signal line (inner conductor).

The relevant scattering parameter is defined with $\Gamma_Z = \frac{Z_1 - Z_\mathrm{c}}{Z_1 + Z_\mathrm{c}}$ with Z_1 describing the impedance deviation. Because we use ferromagnetic materials in the following Eq. 3.2 is converted using $\mu_0 \to \tilde{\mu}$

$$Z_\mathrm{c} = 1/4\sqrt{\frac{\tilde{\mu}}{\tilde{\epsilon}} f(s, w)}. \tag{3.3}$$

Here $\tilde{\mu}$ is the effective permeability. For a resonance of the magnetic film $\tilde{\mu}$ alters and the electromagnetic wave is scattered. More details of high frequency properties of the measurement technique are described in [Bil07].

3.1.4 Signal generation and detection

With the VNA we apply a microwave current $i(f)$ to the signal and ground lines of the CPW [Fig. 3.4 (a)]. The high frequency magnetic field $\mathbf{h}^\mathrm{rf}(x, f)$ generated around the conductors [Fig. 3.4 (b)] is described by Biot-Savart's law. As described in section 2.3.1 a high frequency field induces a spin-precessional motion. By the precessing magnetization we obtain a magnetic flux ϕ_M in the CPW generating a voltage. Following Ref. [Gie05, Neu11] the magnetic flux is described using the magnetization **M** and the dynamic magnetic field $\mathbf{h}^\mathrm{rf}$

$$\phi_M = \mu_0 \int_{V_\mathrm{s}} \frac{\mathbf{h}^\mathrm{rf}}{I} \mathbf{M} dV \tag{3.4}$$

with V_s the sample volume and I the current enclosed in the CPW. The magnetic field $\mathbf{h}^\mathrm{rf}$ is aligned perpendicular to the CPW and we take only the in-plane component $\psi(x)$ into account. We assume a spatial distribution for $\mathbf{h}^\mathrm{rf}$ with $\int dy \psi(x) = \Psi$. Therefore Eq. 3.4 reads

$$\phi_\mathrm{M} = \frac{\mu_0 t_\mathrm{s} l sin \iota}{w\Psi} \int \psi x M_\mathrm{x}(x, t) dV \tag{3.5}$$

with ι defining the angle between **M** and the *x* axis, l the length of the conductor. The induced voltage is described by

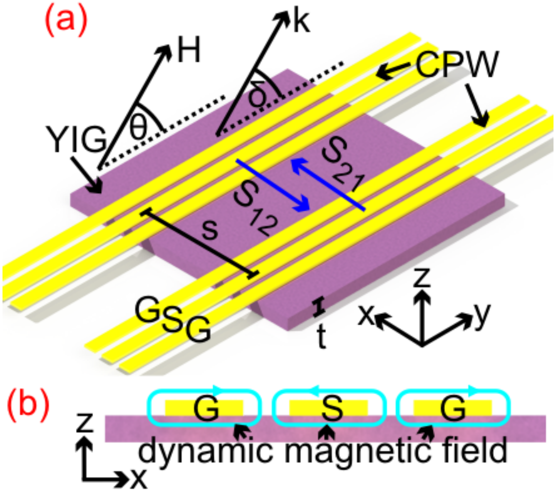

Figure 3.4: (a) Sketch of a bare magnetic film with thickness t investigated with BSWS. The parameter s describes the distance between the signal lines of CPWs. The angle θ (δ) describes the angle enclosed by the external magnetic field (wave vector of the SW) to the CPW. (b) Sideview of the sample. The lines around ground (G) and signal (S) lines indicate the dynamic magnetic field $\mathbf{h}^{\mathrm{rf}}$.

$$
\begin{aligned}
V_{\mathrm{ind}} = -\frac{d\phi_{\mathrm{M}}}{dt} = \\
= -C\int \psi(x)\frac{dM_{\mathrm{x}}(x,t)}{dt}dx = \\
= -C\int \psi(x)\chi_{\mathrm{xx}}\frac{dh(x,t)}{dt}dx
\end{aligned}
\tag{3.6}
$$

with χ_{xx} denoting the susceptibility. In a next step we transform Eq. 3.6 to reciprocal space

$$
V_{\mathrm{ind}} = -C'\int \rho(k)\chi_{\mathrm{xx}}(k)h(k,w)dk \tag{3.7}
$$

with $\rho(k)$ denoting the SW excitation distribution. For harmonic excitations we calculate the time derivative to $\frac{dh(t)}{dt} = -i\omega h(\omega)$ and we assume $\rho(k) = h(k)$. The measured signal a_{ii} that is proportional to V_{ind} containing the susceptibilities of all excited SWs can be expressed with [VB10]

$$a_{\mathrm{ii}}(\omega) \propto \int \chi(\omega, k)\rho(k)^2 dk. \tag{3.8}$$

The measured signal a_{ii} is the relative self-inductance of the CPW. To describe propagating SWs an exponential function with a complex wave vector is used including a phase and attenuation for the SW

$$a_{\mathrm{ji}}(\omega) \propto \int \chi(\omega, k)\rho(k)^2 e^{-ikx} dk \tag{3.9}$$

with a_{ji} the relative mutual inductance of two CPWs. The CPW i is used to excite spin waves and CPW j is used for detection. The voltage generated by the precessing magnetization alters the impedance matrix Z_{ji}. Thus also the S-parameter matrix is altered following the correlation $S_{\mathrm{ji}} \longleftrightarrow Z_{\mathrm{ji}}$ [ASG97].

3.1.5 Excitation characteristics of prepared coplanar waveguides

For the excitation of SWs we used different types of CPWs that we introduce in this section. CPWs consist of a 4.5 nm chromium and a 120 nm gold layer. We use simulation to model the characteristic excitation of the CPW generated by its magnetic field $\mathbf{h}$ [CST].

The smallest signal line width used for a CPW in this thesis was 2.1 ± 0.2 μm. The edge-to-edge distance r of signal and ground line was 1.4 ± 0.2 μm. The CPWs were 40 to 380 μm long. CPWs with a length of 380 μm are depicted in Fig. 3.3. We have prepared two CPWs that were aligned parallel. The separation s between both signal lines was 20 μm to 60 μm [Fig. 3.4 (a)]. We show the calculated excitation amplitudes of the CPW in Fig. 3.5 in dependence of the SW wave vector k excited in the magnetic film.

The Fourier analysis reveals that the maximum excitation amplitude of the CPW is at 0.9 rad/μm labeled with k_{I}. But also various other wave vectors are excited up to 20.0 rad/μm labeled with k_{II} to k_{XI}. The calculation was performed by Ioannis Stasinopoulos and Filip Lisiecki.

In case of large s up to 2 mm, we used CPWs with different geometric parameters: $w = 3$ μm and $r = 2$ μm. The length of the CPW

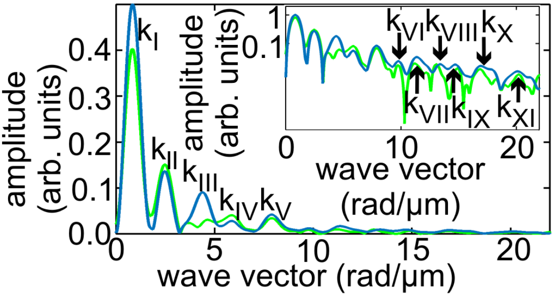

Figure 3.5: Simulated excitation amplitude in dependence of the wave vector k. We assumed a CPW with $w = 2.1$ μm and $r = 1.5$ μm. We present the Fourier analysis for component $h_z(x)$ ($h_x(x)$) of $\mathbf{h}$ corresponding to the blue (green) line. The data of the inset is plotted as half-logarithmic graph. Labels highlight peaks used throughout this thesis.

was 2 mm. With the Fourier analysis a maximum excitation amplitude $k_{\mathrm{I}} = 0.4$ rad/μm was calculated. The calculation was performed by Ioannis Stasinopoulos and Markus Kleinhans.
To investigate the samples also for small wave vectors we used a CPW with a signal line width of 20 μm and a length $l = 9$ mm. The wave vector distribution is shown in Ref. [Sch13] revealing a maximum excitation amplitude k_{I} at 0.1 rad/μm.

3.1.6 Ferromagnetic resonance using vector network analyzer

We used the experimental technique vector network analyzer ferromagnetic resonance (VNA-FMR) for FMR measurements over a broad frequency spectrum [KBBG02, CKD$^+$04, Gie05, Bil07, NDB$^+$10]. The CPW we applied in the experiment is 9 mm long and the signal line width w is 20 μm. The maximum excitation amplitude k_{I} at 0.1 rad/μm (section 3.1.5) is close to $k = 0$. Thus this technique is called VNA-FMR. The measurements are performed in the flip chip geometry. This means the sample is orientated face down onto the CPW. The VNA connected to the CPW measures the S-parameters in dependence of the excitation frequency f and the external magnetic field $\mathbf{H}$. Because we perform a continuous wave experiment the S-parameters are obtained for a distinct external magnetic field **H** and angle θ. Following Eq. 3.7 the scattering of electromagnetic waves for a resonant excitation change.

3.1.7 Frequency-resolved spin-wave spectroscopy

For frequency-resolved spin-wave spectroscopy we apply two CPWs aligned parallel. The CPWs have a signal line width w between 2.1 μm and 3 μm. This arrangement of the CPWs allows us to investigate propagating SW at $k \neq 0$. CPW 1 acts as emitter/detector and CPW 2 acts as detector/emitter, respectively. Again we perform a continuous wave experiment acquiring the S-parameters at a distinct external magnetic field **H** and angle θ. In Ref. [BOF03, VB10, YHS$^+$12] it was demonstrated that a propagation analysis is practical. The parameter a_{ii} is used to investigate the susceptibility χ and the parameter a_{ji} with $i \neq j$ exhibits the propagation signal. The phase ϕ resolved by the detector is denoted with

$$\phi = k \cdot s \tag{3.10}$$

with k the wave vector of the SW and s the separation between the CPWs. Changing the frequency f applying a VNA changes the wave vector k. This leads to a change of the phase ϕ . We can determine the group velocity by measuring the phase shift $\delta\phi$ by changing the frequency δf. The group velocity is then described by

$$v_{\mathrm{g}} = \frac{\partial\omega}{\partial k} = 2\pi s\frac{\delta f}{\delta\phi}. \tag{3.11}$$

We use $\mathcal{I}(S_{12})$ with $i \neq j$ for extracting the group velocity [BOF03, NDB$^+$10, YHS$^+$12]. A example for a spectra obtained for propagating SWs is given in Fig. 3.6 showing $\mathcal{I}(S_{12})$ exhibiting local extrema. Neighboring extrema show a phase shift of $\delta\phi = 2\pi$. If we introduce this correlation to Eq. 3.11 we obtain

$$v_{\mathrm{g}} = 2\pi s\frac{\delta f}{2\pi} = \delta f \cdot s \tag{3.12}$$

with δf the frequency spacing between neighboring extrema.

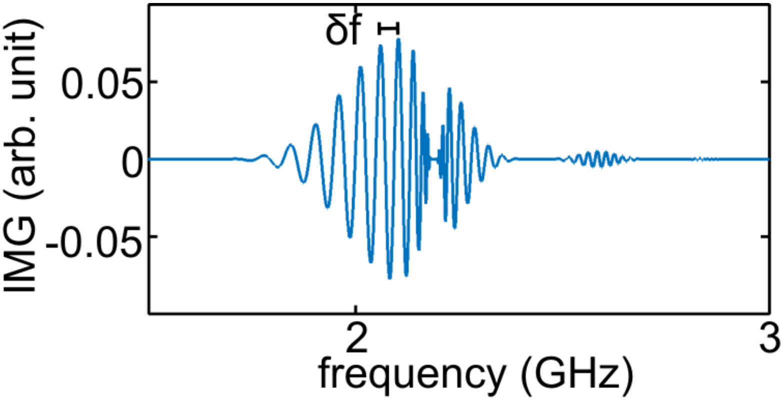

Figure 3.6: Propagating SW spectra. The parameter δf denotes the frequency spacing between neighboring extrema.

3.1.8 Evaluation and processing of measured spectra

The measured spectra were evaluated with two different methods:

Method 1 We subtract a reference spectrum $S_{\mathrm{ij}}(Ref)$ from the measured spectrum $S_{\mathrm{ij}}(Meas)$. Thus we obtain $\Delta S_{\mathrm{ij}} = S_{\mathrm{ij}}(Meas) - S_{\mathrm{ij}}(Ref)$ to remove field-independent background signals.

Method 2 We subtract spectra taken at successive field H or angle θ. For field sweep measurements we apply $\Delta S_{\mathrm{ij}}(H,\theta) = S_{\mathrm{ij}}(H,\theta) - S_{\mathrm{ij}}(H+1,\theta)$. For angle scan measurements we apply $\Delta S_{\mathrm{ij}}(H,\theta) = S_{\mathrm{ij}}(H,\theta) - S_{\mathrm{ij}}(H,\theta+1)$. With this method we increase the signal to noise ratio.

The group velocity is calculated by extracting the frequency spacing between neighboring extrema (section 3.1.7). To avoid falsification of the local extrema we applied the first method to spectra that are used to extract the group velocity of propagating SWs. The second method was applied to extract the wave vector of the spectra because of the increased signal to noise ratio. If not stated differently we always applied the second method in the following chapters.

For the extraction of the nonreciprocity parameter β we apply the following equation:

$$\beta = \frac{a(\Delta S_{12}(H))}{a(\Delta S_{12}(-H)) + a(\Delta S_{12}(H))} \tag{3.13}$$

with a denoting the maximum amplitude of ΔS_{12} and ΔS_{21} evaluated with method 1.

3.2 Micro-focused Brillouin light scattering

In this chapter we introduce the experimental setup of μBLS. While the BSWS setup described above is sensitive to the whole area covered by the CPW, μBLS allows for the investigation of SWs on the scale of a few micrometer. The key components of this setup are a continuous wave laser, a Glan-Laser polarizer to increase the signal to noise ratio and a multipass tandem interferometer for high contrast. Using a scanning laser microscope we can investigate SWs in two dimensions. To counteract the drift of the microscope a CCD camera is applied using optical feedback for beam position correction. The complete setup is shown in Fig. 3.7.

3.2.1 Inelastic light scattering

For the technique of BLS photons are used for the investigation. The photons interact with the SWs. In the classical picture a phase grating propagating with the velocity of the SW is induced in the material by spin-orbit coupling. The scattering process of the photons is then described as Bragg-reflection from the phase grating. The frequency of the photon is Doppler-shifted by the SW frequency. This treatment accounts for many materials [Hil00]. The process can also be treated as inelastic scattering of a photon with a magnon [Hil00]. The magnon is the quasiparticle of the SW. Energy and momentum of the scattered photon are described with

$$\begin{aligned} \hbar\omega_\mathrm{s} &= \hbar\omega_\mathrm{i} \pm \hbar\omega \\ \hbar\mathbf{k}_\mathrm{s} &= \hbar\mathbf{k}_\mathrm{i} \pm \hbar\mathbf{k} \end{aligned} \tag{3.14}$$

$\mathbf{k}_\mathrm{i}$, ω_i ($\mathbf{k}_\mathrm{s}$, ω_s) are describing the wave vector and frequency of the incident (scattered) photon. Wave vector and frequency of the magnon are described with **k** and ω.

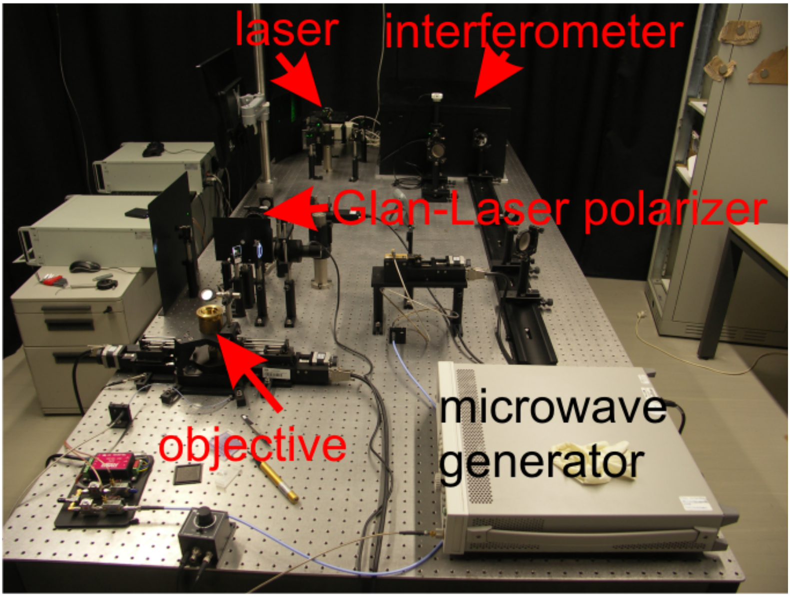

Figure 3.7: Experimental setup μBLS used throughout this thesis. The most important elements are highlighted.

3.2.2 Micro-focused Brillouin light scattering setup

As source for coherent light a solid state laser is utilized. The laser emits polarized light with a wavelength of 532 nm. By expanding and collimating the laser beam the divergence of the light is reduced. The light is guided through a Glan-Laser Polarizer to further increase the polarization. The beam is then focused on the sample surface with a objective lens exhibiting a magnification of 100 and numerical aperture of 0.75. We obtain a spot size of 250 to 300 nm for the laser beam. The sample is mounted on a XYZ-piezo stage to allow for movement in 3 dimensions. By adjusting the distance of sample and objective lens using the stage the laser beam is focused on the sample surface. The remaining degrees of freedom are used to scan the laser beam over the sample surface.

The light is reflected from the sample surface. A part of the reflected light is scattered on magnons and the polarization is rotated by 90 deg.

By guiding the reflected light back through the Glan-Laser Polarizer only the light scattered on magnons is guided to the multipass tandem interferometer. The interferometer selects a specific wavelength/frequency of the scattered light corresponding to a specific frequency of the magnon [Eq. 3.14]. The photons are detected by a photon counter. The signal strength is proportional to the photons detected by the photon counter. By varying the selected wavelength/frequency of the light we can select the magnon frequency that is investigated. More details of the setup are given in Refs. [DDH$^+$04, DD08].
The SWs are excited using a CPW. The dimensions of the setup do not allow for contacting the sample with a microwave tip as in section 3.1.1. The CPW is connected using thin cooper wires and a 2D pad structure attached with conducting glue to a GHz connector. But this part is not optimized for guiding a electromagnetic wave and thus the signal reaching the CPW is decreased. Therefore a increased microwave power output is necessary.

3.2.3 Multipass tandem interferometer

Following Eq. 3.14 the frequency difference of incident and inelastic scattered light has to be determined. But the frequency difference is usually very small, because the phase velocity of magnons is very small in comparison with the phase velocity of light:

$$\omega = v \cdot k \ll c_{\mathrm{i}} \cdot k_{\mathrm{i}} = \omega_{\mathrm{i}} \Longrightarrow \omega_{\mathrm{i}} \pm \omega \approx \omega_{\mathrm{i}}. \tag{3.15}$$

To determine the frequency difference we use a multipass tandem interferometer. Core of the interferometer is a Fabry-Perot interferometer. A single Fabry-Perot interferometer consists of two plane parallel mirrors with tunable distance d and high reflectivity R. The transmission is given by [Jac60, DVHVDA81]

$$I = (\frac{T}{1-R})^2 \frac{1}{1 + (4R/(1-R)^2) sin^2(2\pi\sigma d\lambda)} \tag{3.16}$$

with T and σ indicating the transmission of the mirror and the wave number $\sigma = 1/\lambda$. The maximum transmission is [Jac60]:

$$I_0 = \left(\frac{T}{1-R}\right)^2 = \left(1 - \frac{A}{1-R}\right)^2 \tag{3.17}$$

with A indicating the absorption of the mirrors with $A = 1 - T - R$. If the condition of positive interference is satisfied

$$d = \frac{m\lambda}{2} = \frac{m}{2\sigma} \Longrightarrow \sigma = \frac{m}{2d} \tag{3.18}$$

with m an integer number we obtain maximum transmission. Assuming $m_1, m_2 \in \mathbb{N}$ the distance of two peaks with $m_2 = m_1 \pm 1$ is calculated to be $\Delta\sigma = \frac{1}{2d}$. The peak width $\delta\sigma$ is described with [Jac60]:

$$F = \pi\frac{\sqrt{R}}{1-R} = \frac{\Delta\sigma}{\delta\sigma}. \tag{3.19}$$

But as indicated by Eq. 3.18 the condition of positive interference is satisfied for not only one wavelength. In consequence only wave numbers smaller than the peak distance $\Delta\sigma$ can be analyzed. The parameter $\Delta\sigma$ is therefore also known as the free spectral range of the interferometer. To increase $\Delta\sigma$ the mirror distance d could be reduced, but this would lead to an reduction of the spectral resolution [Eq. 3.19]. Another way to increase the free spectral range is using two Fabry-Perot interferometer in series. The transmission is then described with [DVHVDA81]:

$$\begin{aligned} I = I_{01}&\frac{1}{1+(4R/(1-R)^2)sin^2(2\pi\sigma d_1\lambda)}\times \\ I_{02}&\frac{1}{1+(4R/(1-R)^2)sin^2(2\pi d_2\sigma\lambda)}. \end{aligned} \tag{3.20}$$

The indices 1,2 specify the Fabry-Perot interferometer 1 and 2, respectively. A wave has to fulfill the condition in Eq. 3.18 for both Fabry-Perot interferometer for transmission:

$$d_1 = 1/2m\lambda; d_2 = 1/2n\lambda \tag{3.21}$$

with $m, n \in \mathbb{N}$. Assuming $d_1 \neq d_2$ the distances $\Delta\sigma_1$ and $\Delta\sigma_2$ to the neighboring transmission maxima are different for Fabry-Perot interferometer 1 and Fabry-Perot interferometer 2. Consequently by multiplying the transmission signal for Fabry-Perot interferometer 1 and Fabry-Perot interferometer 2 the neighboring transmission maxima do not overlap and are suppressed. To enhance this effect the light is guided several times

through each Fabry-Perot interferometer.
Let us assume now that the parameters d_1, d_2, m and n are set so that Eq. 3.21 is fulfilled for a wavelength λ_0. By altering the wavelength the mirror distance has to be changed following [LAS81]

$$\Delta\lambda = 2\frac{\Delta d_1}{m} = 2\frac{\Delta d_2}{n} \tag{3.22}$$

that the wavelength again passes both Fabry-Perot interferometer. From Eq. 3.21 and Eq. 3.22 we obtain:

$$\frac{\Delta d_2}{\Delta d_1} = \frac{d_2}{d_1}. \tag{3.23}$$

For the tandem interferometer one mirror of each Fabry-Perot interferometer is placed on a fixed position on the setup table while the other mirror is placed on a moving stage [Fig. 3.8]. The orientation of one Fabry-Perot interferometer is rotated by an angle α with respect to the second Fabry-Perot interferometer. Because the mirrors are on the same stage, the movement of both Fabry-Perot interferometer is synchronous and the following relation accounts:

$$d_2 = d_1 cos\alpha; \Delta d_2 = \Delta d_1 cos\alpha \tag{3.24}$$

Equation 3.24 meets the condition in Eq. 3.23.
Because the light beam is sent several times through each Fabry-Perot interferometer the device is called multipass tandem interferometer.

3.3 Helium ion microscopy

For nanostructuring of samples usually EBL is applied. In this thesis we also use HIM for this purpose. By the utilization of HIM the periodicity of the lattice is reduced down to 100 nm. In this section we give an introduction to this technique. A detailed instruction can be found in Refs. [HNS12, HVvGP14].
The working principle can be divided in three parts:

- **Helium ionization and acceleration**

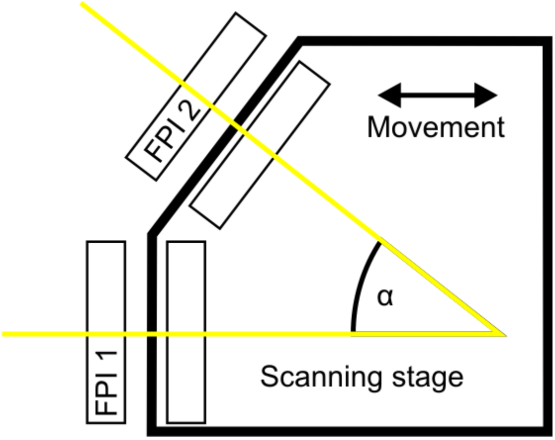

Figure 3.8: Schematic sketch of a tandem interferometer and the arrangement of the Fabry-Perot interferometer (FPI). One mirror of each Fabry-Perot interferometer is placed on the moving stage. The orientation of one Fabry-Perot interferometer is rotated by an angle α with respect to the second Fabry-Perot interferometer.

For the generation of Helium ions a parabolic shaped apex is used. The tip of the apex is formed to a three sided pyramid by field evaporation. The three sided pyramid can form a so called trimer at the tip of the apex. By using this shape the helium ions are mainly ionized at the top most atoms of the pyramid.

- **Formation and Control of the beam**

The beam is formed using electrostatic lenses similar to the lenses for EBL. But one has to take into account that the helium ions are positively charged. A important parameter for ion optical performance is the image side beam convergence angle α_i [HVvGP14]. A small side beam convergence angle lead to a large depth of field d_f

$$d_f = \frac{\delta}{\alpha_i} \tag{3.25}$$

The parameter δ describes the minimum feature that can be imaged. For HIM a image side beam convergence angel of 1 mrad [HVvGP14] or below is reached, whereas for low-voltage SEM values of 8 mrad are typical [HNW08].

- **Sample interaction and imaging**

When the helium ions hit the sample secondary electrons are generated. By detecting SEs the sample is imaged. Therefore SEs have to be excited and subsequently transported through the material.
Mainly two types of SEs contribute. The rate of SEs δ_{SE} generated of the first type is proportional to the stopping power of the incident particle dE/ds [Bet41]

$$\delta_{\mathrm{SE}} = -\frac{1}{\epsilon}\frac{dE}{ds} \tag{3.26}$$

with ϵ a scaling constant. Here it is assumed that in the relevant near surface region atomic collisions can be neglected and the parameter dE/ds depends only on the electronic stopping power.
The second type of SEs are excited by recoil atoms, assuming that they are fast enough so that they hit the Fermi velocity of the target material. Then the cross section for this type of collision is highest [HVvGP14].
After the generation of SEs the same have to escape from the solid by diffusion. Following Ref. [RGJ09] the effective diffusion length of SEs in metals is of the order of 1 nm
The high resolution of the HIM can therefore be explained that SEs originate from a small cylinder interacting with the helium ion beam. The cylinder has a size of about 1 nm in diameter (given by the beam diameter) and is 3 nm deep determined by the characteristic electron diffusion length [HVvGP14]. This small interaction volume leads to high resolution.

3.3.1 Direct write lithography

In the following work we use the HIM for nanostructuring. With the HIM we introduce defects arranged in a lattice in two dimensions with distinct lattice constants. This is obtained by illuminating distinct points with the helium ion beam. Due to the illumination the crystal structure of the penetrated sample material is distorted and helium ions are implemented. Thereby we induce columnar crystal lattice distortions (CLD) arranged in a periodic lattice.

4 Preparation

In this chapter we describe the preparation steps that were necessary to fabricate the samples investigated in the chapters 6 to 9. For the preparation we have used two different types of YIG films. Christoph Hauser from the group of Prof. Dr. Georg Schmidt had provided a YIG film grown with PLD and a thickness of 20 nm. The YIG film was nominal identical to the film in Ref. [HRH$^+$16]. Another YIG film was grown commercially with LPE[1] and had a thickness of 200 nm. We utilized the following techniques: optical lithography[2], EBL[3], argon ion milling, physical vapor deposition and HIM[4]. Using the intriguing new technique of HIM we expected a deeper insight into the physics of SWs.

4.1 Preparation of bare yttrium iron garnet films

For the characterization of both YIG films grown with PLD and LPE we fabricated integrated CPWs on top of the surface [CKD$^+$04, NDB$^+$10]. Samples fabricated with PLD had a lateral size of 5 x 10 mm^2. The lateral size of sample pieces that were taken from the YIG wafer grown with LPE was 6 x 6 mm^2. To obtain smooth edges of signal and ground line of the CPW we used EBL for the preparation. We applied the following steps (left column Fig. 4.1):

1. Deposition of 10 nm aluminum (Al) with physical vapor deposition. Without the Al layer the YIG film would be charged up by the electrons and the electron beam would be distorted.

2. Spin coating with AR-P 639.10[5] and subsequent with AR-P 679.02[6]. For both resists we used 4500 rpm for 60 s. The double layer resist

---

[1] Matesy GmbH, Jena, Germany

[2] Süss MicroTec AG, Garching b. München, Germany

[3] Raith Corp., Dortmund, Germany

[4] Carl Zeiss AG, Oberkochen, Germany

[5] Allresist GmbH, Strausberg, Germany

[6] Allresist GmbH, Strausberg, Germany

was used to avoid rims on the fabricated structures.

3. Exposure to electron beam using a dose of 150 μC/μm^2.
4. Developing with AR 600-56[1] for a duration of 60 s. Subsequently the Al was removed with MF-26A[2] using a duration of 20 s.
5. Physical vapor deposition with 4.5 nm chromium and subsequently with 120 nm gold.
6. Lift-off-process with 1165[3] for a duration of 1 h at a temperature of 55°C.

Applying these steps we fabricated CPWs with a width of 2.1 ± 0.2 μm for signal and ground line. The edge-to-edge distance r of signal and ground line was 1.4 ± 0.2 μm. The CPWs were 380 μm long and are depicted in Fig. 3.3. We have prepared two CPWs that were aligned parallel. The separation between both signal lines was 30 μm for the YIG film grown with PLD to compare the results to Ref. [YdKC$^+$14]. For the YIG film grown with LPE we have chosen 60 μm to go beyond Ref. [YdKC$^+$14].

With the samples we addressed propagating SWs in bare YIG films fabricated with PLD and LPE.

4.2 Nanostructuring of yttrium iron garnet films with electron beam lithography

For the preparation of magnetic nanodisks on top of the YIG film grown with PLD and LPE we applied EBL. To minimize the stray field of the magnetic disks we partially embedded the magnetic disks into the YIG film. We applied the following steps (right column Fig. 4.1):

1. Deposition of 10 nm Al with physical vapor deposition. Without the Al layer the YIG film would be charged up by the electrons and the electron beam would be distorted.

---

[1] Allresist GmbH, Strausberg, Germany

[2] Rohm and Haas Company, Philadelphia, PA, USA

[3] Rohm and Haas Company, Philadelphia, PA, USA

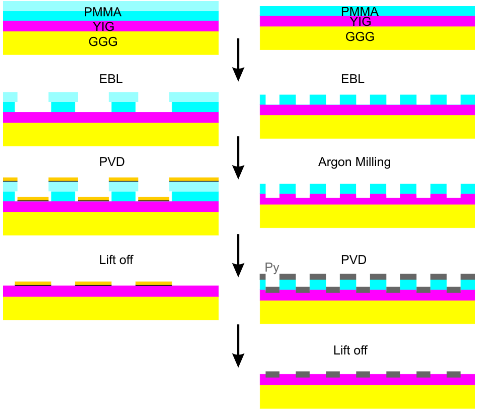

Figure 4.1: Sequence of preparation steps necessary for structuring with EBL. Left column depicts the preparation of integrated CPWs. Right column depicts the preparation of partially embedded magnetic nanodisks.

2. Spin coating with AR-P 672.08[1]. We used 4500 rpm for 60 s. We use a one layer resist, because otherwise the magnetic nanodisks exceeded the diameter of the nanothroughs in the following steps.

3. Exposure to electron beam using a dose of 200 μC/μm^2.

4. Developing with AR 600-56[2] a duration of 90 s. Subsequently Al was removed with MF-26A[3] using a duration of 10 to 45 min. The duration depended on the morphology of the Al due to the small size of the features and varied for every Al layer.

5. Physical etching with argon ion milling to fabricate nanothroughs. The etching depth is limited to 6 nm, because otherwise the resist is to fragile for the lift-off-process after the physical vapor deposition.

6. Physical vapor deposition with Py. To change from argon ion milling to physical vapor deposition the sample was exposed to air.

---

[1] Allresist GmbH, Strausberg, Germany

[2] Allresist GmbH, Strausberg, Germany

[3] Rohm and Haas Company, Philadelphia, PA, USA

7. Lift-off-process with 1165[1] for a duration of 1 h at a temperature of $55°$C.

The resulting structures are depicted in Fig. 4.2 and Fig. 4.4. The figures were obtained using atomic force microscopy (AFM). For the samples we used a periodicity a of 700 nm. The value of 700 nm corresponded to a reciprocal lattice vector of $G_{10} = 9$ radμm and $G_{20} = 18$ radμm. By using this wave vectors in MSSW configuration we avoided the wave vector regime with minimum group velocity for the 200 nm thick YIG film [Fig. 2.1 (b)]. The magnetic nanodisks were arranged in a square lattice to compare the results to Ref. [YDH$^+$13, YdKC$^+$16].
For the 20 nm thick YIG grown with PLD we fabricated a additional sample consisting only of nanothroughs without magnetic disks. Therefore we increased the depth for the fabricated nanothroughs to 7 nm. The etching time for the argon ion milling was increased, because no physical vapor deposition was necessary and therefore no lift-off-process, too.

4.2.1 200 nm thick YIG grown with liquid phase epitaxy

We fabricated 4 different sample geometries (MGC01, MGC02, MGC03, MGC04) for the 200 nm thick YIG film [Fig. 4.3]. The geometric parameters for the samples are summarized in Tab. 4.1. In Fig. 4.2 we present AFM images of the sample surface after physical etching with argon ion milling and after physcial vapor deposition [Fig. 4.2 (a) and (b)]. The definition of the geometric parameters is given in Fig. 4.2 (c).

We fabricated the 4 sample geometries depicted in Fig. 4.3 to address the following topics:

1. MGC01: Sample consisted of two Py nanodisk arrays. A Py nanodisk array was located under each CPW. [Fig. 4.3 (a)]. Between the CPWs no Py nanodisks and also no nanothroughs were prepared. Investigation of propagating SWs with large wave vector induced by Py nanodisks arranged in a square lattice.

2. MGC02: Sample consisted of one large Py nanodisk array. Both CPWs were located on the Py nanodisk array [Fig. 4.3 (b)] to compare results with MGC01.

---

[1] Rohm and Haas Company, Philadelphia, PA, USA

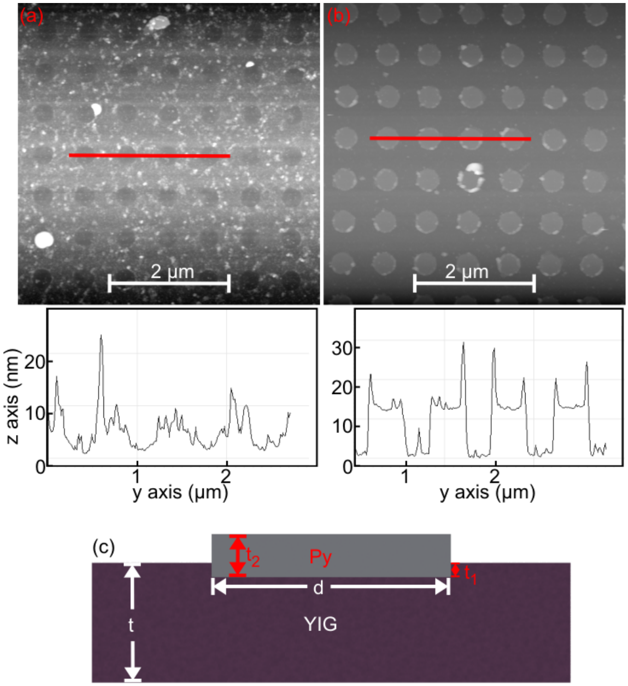

Figure 4.2: (a) Sample topography measured after ion beam milling using AFM. Etched nanothroughs arranged in a square lattice with a depth of 4-6 nm and a periodicity of 700 nm were resolved. (b) Sample after physical vapor deposition of Py using AFM. The embedded Py nanodisks were arranged in a square lattice with a height of 15-16 nm and a periodicity of 700 nm. The diameters of the disks were measured to range from 360 to 380 nm. The line plots on the bottom of (a) and (b) are along the red lines. (c) Basic sketch of the sample geometry (sideview) defining geometric parameters.

$Label$	t_1 (nm)	t_2 (nm)	d (nm)	$size$ (μm^2)
MGC01	4 ± 2	15 ± 4	380 ± 20	365 x 15$*$
MGC02	6 ± 2	16 ± 4	360 ± 20	365 x 85
MGC03	6 ± 2	16 ± 4	360 ± 20	300 x 65
MGC04	6 ± 2	16 ± 4	360 ± 20	365 x 15

Table 4.1: Geometric parameters of samples (MGC01, MGC02, MGC03, MGC04). Sample MGC01 consisted of two independent Py nanodisk arrays ($*$ area of one nanodisk array). Geometric parameters are defined in Fig. 4.2 (c). A sketch of each sample is depicted in Fig. 4.3.

3. MGC03: Sample consisted of one extended Py nanodisk lattice. One CPW was located on the Py nanodisk array the other one on the bare YIG film. [Fig. 4.3 (c)]. Investigation of the reciprocal effect of SWs induced by the MGC effect.

4. MGC04: Sample consisted of one Py nanodisk lattice. The Py nanodisk lattice had the same size as one Py nanodisk lattice of MGC01. One CPW was located on the Py nanodisk array the other one on the bare YIG film. [Fig. 4.3 (d)]. Investigation of the reciprocal effect of SWs induced by the MGC effect and comparison to MGC03.

During physical vapor deposition for the magnetic nanodisks we fabricated simultaneously a Py film. For the Py film we extracted a uniaxial anisotropy between 2 to 3 mT. The uniaxial anisotropy was also observed for the Py nanodisks. If we compare the reference Py film of MGC03 to the reference films of the other samples, the resonance frequency of MGC03 was reduced by 0.5 GHz at 100 mT, although for the samples nominally identical pieces of Py were used for physical vapor deposition. The difference is attributed to the saturation magnetization. For the reference films of samples MGC01, MGC02, MGC04 we extracted a saturation magnetization from 750 kA/m to 770 kA/m. But for the reference film of MGC03 we extract (680±10) kA/m.

For the excitation of SWs we used two integrated CPWs aligned parallel. The separation of the ground lines was 60 μm. The fabrication of the integrated CPWs is described in section 4.1.

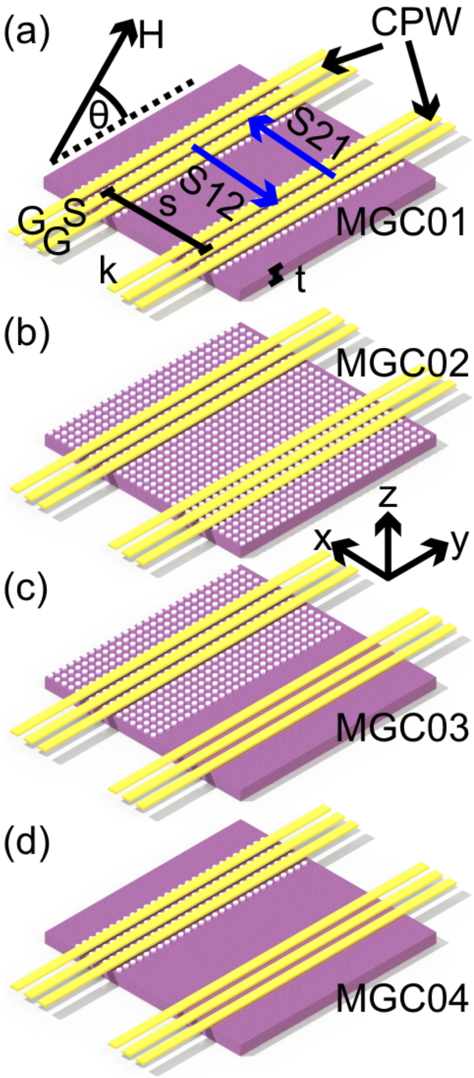

Figure 4.3: (a) - (d) Sample configurations that were investigated. The YIG film for all samples was taken from the same wafer and the Py nanodisks and CPWs were fabricated with nominally identical parameters. The areas covered by Py nanodisks varied from sample to sample.

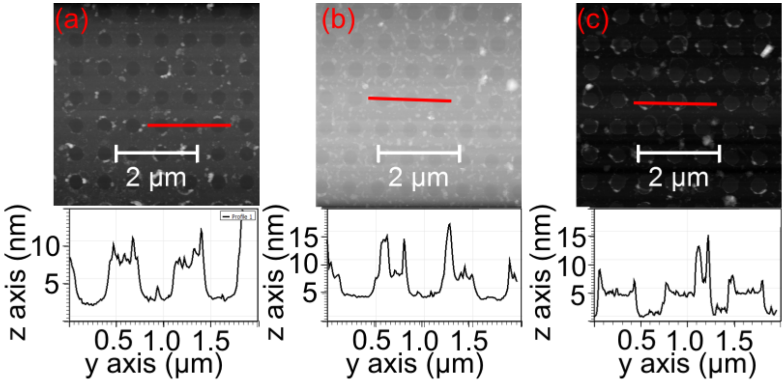

Figure 4.4: (a) Topography of sample TMGC01 after ion beam milling measured with AFM. The etched nanothroughs were arranged in a square lattice with a depth of 7 nm and a periodicity of 700 nm. (b) Sample topography of TMGC02 before physical vapor deposition of Py (AFM data). (c) Sample TMGC02 after physical vapor deposition obtained with AFM. The Py nanodisks were arranged in a square lattice (periodicity of 700 nm) and embedded with a remaining height of 4 nm. The line plots at the bottom are along the red lines in (a) - (c). Geometric parameters of both samples are summarized in Tab. 4.2.

4.2.2 20 nm thick YIG grown with pulsed laser deposition

The sample TMGC01 in Fig. 4.4 (a) consisted of nanothroughs with a depth of $t_1 = 7$ nm. Their diameter d was measured to be 350 nm and the periodicity a amounted 700 nm. The sample TMGC02 in Fig. 4.4 (b) and (c) represents a bi-component MGC. The nanodisks were partially [etching depth $t_1 = 5$ nm] embedded and consist of Py. The height t_2 of the nanodisks was measured to be 9 nm. The diameter d was measured to 400 nm and the periodicity a amounted to 700 nm. The definition of the geometric parameters is given in Fig. 4.2 (c). Geometric parameters are summarized in Tab. 4.2.

For the excitation of SWs we used two integrated CPWs aligned parallel. The separation of the ground lines was 60 μm. The fabrication of the integrated CPWs is described in section 4.1.

Label	t_1 (nm)	t_2 (nm)	d (nm)
TMGC01	7 ± 2	–	350 ± 20
TMGC02	5 ± 2	9 ± 4	400 ± 20

Table 4.2: Geometric parameters of samples TMGC01, TMGC02. Sample TMGC01 consisted of an array of etched nanothroughs. For sample TMGC02 we used Py nanodisks partially embedded in the YIG film. The definition of the geometric parameters is given in Fig. 4.2 (c). The periodicity a for both samples amounted 700 nm.

4.3 Nanostructuring of yttrium iron garnet films with helium ion microscopy

This technique was applied to the YIG film grown with LPE. With the HIM (section 3.3) we nanostructure the YIG film with periodic arranged columnar CLDs. We applied the following steps to the sample:

1. Deposition of 10 nm Al with physical vapor deposition. Without the Al layer the YIG film would be charged up by the helium ions and the helium ion beam would be distorted.
2. Correction of focus, aperture and stigmatism of the microscope using a gold marker.
3. Exposing the helium ion beam to positions arranged periodically applying a dose of 0.1 nC/μm^2 using a acceleration voltage of 30 keV.
4. Removing the Al using MF-26A[1] for a duration of 60 s.

For the periodicities of the CLDs we have chosen 100 nm and 400 nm [Fig. 4.5 (a) and (b)]. The geometric parameters are given in Tab. 4.3. The periodicity of 100 nm was used to investigate SWs for small lattice constants and the periodicity of 400 nm was necessary to obtain a nanostructured area with a size between 29 x 15 μm^2 to 30 x 15 μm^2. If the nanostructured area would get too small we could not detect SW signal with a integrated CPW of the nanostructured area. For the excitation of

---

[1] Rohm and Haas Company, Philadelphia, PA, USA

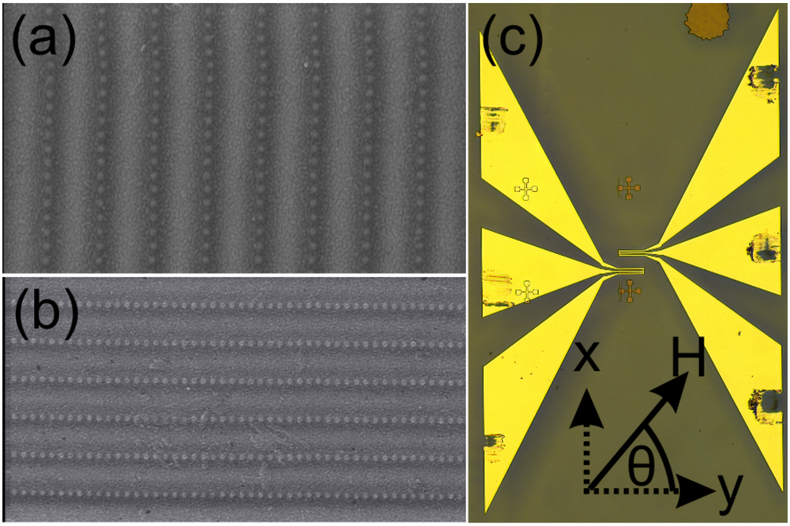

Figure 4.5: (a) HIM picture of sample H01 with periodicities of $a_\mathrm{x} = 100$ nm and $a_\mathrm{y} = 400$ nm. (b) HIM picture of sample H02 with periodicities of $a_\mathrm{x} = 400$ nm and $a_\mathrm{y} = 100$ nm. (c) CPWs used to measure SWs. The length of the CPWs was 40 μm and the distance s between the CPWs ranged from 20 to 28 μm from sample to sample.

SWs we used two integrated CPWs aligned parallel [Fig. 4.5 (c)]. We fabricated CPWs with a width of 2.1 $\pm$ 0.2 μm for signal and ground line. The edge-to-edge distance r of signal and ground line was 1.4 $\pm$ 0.2 μm. The length of the CPW was 40 μm to obtain signal from the nanostructured area. The length of the CPW exceeded the length of the nanostructured area to obtain also signal form the bare YIG film as reference signal. Beside the length of the CPWs the fabrication and the geometric parameters were nominally identical to the integrated CPWs described in section 4.1.

We fabricated 4 different samples H00, H01, H02, H03. A sample fabricated with the HIM consisted of one CPW and one array of periodic arranged CLDs [Fig. 4.6]. With the samples we addressed the following topics:

1. H00: Bare YIG film to characterize the 40 μm long CPW.

label	a_x (nm)	a_y (nm)	size (μm^2)
H00	–	–	bare film
H01	100	400	30 x 15
H02	400	100	29 x 15
H02	400	100	29 x 15

Table 4.3: Geometric parameters of samples H00, H01, H02, H03.

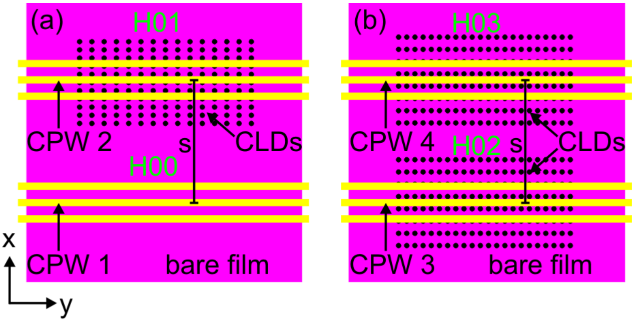

Figure 4.6: Sample geometries used for SW propagation experiment. The sample geometry in (a) was used to measure propagating SWs between sample H00 and H01. The sample geometry in (b) was used to measure propagating SWs between sample H02 and H03.

2. H01: Investigation of SWs in periodic arranged CLDs ($a_\mathrm{x} = 100$ nm and $a_\mathrm{y} = 400$ nm) fabricated with HIM [Fig. 4.5 (a)].

3. H02, H03: Investigation of periodic arranged CLDs ($a_\mathrm{x} = 400$ nm and $a_\mathrm{y} = 100$ nm) fabricated with HIM [Fig. 4.5 (b)]. The lattice symmetry was rotated by 90 deg compared to H01. The results are compared to H01.

4. The samples are also used for propagation measurement. Propagating SWs were measured between sample H00 and H01 [Fig. 4.6 (a)] and between H02 and H03 [Fig. 4.6 (b)], respectively.

The signal lines for the sample geometry in Fig. 4.6 (a) had a distance s of 20 μm and the signal lines for the sample geometry in Fig. 4.6 (a) had a distance s of 28 μm.

4.4 Preparation of flip-chip coplanar waveguides

To investigate samples on the millimeter scale so called flip-chip measurements were performed. The lateral sample size varied between 5 x 5 mm^2 and 2 x 8 mm^2. For this experiment the whole sample was put face down on the CPW and long CPWs were needed. Optical lithography allowed to illuminate large areas and the fabrication of CPWs that were between 2 to 9 mm long. We applied the following steps to prepare flip-chip CPWs:

1. Spin coating the substrate (GaAs[1]) with LOR-3A[2] using 4500 rpm and subsequently with S1813 G2[3] using 6000 rpm for 60 s.
2. Illumination using a lithography mask with a power density of 15 mW/cm^2 and a duration of 4 s.
3. Developing with MF-26A[4] and a duration of 25s.
4. Physical vapor deposition with 4.5 nm chromium and subsequently with 120 nm gold.
5. Lift-off-process using 1165[5] for a duration of 1 h at a temperature of 55°C.

We used the CPWs in section 3.1.5 with a signal line width w of 3 μm and 20 μm in flip-chip configuration.

---

[1] Freiberger Compound Materials GmbH, Freiberg, Germany
[2] MicroChem Corp., Newton, MA, USA
[3] Rohm and Haas Company, Philadelphia, PA, USA
[4] Rohm and Haas Company, Philadelphia, PA, USA
[5] Rohm and Haas Company, Philadelphia, PA, USA

5 Magnonic grating-coupler effect investigated with micro-magnetic simulation

In this chapter we investigate the origin of the MGC effect on the microscale using micro-magnetic simulations. The geometry consisted of a magnetic film and magnetic disks. We present micro-magnetic simulations for different sample geometries and different thickness t for the magnetic film. For micro-magnetic simulation using $t = 200$ nm we modeled the samples investigated experimentally in chapter 8. But for a detailed investigation of the MGC modes we optimized the geometric and magnetic parameters using $t = 20$ nm. This allowed us to study different types of MGC modes on the microscale. The simulation were performed using the MicroMagus package [BG].

5.1 Micro-magnetic simulation of magnonic grating-coupler mode

For the simulation presented in this section we used geometric and magnetic parameters similar to the samples investigated in chapter 8. For the simulation we set the geometric and magnetic parameters of Set1 given in section 2.4.4. In Fig. 5.1 (a) with the color bar in logarithmic scale a micro-magnetic simulation is depicted obtained for simulation type Simu1 (see section 2.4.3). The result was subdivided in two field regimes. Regime 1 ranging from 0 mT to 25 mT showed first an increase of the most intense mode highlighted by white arrows until 15 mT and subsequent a decrease until 25 mT. This behavior is characteristic for an unsaturated magnetic film with a magnetic field pointing out-of-plane. For the out-of-plane component of the demagnetization field at 20 mT, we resolved an increased value in the middle of the magnetic disk [green ellipsoid in Fig. 5.1 (b)]. This was compared to the out-of-plane component of the demagnetization field at 70 mT [Fig. 5.1 (c)] of regime 2 ranging form 30 to 100 mT. For 70 mT we did not resolve this out of-plane component. Therefore we compared theory and simulation in regime 2.

The broken line in Fig. 5.1 (a) was evaluated using Ref. [KS86] assuming $k = 0$. The most intense mode highlighted with white arrows was in agreement with the theoretical calculated line and therefore named ferromagnetic resonance (FMR). The mode highlighted with the black arrow is attributed to the resonance of the magnetic disks. Additionally to these modes we resolve several further modes.

In Fig. 5.1 (a) and Fig. 5.1 (d) we show theoretical lines calculated assuming $G_{\mathrm{i}0}$ (blue lines) and $G_{0\mathrm{i}}$ (black lines), respectively, with $i = 1, 2, ..., 9$. For the calculations we used $H \perp G_{\mathrm{i}0}$ and $H \parallel G_{0\mathrm{i}}$ indicating MSSW and MSBVW configuration for the reciprocal lattice vectors, respectively. The blue and black lines are in agreement with the modes resolved additionally to the FMR mode and the magnetic disk resonance. These additional modes originate from the reciprocal lattice vectors and were MGC modes. The simulation data displays qualitatively the experimental results in chapter 8, because in experiment we also resolve several MGC modes.

5.2 Micro-magnetic simulation optimized for investigation of magnonic grating-coupler mode

In this section we present simulation data with geometric and magnetic parameters optimized to study MGC modes on the microscale. For the simulation we set the geometric and magnetic parameters of Set2 given in section 2.4.4. In the following we present results consecutively for all geometries depicted in Fig. 2.5.

In Fig. 5.2 we present a simulation excited with a magnetic field pulse (simulation type Simu1 in section 2.4.3). In the simulation we resolved several resonances. The resonance highlighted with white arrows is in agreement with the black line. For the line we assumed $k = 0$ [Ref. [KS86]]. Therefore the resonance observed in simulation was attributed to the FMR. The mode highlighted with red arrows was attributed to the magnetic disk resonance. We observed additional modes to the FMR and magnetic disk resonance. The resonances highlighted by black and green arrows were compared to theory (not shown) [KS86] and were identified as MGC modes originating from reciprocal lattice vectors. We related the resonances to G_{20} (green arrows) and G_{40} (black arrows). The MGC mode highlighted by black arrows intersected the magnetic disk resonance high-

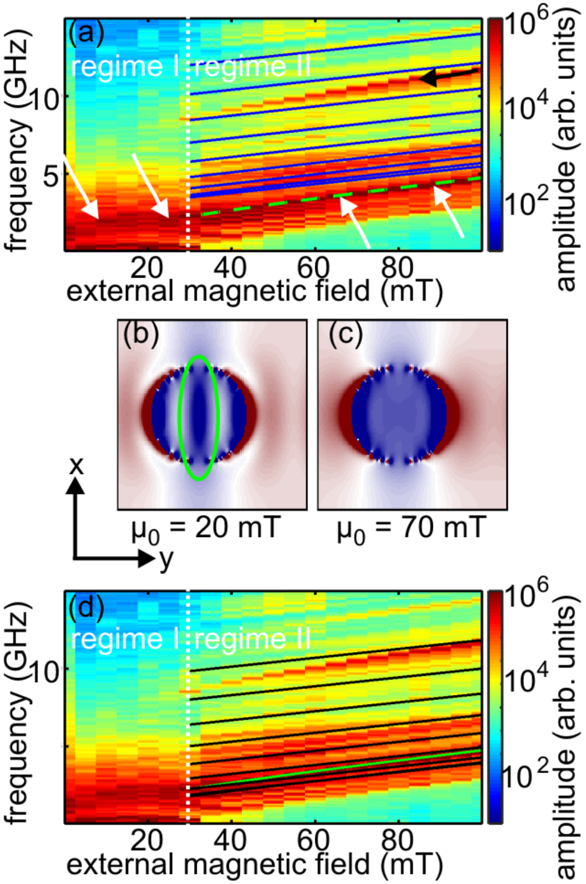

Figure 5.1: Micro-magnetic simulation obtained with the following parameters: $t = 200$ nm, $t_1 = 5$ nm, $t_2 = 15$ nm, $d = 350$ nm, periodicity $a = 700$ nm, $M_F = 140$ kA/m, $A_F = 3.32 \cdot 10^{-12}$ J/m, $M_D = 810$ kA/m and $A_D = 10.0 \cdot 10^{-12}$ J/m. (a) Field sweep simulation with the color bar in logarithmic scale. The lines were calculated with Ref. [KS86] assuming $k = G_{\mathrm{i}0}$ ($H \perp G_{\mathrm{i}0}$) for the blue lines with $i = 1, 2, ..., 9$ and $k = 0$ for the green line. (b) and (c) Out-of-plane demagnetization field for $\mu_0 H = 20$ mT and $\mu_0 H = 70$ mT with the magnetic field along the y axis. (d) Field sweep simulation with the color bar in logarithmic scale. The lines are calculated with Ref. [KS86] assuming $k = G_{0\mathrm{i}}$ ($H \parallel G_{0\mathrm{i}}$) for the black lines with $i = 1, 2, ..., 9$ and $k = 0$ for the green line.

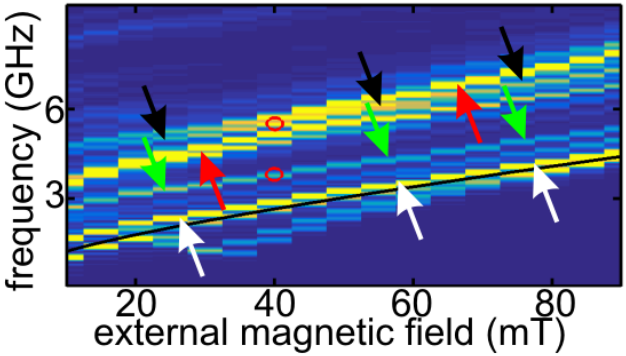

Figure 5.2: Micromagnetic simulation obtained for the following parameters: t = 20 nm, t_1 = 8 nm, t_2 = 16 nm, d = 350 nm periodicity a = 700 nm, M_F = 140 kA/m, A_F = $3.32 \cdot 10^{-12}$ J/m, M_D = 735 kA/m and A_D = $10.0 \cdot 10^{-12}$ J/m. For the black line we assumed $k = 0$ [Ref. [KS86]]. The red circles mark the external magnetic field and resonance frequencies used for simulations in Fig. 5.3.

lighted with red arrows. Because the MGC mode resonates at 40 mT at the same resonance frequency as the magnetic disks this mode is named resonant MGC mode. Therefore this simulation provides both a MGC mode and a resonant MGC mode. This allowed us to investigate both modes on the microscale.

Now we study propagating MGC modes. We applied an oscillating magnetic field to excite SWs using simulation type Simu2a (see section 2.4.3). The enlarged geometry allowed us to study propagating MGC modes. We studied the MGC mode highlighted by green arrows in Fig. 5.2. Therefore we set the external magnetic field to 40 mT and the excitation frequency to 3.8 GHz [lower red circle in Fig. 5.2]. The result of the simulation is depicted in Fig. 5.3 (a). Black and white indicated large spin-precessional amplitude. We resolved a propagating SW, but we resolved no spin-precessional motion of the magnetic disks. The reason was that the excitation frequency was below the resonance of the magnetic disks. We extracted the wavelength of the propagating SW by determining the spatial distance between different intensity maxima (white contrast) of the SW along the x axis. We obtained a wavelength of 360 nm for the propa-

gating SW.
Now we investigate the resonant MGC mode highlighted by black arrows in Fig. 5.2. Therefore we performed the same simulation, but we used a excitation frequency of 5.5 GHz. The result is shown in Fig. 5.3 (b). We resolve a propagating SW with spin precessional motion of the magnetic disks, because the MGC mode and the magnetic disks have the same resonance frequency. We extracted a wavelength of 171 nm.

The simulations shown in Fig. 5.3 (c) and (d) were obtained using simulation type Simu2b (see section 2.4.3), so we studied MGC modes at a SW interface. For the excitation frequency we used 3.8 GHz and 5.5 GHz, respectively. The SWs resolved in region 1 in Fig. 5.3 (c) and (d) were similar to the SWs resolved in Fig. 5.3 (a) and (b), respectively. But in Fig. 5.3 (c) and (d) the SWs were affected by the SW interface occurring due to omitted magnetic disk array in region 2. In Fig. 5.3 (c) we resolved SW wave packet beyond the SW interface (green cuboid). The simulation in Fig. 5.3 (d) revealed SW channels beyond the SW interface (red cuboids). Interestingly the pattern of the SW channels in Fig. 5.3 (d) varied depending on the SW propagating direction. This became apparent by comparing the pattern of the SW channels in the red cuboids. These effects are interesting and show that the SW interface modified SWs.
The SWs in Fig. 5.3 (c) and (d) in region 2 showed a larger intensity at the same distance of the excitation area compared to the results presented in Fig. 5.3 (a) and (b), respectively. This accounted for both the MGC mode and the resonant MGC mode. We suggest that by omitting of the magnetic disks the SW is damped less and therefore the decay length is increased.

Now we investigate the geometry in Fig. 2.5 (b) using simulation type Simu2c (see section 2.4.3). In addition we performed a spatio-temporal Fast-Fourier-Transformation (FFT) along the x axis in Fig. 2.5 (b). The result is shown in Fig. 5.4. The data revealed the band structure of the investigated MGC. We resolved the dispersion of the magnetic film highlighted by green arrows and the dispersionless resonance of the magnetic disks highlighted by black arrows in Fig. 5.4. In the data we resolved Brillouin zone boundaries at $(4.5 \pm n \cdot 9)$ rad/μm with $n = 1, 2, ...$ highlighted by black lines. The Brillouin zones occurred due to the reciprocal lattice vectors $G_{\mathrm{i}0}$, because the FFT was performed along the x axis. The value 9 rad/μm corresponded to the periodicity a of 700 nm with $2\pi/a$. In Fig.

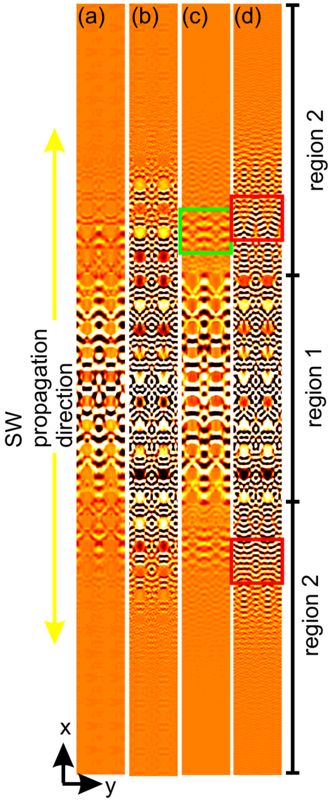

Figure 5.3: (a) and (b) Micromagnetic simulation obtained with the geometry in Fig. 2.5 (b). The external magnetic field was applied along the *y* axis. The excitation frequency was set to 3.8 GHz in (a) and 5.5 GHz in (b). (c) and (d) Micromagnetic simulation obtained with the geometry in Fig. 2.5 (c). The external magnetic field was applied along the *y* axis. The excitation frequency was set to 3.8 GHz in (c) and 5.5 GHz in (d). White and black indicates large spin-precessional motion.

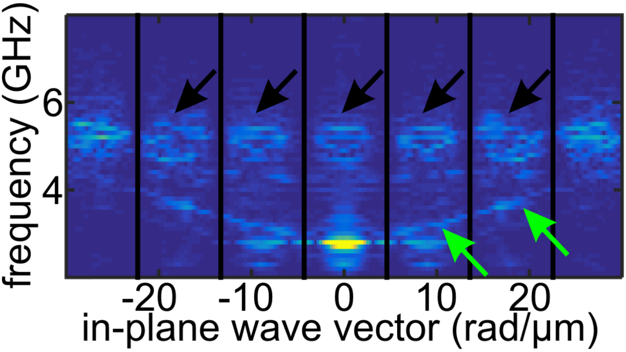

Figure 5.4: Micromagnetic simulation using Simu2c in section 2.4.3. We used a magnetic field pulse to excite the SWs. The green arrows highlight the dispersion of the film and the black arrows highlight the dispersion of the magnetic disks.

5.4 we directly observed the origin of the MGC modes. The dispersion relation of the magnetic film was backfolded by the reciprocal lattice vectors. We obtained MGC modes not present in a bare magnetic film [YDH$^+$13].

5.3 Discussion and conclusion

The MGC modes investigated in Fig. 5.2 were attributed to the reciprocal lattice vectors G_{20} (green arrows) and G_{40} (black arrows). The extracted reciprocal lattice vectors were correlated with their wavelengths using $\lambda = 2\pi/G_{\mathrm{ij}}$. Therefore the MGC mode corresponded to a wavelength $\lambda = 2\pi/G_{20}$ = 350 nm and the resonant MGC mode to a wavelength $\lambda = 2\pi/G_{40}$ = 175 nm. For the same MGC modes in section 5.2 we obtained for the wavelengths 360 nm and 171 nm, respectively, by extracting the wavelengths of spatial resolved simulations [Fig. 5.3 (a) and (b)]. The wavelengths determined using reciprocal lattice vectors in Fig. 5.2 coincide with the wavelengths extracted from spatial resolved simulations. We conclude that using reciprocal lattice vectors (or empty lattice model) is suitable for determining the wavelength of MGC modes. This is particular important, because we used the empty lattice model in chapter 6, 8 and 9 to investigate experimentally observed MGC modes. Furthermore we clarified the origin of the MGC modes in magnetic films. MGC modes occurred by backfolding of the dispersion relation of the magnetic film by reciprocal lattice vectors.

6 Investigation of low damping 20 nm thick yttrium iron garnet grown with pulsed laser deposition

In this chapter we study a YIG film grown with PLD [SSC$^+$12]. The YIG film investigated in this chapter had a thickness of 20 nm and was nominal identical to the film in Ref. [HRH$^+$16]. This film exhibited the lowest Gilbert damping α found up to now for nanometer YIG films grown with PLD. We characterized the YIG film by preparing CPWs on top of the bare YIG film. The experiments we performed were similar to Ref. [YdKC$^+$14] for a 20 nm YIG film grown with PLD by different supplier [dKAB$^+$13]. We compared the data obtained in this chapter to the results in Ref. [YdKC$^+$14]. Additionally we nanostructured the YIG film. Both the sample fabrication and the geometric parameters are given in section 4.2.2. We investigated the MGC effect for etched nanothroughs and partially embedded nanodisks. The data is compared to the results of Ref. [YdKC$^+$16]. In Ref. [YdKC$^+$16] the authors added magnetic nanodisks to a 20 nm YIG film which were not embedded.

6.1 Investigation of a bare and nanostructured 20 nm thick YIG film

To characterize the 20 nm thick YIG film we fabricated two CPWs on top of YIG film. The geometric parameters and the excitation amplitudes of the CPW are given in section 3.1.5. The sample fabrication is described in section 4.2.2. For the CPW a maximum excitation amplitude occurred at $k_\mathrm{I} = 0.9$ rad/μm. The data was obtained with the setup described in section 3.1. Consistent with Ref. [YdKC$^+$14] we used a spacing $s = 30$ μm for the CPWs. The microwave power amounted to 0 dBm. The external magnetic field was applied in-plane at an angle of $\theta = 0$ deg (MSSW configuration) [Fig. 3.4 (a)]. For the linear magnitude of ΔS_{11} we resolve the spectrum shown in Fig. 6.1 (a). A similar spectrum was obtained for the linear magnitude of ΔS_{22} (not shown). For both spectra we resolved the

k_I excitation. In Fig. 6.1 (b) we show the imaginary part of ΔS_{12}. The branch is attributed to magnetic cross-talk. This is in contrast to the results found in Ref. [YdKC$^+$14]. In Ref. [YdKC$^+$14] the spectra showed propagating SWs for k_I and higher excitations of the CPW.
Besides the bare YIG film we investigated two nanostructured samples depicted in Fig. 4.4. Sample TMGC01 in Fig. 4.4 (a) consisted of nanothroughs and sample TMGC02 in Fig. 4.4 (b) and (c) represented a bicomponent MGC. The geometric parameters are given in Tab. 4.2.
In Fig. 6.1 (c) we show spectra of the sample TMGC01 (linear magnitude of ΔS_{11}). Besides the k_I excitation we resolved a mode (highlighted by red arrows) not present in the bare YIG film. The additional resolved modes were attributed to the MGC effect [YDH$^+$13] originating from the reciprocal lattice vectors introduced by the periodic lattice of the nanothroughs. Using the formalism of Ref. [KS86] and the same parameters for YIG as in chapter 7 ($M_S = 140$ kA/m, $A = 3.32 \cdot 10^{-12}\ J/m$, $\gamma/2\pi = 28.3$ GHz/T) we assigned the additional branch to the wave vector $-k_\mathrm{I} + G_{10}$.

In Fig. 6.1 (d) data of the linear magnitude of ΔS_{11} is depicted of sample TMGC02. Besides the k_I excitation we resolved the resonance of the Py nanodisks (highlighted by blue arrows) and three further modes (highlighted by red arrows) not resolved in the bare YIG film. These new modes were attributed to the MGC effect. For TMGC02 we evaluated the wave vectors $-k_\mathrm{I} + G_{10}$, $-k_\mathrm{I} + G_{20}$ and $-k_\mathrm{I} + G_{30}$ for the new modes using the formalism of Ref. [KS86] and the same parameters for YIG as above. We resolved the higher MGC modes ($-k_\mathrm{I} + G_{20}$ and $-k_\mathrm{I} + G_{30}$) due to the presence of the Py nanodisk array, when these modes intersect with the FMR branch of the Py nanodisks. This was different from previous experiments. In Ref. [YdKC$^+$16] higher MGC modes were present over the whole range of the external magnetic field.

6.2 Discussion and conclusion

We now discuss the ΔS_{12} imaginary part obtained for the bare 20 nm thick YIG film depicted in Fig. 6.1 (b). We did not resolve propagation signal from SWs. This is surprising as a nominally identical YIG film grown by the same group showed the lowest Gilbert damping α ever reported for

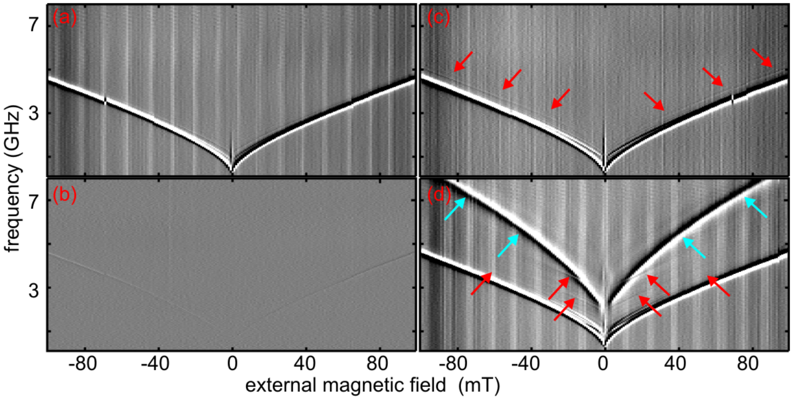

Figure 6.1: Field sweep measurements for a bare YIG film and the samples TMGC01 and TMGC02. (a) Spectra (linear magnitude of ΔS_{11}) of a bare YIG film in MSSW configuration at $\theta = 0$ deg. (b) Spectra (imaginary part of ΔS_{12}) of a bare YIG film in MSSW configuration at $\theta = 0$ deg. (c) Spectra (linear magnitude of ΔS_{11}) of sample TMGC01 in MSSW configuration at $\theta = 0$ deg. (d) Spectra (linear magnitude of ΔS_{11}) of sample TMGC02 in MSSW configuration at $\theta = 0$ deg.

20 nm thick YIG [HRH$^+$16]. In Ref. [YdKC$^+$14] a PLD grown film supported propagating SWs over $s = 30$ μm. In Ref. [YdKC$^+$14] a nominally identical film of Ref. [dKAB$^+$13] was used. If we compare the linewidth at zero magnetic field ΔH_0 of both YIG films, we recognize that ΔH_0 of the YIG film we used amounted to 3.3 Oe and consequently to more than double the value compared to 1.4 Oe in [dKAB$^+$13]. The larger value of ΔH_0 of the YIG film used might have reduced the decay length of the SWs.

We conclude that for a large SW decay length not only the Gilbert damping α but also ΔH_0 has to be minimized. Large decay lengths for SWs are advantageous for future application of magnonics to minimize the loss of magnonic devices.

7 Investigation of bare 200 nm yttrium iron garnet thin film grown by liquid phase epitaxy

With LPE it is possible to grow large wafer areas homogeneously suitable for future magnonic circuits. But commercially grown YIG films using LPE had a thickness of 1 μm or beyond [SCH10] not suitable for application in nanomagnonics. In this chapter we report on BSWS (section 3.1) performed on a YIG thin film with a thickness t of 200 nm. The YIG thin film was grown with LPE on a GGG substrate [Mat]. We demonstrate in this chapter that the thin YIG film exhibited convincing magnetic characteristics. Therefore we used the YIG film in the subsequent chapters for sample fabrication.

First we evaluated the relevant magnetic parameters (saturation magnetization M_S, exchange constant A, gyromagnetic ratio γ and damping constant α). We analyzed SW properties as the SW wavelength, group velocity, nonreciprocity and decay length. The experimental data is modeled using the approach of Ref. [KS86].

7.1 Determination of magnetic parameters of 200 nm thick yttrium iron garnet film

We conducted a measurement with the external magnetic field out-of-plane for the bare YIG film using CPW with a 20 μm wide signal line and measuring at three different temperatures [Fig. 7.1][Sch13]. The geometric parameters of the CPW are described in section 3.1.5 and the fabrication of the CPW in section 4.4. The external magnetic field was applied out-of-plane, because it allowed the direct determination of three magnetic parameters: saturation magnetization M_S, gyromagnetic ratio γ and damping constant α. We swept the external magnetic field from 1000 mT to 0 mT in steps of 40 mT. We extracted the damping parameter α for three different temperatures. We used the linear magnitude of ΔS_{12} and fitted the resulting line plots at different external magnetic field using a Lorentzian. Of the

temperature T [K]	damping α
50	$8.4 \cdot 10^{-4}$
150	$1.5 \cdot 10^{-4}$
300	$1.0 \cdot 10^{-4}$

Table 7.1: Temperature dependent damping α extracted from Fig. 7.2 (a).

fitted function we extracted the linewidth and the resonance frequency. By plotting the linewidth over the resonance frequency [Fig. 7.2 (a)] we extracted the damping by evaluating the slope of the different lines according to $\alpha = \frac{m}{2 \cdot \sqrt{3}}$ with m being the slope of the line.

The factor $\sqrt{3}$ had to be used, because we extracted the linewidth of the linear magnitude [Sta93]. We obtained the damping for the 200 nm YIG film summarized in Tab. 7.1. The damping decreased with increasing temperature and at 300 K we obtained the smallest damping parameter α of $1.0 \cdot 10^{-4}$. Our value of $\alpha = 1.0 \cdot 10^{-4}$ is similar to the value of $\alpha = 1.2 \cdot 10^{-4}$ found very recently for a 106 nm thick YIG film grown by LPE [DSL$^+$17]. It is a factor of 5.5 better than the value found for 82 nm thick YIG grown by PLD [KGK$^+$17], and larger compared to PLD-grown and sputtered YIG [CLZ$^+$14, HRH$^+$16].

In Fig. 7.2 (b) we plotted the resonance frequency over the external magnetic field for 300 K. We assumed an error of 2 % for the external magnetic field to take into account that the sample is not in the center of the applied external magnetic field or the sample surface is not perpendicular to the external magnetic field. We used a linear function to fit the data. From the slope we extract $\gamma/2\pi = 27.5 \pm 1.1$ GHz/T. From the intersection point of the line and the x axis in Fig. 7.2 (b) we obtained the saturation magnetization M_S. In Fig. 7.1 (c) the resonance frequency amounted nearly 0 GHz for nonzero magnetic field value highlighted by a green arrow. At this point the magnetization was rotated perpendicular to the film surface and the external magnetic field and the demagnetization field canceled each other. The external magnetic field had the same value as the saturation magnetization. M_S amounts to 139 ± 15 kA/m. In the following chapters we used 28.3 GHz/T [CLZ$^+$14] for the gyromagnetic ratio and 140 kA/m [CLZ$^+$14] for the saturation magnetization, because

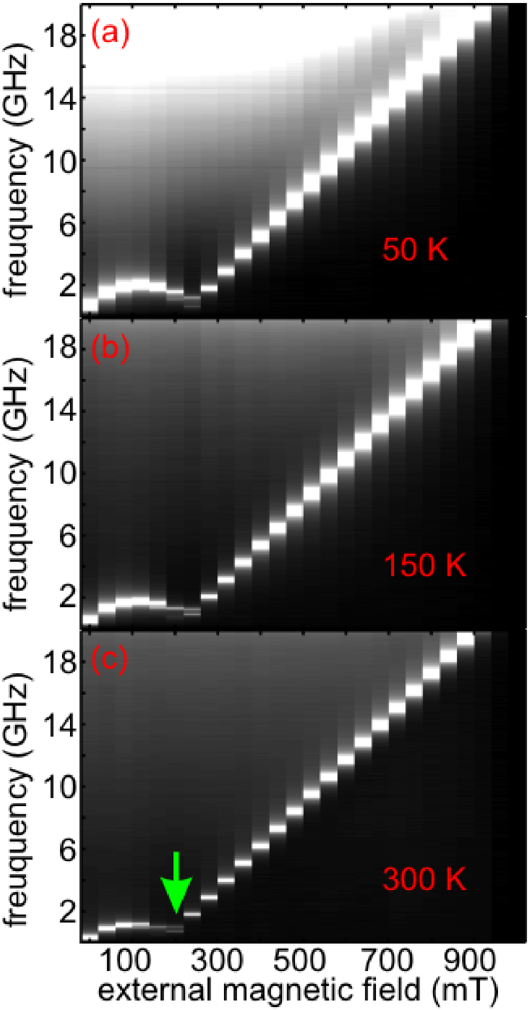

Figure 7.1: Spectra obtained for YIG thin film with external magnetic field pointing out-of-plane. The measurement was obtained for 3 different temperatures: 50 K, 150 K and 300 K. For the evaluation of the spectra we applied method 1 in section 3.1.8.

these values were determined with an error ten times smaller than the error of our measurement. Both values were within the error bar of our measurements.

To extract the exchange constant A we used an angle scan measurement with an in-plane field of 16 mT of a bare YIG film with an integrated CPW. The experimental details are described in chapter 3.1. We used the CPW with $w = 2.1$ μm with a maximum excitation amplitude at $k_\mathrm{I} = 0.9$ rad/μm (section 3.1.5). The CPW preparation is given in section 4.1. In Fig. 7.2 (c) we show ΔS_{11} of the linear magnitude. Using the formalism of Ref. [KS86] we fitted the PSSW of first order ($p = 1$) [red dashed line in Fig. 7.2 (c)] to extract the exchange constant A. We obtained $3.32 \pm 0.02 \cdot 10^{-12}$ J/m. This is in agreement with Refs. [dKAB$^+$13, KWG60, EP59].

7.2 Spin-waves excited in a 200 nm thick yttrium iron garnet film using a coplanar waveguide

We used the nominal identical YIG film as in the section before to prepare our samples. For the investigation we prepared two integrated CPWs ($w = 2.1$ μm) on top of the sample. The geometric parameters and the Fourier analysis in dependence of the SW wave vector k are given in section 3.1.5. Fabrication of the sample and CPW are given in section 4.1. For the investigation of SWs we applied BSWS [chapter 3.1]. We investigate S_{12} and S_{21} between two neighboring CPWs [Fig. 3.4 (a)]. The in-plane component of $\mathbf{k}$ is orientated perpendicular to the signal line. The output power in this section of the VNA was set to -20 dBm, if not stated otherwise. For the experiment we utilized an external magnetic field $\mathbf{H}$ in the plane of the sample at different angles θ. To obtain v_g (nonreciprocity β) we take the imaginary part (magnitude) of S_{12} and S_{21}.
In Fig. 7.3 (a) we present spectra of ΔS_{12} (imaginary part) with H parallel to the CPW ($\theta = 0$ deg). For large H we obtained MSSW configuration with the magnetization $\mathbf{M}$ perpendicular to $\mathbf{k}$. In Fig. 7.3 (a) we resolved oscillating signal (white - positive values, black - negative values) indicating propagating SWs between the CPWs in Fig. 3.4 (a) [BOF03]. The spectra at positive H and the lineplots along 16 mT [Fig. 7.3 (b) and (c)] revealed up to seven different modes. For the calculation of the field dependent eigefreqeuncies we used the formalism of Ref. [KS86] [dashed

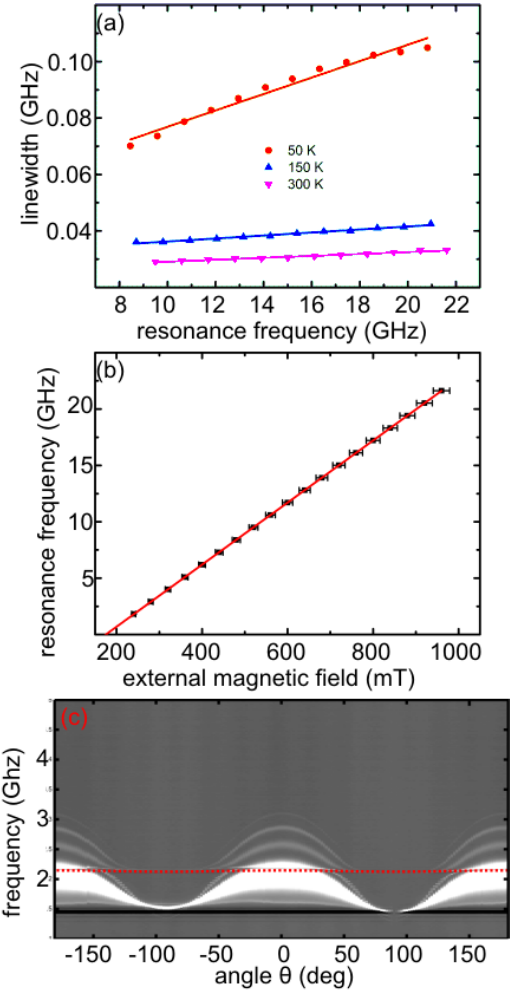

Figure 7.2: The depicted data in (a) and (b) is extracted from Fig. 7.1. (c) In-plane measurement with an external magnetic field of 16 mT using the setup in chapter 3.1. The measurements are used to evaluate the magnetic parameters of the 200 nm YIG thin film, i.e. saturation magnetization M_S, damping α, gyromagnetic ratio γ and the exchange constant A.

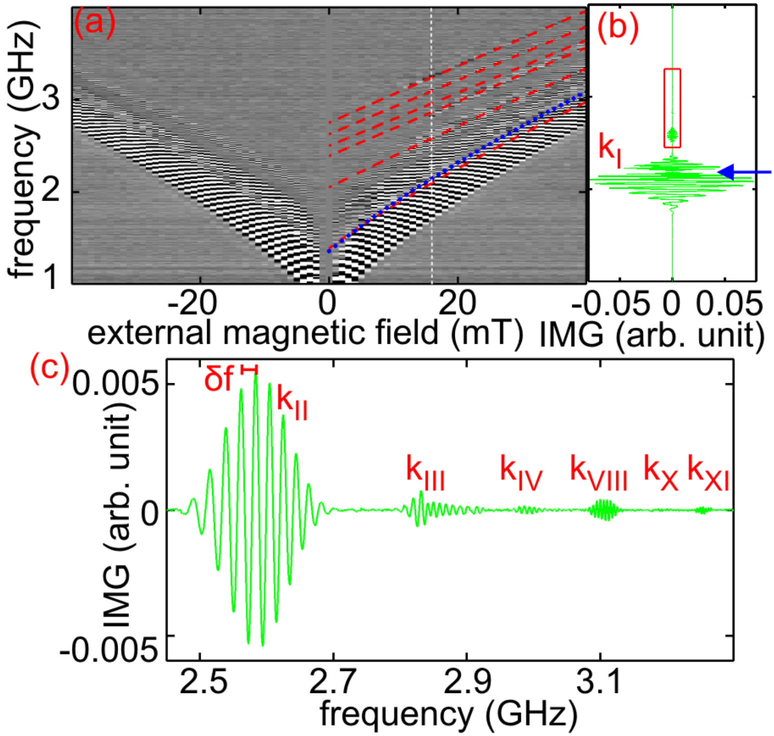

Figure 7.3: (a) Spectra of the imaginary part (IMG) (ΔS_{12}) for MSSW configuration (white - positive values, black - negative values). For the calculation of the spectra we applied method 1 in section 3.1.8. The red and blue broken lines represent eigenfrequencies calculated with Ref. [KS86] assuming fixed k. (b) Line plot of the spectrum obtained at 16 mT [white dashed line in (a)]. The node highlighted by a blue arrow is assigned to an anticrossing between a MSSW and PSSW. (c) Data taken from the rectangular box in (b). The oscillating signal was assigned to propagating SWs. Labels were used to indicate resolved oscillations.

parameter	k (rad/μm)	λ (μm)	v_{g} (km/s)
k_{I}	0.9	6.98	2.58
k_{II}	2.5	2.51	1.32
k_{III}	4.5	1.40	0.66
k_{IV}	5.9	1.06	0.48
k_{VIII}	13.5	0.47	0.30
k_{X}	16.9	0.37	0.30
k_{XI}	20.0	0.31	0.24

Table 7.2: SW properties obtained from Fig. 7.3 at 16 mT. We give the values for the SW wave vectors k, corresponding wavelengths $\lambda = 2\pi/k$ and group velocities v_{g}

lines in Fig. 7.3 (a)]. Using the excitation spectrum of the CPW in Fig. 3.5 we extracted the wave vectors k for each propagating SW indicated by the labels in Fig. 7.3 (b) and (c). The extracted values are listed in Tab. 7.2. The largest wave vector found was $k = 20.0$ rad/μm corresponding to a SW wavelength of 310 nm. Going to negative H, we obtain less modes due to the nonreciprocity of the MSSW. The nonreciprocity is discussed below.

In the spectrum depicted in Fig. 7.3 (b) we resolved a specific node (arrow) in the signal indicated with k_{I}. The node suggested that for a specific frequency the propagating SW is suppressed. We explain the suppression as an anticrossing between the MSSW mode ($\mathbf{M} \perp \mathbf{k}$) and the PSSW mode of first order ($p = 1$) [Grü89]. The dotted line in Fig. 7.3 (a) represents the calculated eigenfrequency of the PSSW mode of first order ($p = 1$) [KS86]. With the line we could model the field dependence of the node, i.e., the signal suppression. The eigenfrequency of the PSSW of first order ($p =, 1$) is nearly independent of the in-plane wave vector k for small k. We could reproduce the center frequency of the gap with its eigenfrequency.

7.2.1 Group velocity in dependence of the external magnetic field and the wave vector

We calculated the group velocities v_g of the SWs. From the oscillating signal presented in Fig. 7.3 (a) we could extract the group velocity in dependence of H or k using Eq. 3.12. For Fig. 7.4 (a) we used the wave vector k_I [Fig. 3.5] showing the most intensive signal to summarize the values v_g (symbols) as a function of H. The maximum group velocity was found at 1 mT and amounted to 5.4 km/s. With increasing H at fixed k the group velocity decreased continuously as commonly observed [YHS$^+$12, KGK$^+$17]. The value of 5.4 km/s exceeded the value by a factor four reported by Yu et al. [YdKC$^+$14] for 20 nm thin YIG. Due to the larger thickness t of the YIG film utilized in this chapter the dipolar forces were increased. In consequence the slope $v_\mathrm{g} = 2\pi df/dk$ of $f(k)$ was increased at small k. For PLD grown YIG with a thickness of 82 nm similarly large values have been observed, but for modeling a growth-induced magnetic anisotropy had to be included [KGK$^+$17].

Now we present the dependence of v_g (symbols) on wave vector k for fixed field $\mu_0 H = 16$ mT in Fig. 7.4 (b). For this value of H we resolved seven modes as shown above. We obtained the maximum group velocity of 2.6 km/s for the wave vector k_I. With increasing k, v_g decreased and then seems to level off. The extracted values are listed in Tab. 7.2. The data in Fig. 7.4 (a) and (b) was modeled using Ref. [KS86]. The lines indicate the calculated dependencies. For $\mu_0|H| \geq 5$ mT we obtained a good quantitative agreement of experiment and theory. In Fig. 7.4 (c) we present the dispersion relation $f(k)$ at 16 mT as a line. The evolution of $f(k)$ indicates that we addressed both dipolar (magnetostatic) and dipole-exchange SWs in the thin YIG with our experiment [GM96]. In the wave vector range from 7 $\mathrm{r}ad/\mu\mathrm{m}$ to 12 $\mathrm{r}ad/\mu\mathrm{m}$, the resonance frequency $f(k)$ is nearly constant. Thus we expected that $v_\mathrm{g} = 2\pi df/dk$ is (vanishingly) small. For the wave vectors k_V, $k_{\mathrm{V}I}$, $k_{\mathrm{V}II}$ and $k_{\mathrm{I}X}$ we did not obtain propagation signal in the spectrum of Fig. 7.3 (c). But for this wave vectors we calculated that the SW dispersion relation is flat. It follows that v_g went to zero. Therefore the decay length of this SWs was small [Eq. 2.39] consistent with the experimental observation. But a SW attributed to $k_{\mathrm{V}III}$ was resolved. In case of $k_{\mathrm{V}III}$ we obtained a local maximum for both components h_x and h_z in Fig. 3.5. We suggest that the summed torque acting on the spins might have produced a SW amplitude that was still sufficient to reach the detector although v_g is small.

7.2.2 Nonreciprocity of the yttrium iron garnet film

In Fig. 7.4 (d) we present the nonreciprocal characteristics of the thin YIG film. We extracted the nonrecirpocity parameter β for the k_I excitation for both the MSSW ($\theta = 0$ deg) and BVMSW configuration ($\theta = 90$ deg). We took the linear magnitude of ΔS_{12} and ΔS_{21} (for calculation we applied method 1 in section 3.1.8) at different H and extracted the maximum amplitude a. To obtain the nonreciprocity we applied Eq. 3.13. For BVMSW modes β was close to 0.5. This indicated reciprocal behavior consistent with Ref. [CTK$^+$10]. In contrast for the MSSW mode we found a large nonreciprocity β with values up to 0.9 (0.1) for S_{12} (S_{21}) at large H of 100 mT. When reducing H the nonreciprocity β of S_{12} decreased consistent with findings for ferromagnetic metals [JKS$^+$13]. The field dependence of β for the MSSW mode was modeled [solid lines in Fig. 7.4 (d)] using the intrinsic nonreciprocity of the MSSW [MVC$^+$06] combined with the direction-dependent excitation characteristics of our antenna [DKR$^+$09] (see modeling in section 2.3.5). Experiment and theoretical calculation were in agreement. The observed characteristics can be employed for nonreciprocity-based magnonic devices [JKS$^+$13].

7.2.3 Decay length of spin-waves in the yttrium iron garnet film

Now we analyze the decay length l_d of propagating SWs. Therefore a YIG sample was placed face-down on two different sets of 2 mm long CPWs and a signal line width of 3 μm. The geometric parameters of the CPW are described in section 3.1.5 and the sample fabrication in section 4.4. The sample size amounted to 2 x 8 mm^2. To prohibit reflections both ends were cut at 45 deg. The simulated value of the k_I excitation of the CPWs was determined to be 0.4 rad/μm [section 3.1.5]. In Fig. 7.5 we present the signal ΔS_{12} obtained for a separation $s = 2$ mm between two neighboring CPWs. The separation s of the CPWs was a factor 28.5 larger than in Ref. [CGE$^+$17]. In the spectrum of ΔS_{12} obtained for -20 mT we resolved an oscillating signal indicating propagating SWs (inset). The signal resolved for ΔS_{12} and a spacing s of 1 mm for the CPWs (not shown) was larger by a factor of 2.5. In Fig. 7.5 (b) we summarized the resolved signal strengths

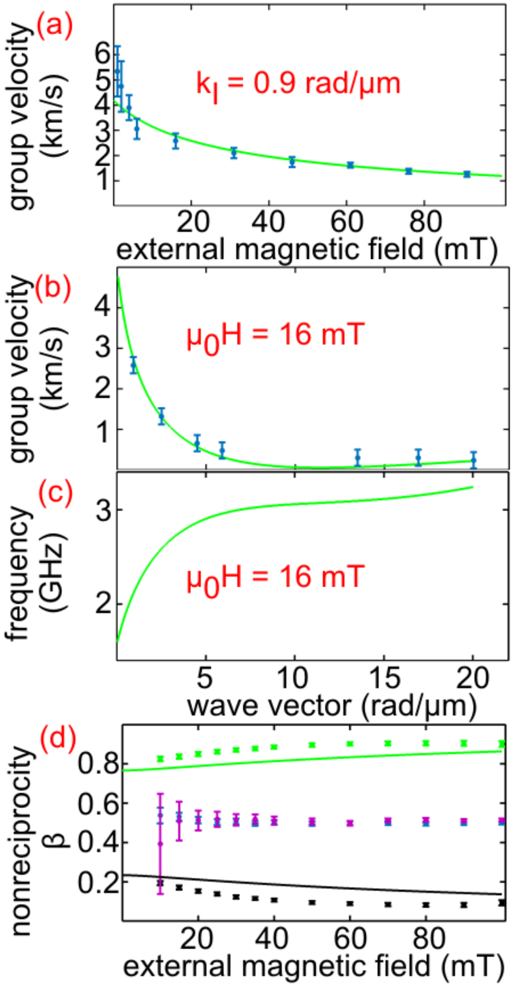

Figure 7.4: (a) Group velocity in dependence of H obtained for MSSW configuration and the wave vector k_I (symbols). (b) Group velocities in dependence of k (symbols) and (c) theoretical dispersion relation $f(k)$ at 16 mT. We extracted the experimental values from the spectra depicted in Fig. 7.3 (a) to (c). For the calculation of the lines in (a) to (c) we applied the formalism of Ref. [KS86]. (d) For SWs with wave vector k_I the nonreciprocity parameter β was extracted for MSSW (top and bottom most symbols) and BVMSW configuration (central symbols). The top most (bottom most) symbols represent S_{12} (S_{21}) obtained at $H > 0$. The lines represent the evaluated nonreciprocity in MSSW configuration.

for varying s. We obtained the data point at $s = 0$ when considering the nonreciprocity in the given MSSW configuration. From the straight line we evaluated a decay length of $l_\mathrm{d} = 0.86 \pm 0.05$ mm.

7.3 Discussion

We use Eq. 2.39 to evaluate the decay length l_d from the Gilbert damping parameter of $\alpha = 1.0 \cdot 10^{-4}$ obtained with the magnetic field out-of-plane [section 7.1] by which two-magnon scattering was suppressed [AM99]. For this purpose we utilized $\tau = \frac{1}{2\pi\alpha f}$ [Sta93] and obtained $l_\mathrm{d} = 2.2$ mm. In this case f indicated the resonance frequency at $k = 0$. For the FMR frequency we used $f = 1.78$ GHz at 20 mT, an ellipticity factor of one [KP75] and $v_\mathrm{g} = 2.5$ km/s. The theoretical value of τ was a factor of 2.6 larger than the value extracted from experiment. The discrepancy was ascribed to the scattering of propagating SWs at both defects in YIG and the regions where CPW ground lines modified $f(k)$ [YdKC$^+$14, CGE$^+$17]. Furthermore due to the flip-chip geometry the separation of sample and CPWs might be varied by a dust particle inducing an unintentional amplitude variation in the different data points of Fig. 7.5 (b). Following these aspects, the experimentally determined decay length of 0.86 mm for the LPE-grown YIG film was reasonable.

Now we present recently published values for decay lengths l_d of thin YIG fabricated on small substrates by PLD. Assuming a fixed damping parameter α, τ becomes large for small f of a MSSW [Sta93]. This accounts also for v_g [YHS$^+$12]. A decay length of 0.58 mm was observed at a frequency of 1.1 GHz and a group velocity $v_\mathrm{g} = 1.16$ km/s for 20 nm thick YIG and an applied in-plane field of 5 mT [YdKC$^+$14]. For the 20 nm tick YIG the damping parameter α was $2.3 \cdot 10^{-4}$. A microstructured waveguide fabricated from 20 nm thick YIG showed a consistently smaller decay length of 0.025 mm at 45 mT with $v_\mathrm{g} = 0.35$ km/s, $\alpha = 4 \cdot 10^{-4}$ and $f = 3$ GHz [CGE$^+$17]. We point out that for a thin film with fixed thickness, l_d in general decreases with increasing field (or increasing frequency). The same holds true for the MSSW in the dipolar regime when reducing the waveguide width. In Ref. [TDS$^+$17], 40 nm thick YIG was produced by magnetron sputtering obtaining $3.1 \cdot 10^{-4}$ for the damping parameter α. It was reported that at 6 GHz and 130 mT spin-wave signals

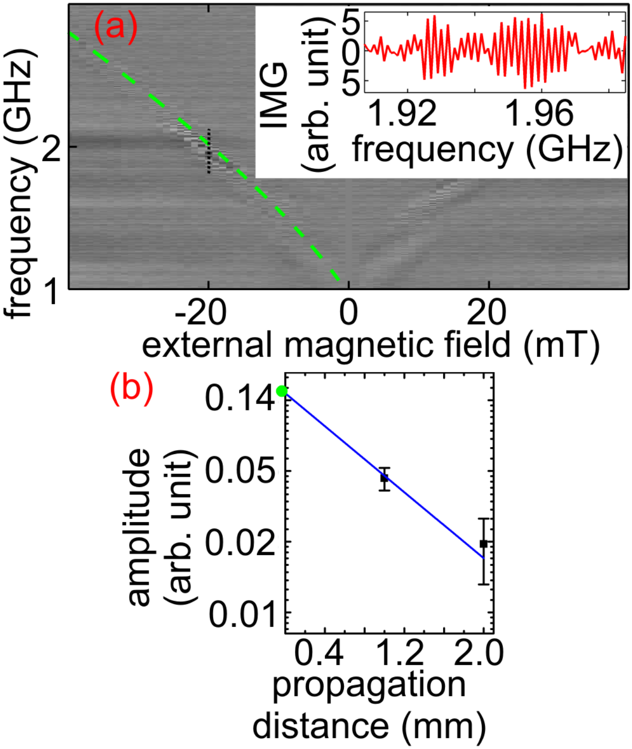

Figure 7.5: (a) Spectra ΔS_{12} (imaginary part) measured for the YIG film in flip-chip geometry. The distance of the two parallel CPWs was 2 mm. H was oriented parallel to the CPWs (MSSW configuration). The inset shows the imaginary part (IMG) of ΔS_{12} extracted at -20 mT (vertical broken line). The dashed line reflects the evaluated eigenfrequencies for the wave vector k_{I} [KS86]. For the calculation of the spectra we applied method 1 in section 3.1.8. (b) Extracted amplitudes taken from ΔS_{12} for k_{I}. We normalized the amplitudes to ΔS_{22} taken at -20 mT for two different s. The microwave power of the VNA amounted to -10 dBm. For $s = 0$ we show the normalized signal strength assuming the nonreciprocity parameter $\beta = 0.15$ for the given MSSW configuration. From the solid line we calculated a decay length of 0.86 mm.

were transmitted up to 0.15 mm by an edge mode. The values reported in Refs. [YdKC$^+$14, CGE$^+$17, TDS$^+$17] are larger compared to the scattering length (mean free path) of electrons (which is typically on the order of 0.0001 mm). This allows for coherent processing of information in a mesoscopic network. Nevertheless larger decay lengths are still advantageous to reduce the loss of magnonic devices. To ensure large v_g and large l_d in the long wavelength limit, small frequencies near 1 GHz are usually required [YdKC$^+$14, KGK$^+$17]. SWs in the exchange regime approaching wavelengths smaller than 100 nm can also possess large v_g in thin YIG [YdKC$^+$16]. But relevant decay lengths have not yet been thoroughly investigated. Therefore SWs in the exchange regime with wavelength down to 100 nm will be investigated in more detail in chapter 8 addressing group velocity and propagation distance.

7.4 Conclusion

In conclusion we presented a 200 nm thick YIG film grown by LPE that supported SWs with a group velocity of up to 5.4 km/s, a large nonreciprocity of $\beta = 0.9$ and small SW wavelengths down to 310 nm by using a conventional CPW. We attributed the large β to the combined nonreciprocity of both the excited MSSW and the direction-dependent excitation characteristics of the microwave antenna. For a SW with a frequency of about 2 GHz we resolved propagation over a distance of 2 mm between two CPWs. Importantly, using LPE leads to thin epitaxial YIG of high quality on large-area GGG substrates. LPE is complementary to magnetron sputtering that already provided YIG with extremely low damping parameters. Long decay lengths are advantageous for coherent information processing in integrated nanomagnonic networks at low power consumption.

8 Magnonic grating-coupler composed of a 200 nm thick YIG film and a Py nanodisk lattice

In this chapter we discuss the MGC effect in experiment first observed by H. Yu et al. [YDH$^+$13]. A MGC consists of a ferro- or ferrimagnetic thin film and ferromagnetic nanodisks (nanostripes) arranged in a periodic lattice. For the 2D grating coupler one can arrange the nanodisks in one of the five 2-dimensional Bravais lattices. We used a square shaped lattice in the following. For the base of the Bravais lattice differently shaped nanostructures could be considered. We used a circularly shaped flat nanodisk to exploit an equally shaped anisotropy for all in-plane field directions that we applied. Furthermore the disks were fabricated as thin as possible and embedded partially into the thin film material [Fig. 4.2] to reduce the magnetic stray field and obtain a homogeneous internal magnetic field in the ferrimagnetic film. In consequence we could use an empty lattice model for the comparison of theoretical and experimental data in this chapter.

8.1 Broadband spin-wave spectroscopy on magnonic grating-coupler

The sample was prepared from a YIG thin film with a thickness t = 200 nm nominally identical to the 200 nm thick YIG film of chapter 7. For the experiments we used 4 different sample geometries. Both sample fabrication and geometric parameters are given in section 4.2.1. The geometric parameters and the excitation amplitudes of the CPW are given in section 3.1.5. For the integrated CPW (width signal line: 2.1 μm) a maximum excitation amplitude occurs at $k_\mathrm{I} = 0.9$ rad/μm. For the investigation of SWs we utilized the setup described in chapter 3.1.

From the Py reference film in Fig. 8.1 (a) we extracted an uniaxial anisotropy field between 2 to 3 mT. The uniaxial anisotropy is also observed for the Py nanodisks. In Fig. 8.1 (b) we show an angle scan measurement of sample MGC01 for an external magnetic field of 70 mT (the

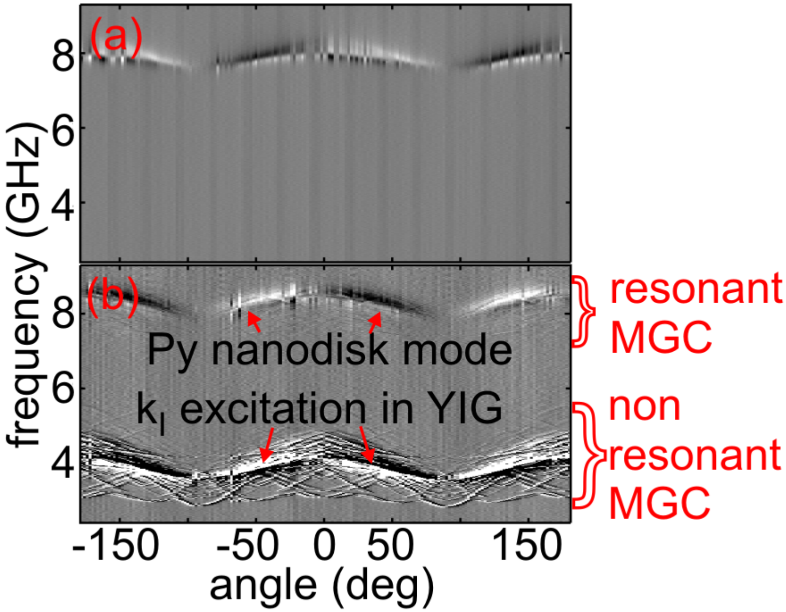

Figure 8.1: Angle scan measurements for a Py thin film and a sample composed of YIG with a Py nanodisk array at an external magnetic field of 70 mT (white - positive values, black - negative values). (a) Spectra showing the linear magnitude of ΔS_{12} obtained for Py thin film in flip chip geometry (width of signal line CPW: 20 μm). (b) Spectra showing the linear magnitude ΔS_{11} of a YIG film with a Py nanodisk array using an integrated CPW $w = 2.1$ μm.

origin of the modes in Fig. 8.1 (b) is discussed in section 8.1.1 in detail). The resonance frequency of the Py nanodisks we obtained was higher than the resonance frequency for the Py film by round about 0.5 GHz at 100 mT. We suggest that the partially embedded nanodisks had different pinning conditions for SWs on the upper and lower surface. This modifies the SW mode profile as shown in Fig. 8.2. Thus we obtained a PSSW like excitation with a wave vector pointing out-of-plane increasing the resonance frequency of the nanodisks.

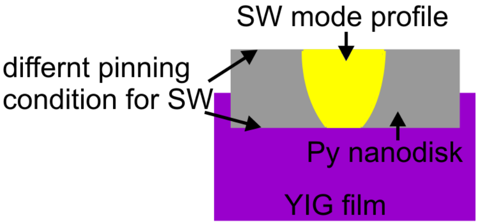

Figure 8.2: Modified SW mode profile due to different pinning conditions for SWs on the upper and lower surface of the Py nanodisk.

8.1.1 Short wavelength spin-wave generation

We evaluated the wavelength λ, propagation distance s_{eff} and the group velocity v_{g} of the SWs.
For the detection of short wavelength SWs over a large propagation distance the sample geometry in Fig. 4.3 (a) (MGC01) was favorable. The sample geometry consisted of two Py nanodisk arrays with a size of
365 x 15 $\mu\mathrm{m}^2$. A Py nanodisk array was located under each CPW. Between the CPWs Py nanodisks did not exist. This sample geometry was studied by H. Yu et al. [YdKC+16].

In Fig. 8.1 (b) and Fig. 8.3 (a) we present color-coded spectra ΔS_{11} and ΔS_{12}. Figure 8.1 (b) shows an angle scan measurement at an external magnetic field of 70 mT. In the angle scan measurement we observe various SW modes not resolved in the bare YIG film. 20 additional modes are present over a frequency range from 3 to 9 GHz. We assumed that the additional modes are MGC modes. The MGC modes were identified [Tab. 8.1] using the approach of Yu et al. [YDH+13].
In Fig. 8.3 (a) we show a field sweep measurement in MSSW configuration with $\theta = 0$ deg [Fig. 3.4 (a)]. We observed various propagating SWs attributed to MGC modes. MGC modes extracted from Fig. 8.3 that could be correlated to MGC modes in the angle scan measurement are listed in Tab. 8.2.
The emission angle δ of MGC modes is defined in Fig. 3.4 (a). SWs with emission angle $\delta = 0$ deg propagated along the CPW and SWs with $\delta = 90$ deg propagate perpendicular to the CPW. The effective propagation distance is calculated using $s_{\mathrm{eff}} = \frac{s}{sin(\delta)}$ and the experimental group

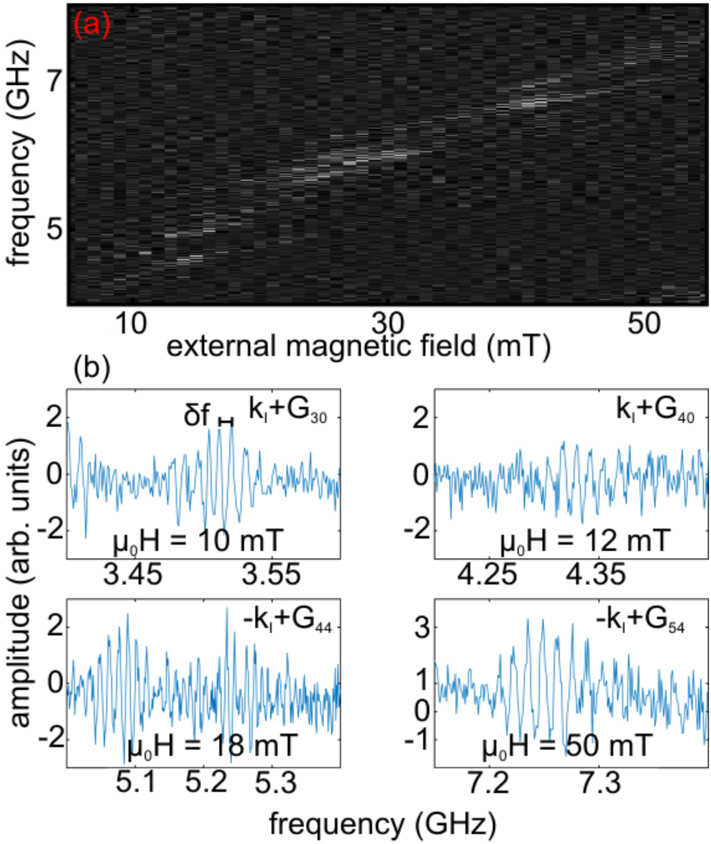

Figure 8.3: (a) Field sweep measurement with $\theta = 0$ deg. The measurement depicts the imaginary part of ΔS_{12} (white - positive values, black - negative values). (b) Line plots extracted from the measurement in (a) at different external magnetic fields and frequencies. The line plots are used to extract the group velocity $v_{\rm g}$. For the calculation of the line plots we applied method 1 in section 3.1.8. The microwave power amounted to -10 dBm.

$k_{\mathrm{I}} \pm G_{10}$	$k_{\mathrm{I}} \pm G_{01}$	$k_{\mathrm{I}} \pm G_{20}$	$k_{\mathrm{I}} \pm G_{02}$
$k_{\mathrm{I}} \pm G_{30}$	$k_{\mathrm{I}} \pm G_{11}$	$k_{\mathrm{I}} \pm G_{40}$	$k_{\mathrm{I}} \pm G_{22}$
$k_{\mathrm{I}} + G_{60}$	$k_{\mathrm{I}} + G_{16}$	$-k_{\mathrm{I}} + G_{54}$	$-k_{\mathrm{I}} + G_{44}$

Table 8.1: 20 different MGC modes extracted from Fig. 8.1 (b). We list MGC modes that were unambiguously identified from the angle scan measurement in Fig. 8.1 (b). Further MGC modes are not listed due to ambiguity.

velocity is calculated with $v_{\mathrm{g}} = \delta f \cdot s_{\mathrm{eff}}$ (Eq. 3.12) with δf extracted from Fig. 8.3 (b). For the calculation of theoretical values we used the same magnetic parameters as for the YIG thin film measurements in chapter 7. Data extracted from the spectra is listed in Tab. 8.2. Analyzing the extracted data we obtained SWs with a wavelength between 230 nm and 110 nm. The group velocities increased from 500 m/s to 1000 m/s with decreasing SW wavelength. The effective propagation distance was up to 86 μm. In Tab. 8.2 the experimental determined group velocity v_{g} deviates from the theoretical calculated group velocity v_{gt} [KS86] assuming the empty lattice model. In experiment we had nanodisks with finite dimension instead of an empty lattice. We suggest that the resulting band structure of the real sample is influenced by the form factor of the nanodisks. Because the group velocity correlates with the band structure, also the group velocity is influenced by the form factor of the nanodisks. The experiment substantiated the omnidirectional nature of the MGC mode [YDH$^+$13]. In Fig. 8.3 (a) we go beyond Ref. [YDH$^+$13] in that exchange dominated SWs were detected. In Ref. [YDH$^+$13] dipolar SWs were resolved.

8.1.2 Investigation of different sample geometries for magnonic grating-coupler

Up to now we analyzed the sample geometry depicted in Fig. 4.3 (a). In Fig. 8.4 we summarize spectra obtained for further sample geometries. All sample geometries consisted of a 200 nm YIG thin film combined with Py nanodisks [Fig. 8.4 (a) and (d)]. The arrangement and the size of the array varied (Tab. 4.1). For example the sample MGC01 consisted of 2 independent Py nanodisk arrays and the nanodisk array for the samples

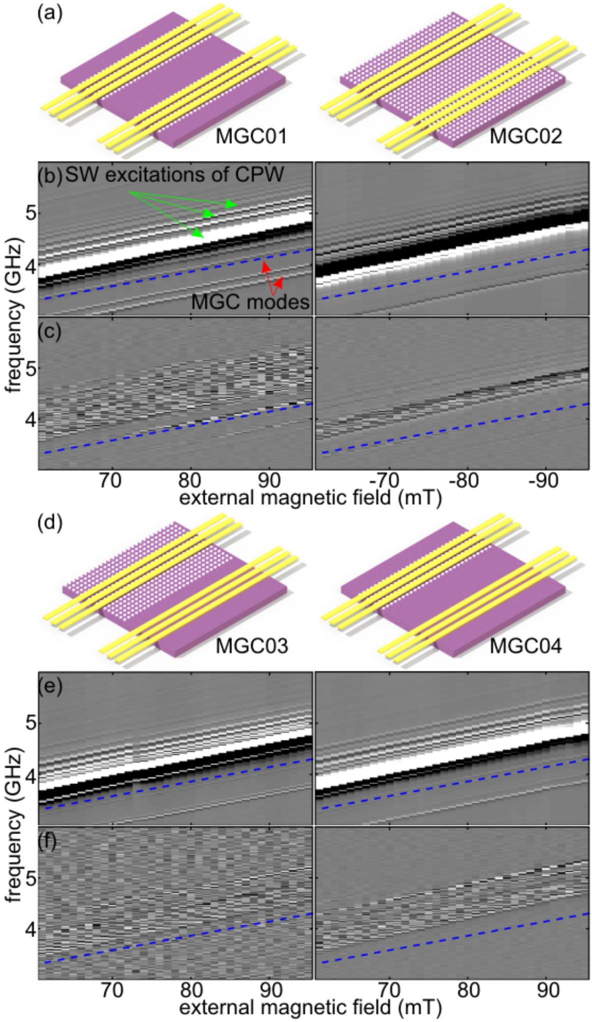

Figure 8.4: (a) Two sample geometries (MGC01 and MGC02) in which we detected SW propagation at MGC $k_\mathrm{I} + G_{12}$. (b) $\Delta\ S_{11}$ (linear magnitude) and (c) spectra $\Delta\ S_{21}$ (imaginary part) for MGC01 (left) and MGC02 (right). (d) Two samples (MGC03 and MGC04) did not show propagation at MGC $k_\mathrm{I} + G_{12}$. (e) $\Delta\ S_{11}$ (linear magnitude) and (f) spectra $\Delta\ S_{21}$ (imaginary part) for MGC03 (left) and MGC04 (right). The microwave power amounted to 0 dBm. The geometric parameters of the samples are summarized in Tab. 4.1.

MGC mode	λ [nm]	δ [deg]	s_{eff} [μm]	v_{g} [m/s]	v_{gt} [m/s]
$k_{\mathrm{I}} + G_{30}$	226	90	60	510 ± 30	431
$k_{\mathrm{I}} + G_{40}$	171	90	60	840 ± 60	630
$-k_{\mathrm{I}} + G_{44}$	125	44	86	988 ± 43	840
$-k_{\mathrm{I}} + G_{54}$	111	51	77	1046 ± 39	961

Table 8.2: MGC modes observed in angle scan and propagation measurement [Fig. 8.1 (b) and Fig. 8.3 (a)]. The table summarizes the SW wavelengths λ, experimentally and theoretically determined group velocities v_{g} and v_{gt}, respectively, the emission angle δ and the effective propagation distance s_{eff} of the SW. Theoretical values of the group velocity v_{gt} were obtained with the formalism of Kalinikos and Slavin [KS86].

MGC03 and MGC04 was located only underneath one CPW. For every sample geometry we present two data sets: The linear magnitude of $\Delta\ S_{11}$ [Fig. 8.4 (b) and (e)] and the imaginary part of $\Delta\ S_{21}$ [Fig. 8.4 (c) and (f)] in MSSW configuration ($\theta = 0$ deg). Because we identified the onset of non-linear behavior for small external magnetic fields, we analyzed the data above 60 mT. In all data sets we resolved signals from the k_{I} excitation and higher wave vectors excited by the CPW. The SW excitations highlighted by red arrows in Fig. 8.4 (b) originate from the MGC effect. The blue dashed line in the spectra represents the field dependent eigenfrequency of a SW with $k_{\mathrm{I}} + G_{12}$ using formalism of Ref. [KS86]. A corresponding resonance was resolved in $\Delta\ S_{11}$ for every sample [Fig. 8.4 (b) and (e)]. We note that we could not unambiguously identify the SW corresponding to $k_{\mathrm{I}} + G_{12}$ in Fig. 8.1 (b). Therefore the assignment was not finally possible. $\Delta\ S_{21}$ in Fig. 8.4 (c) contained a propagating SW mode attributed to $k_{\mathrm{I}} + G_{12}$. But in $\Delta\ S_{21}$ of Fig. 8.4 (f) we did not resolve the $k_{\mathrm{I}} + G_{12}$ MGC mode in propagation. We concluded that for ideal detection of MGC modes the detector of SWs had to consist of a CPW combined with the same Py nanodisk array as the emitter.

8.1.3 Discussion

MGC modes identified in BSWS measurements in Fig. 8.1 (b) are summarized in Fig. 8.5 in red color. MGC modes that are additionally resolved in a field sweep measurement ($\theta = 0$ deg) of ΔS_{12} [Fig. 8.3 (a)] are depicted in blue color in Fig. 8.5. MGC modes were resolved mainly along the high symmetry direction of 10 (01) and 11 in reciprocal space [Fig. 8.5]. A nanodisk magnetized in a distinct direction exhibits a south and a north pole. The north and a south pole act as source and drain for magnetic stray field, respectively. We suggest that source and drain of the magnetic stray field might act as two-component base for the SWs causing destructive interference for distinct reciprocal lattice vectors. Therefore distinct MGC modes were not resolved in experiment. Furthermore most propagating MGC modes were resolved along the 10 and 11 direction but none along the 01 direction. Along the 01 direction we got $\delta = 0$ and $s_{\mathrm{eff}} \to \infty$. The SWs did not reach the detector antenna, so we could not resolve MGC modes along 01 direction. The reciprocal lattice vectors highlighted in the green square in Fig. 8.5 were not unambiguously identified in propagation. SWs corresponding to the reciprocal lattice vectors $G_{10} = 9$ rad/μm and $G_{20} = 18$ rad/μm were in the same wave vector regime as SWs excited by the CPW [section 7.2]. SWs corresponding to the reciprocal lattice vectors G_{11} and G_{22} were in the same frequency regime for a field sweep measurement with $\theta = 0$ deg as SWs excited by the CPW. Thus we could not distinguish between SWs originating from a reciprocal lattice vector or of the CPW.

For sample MGC02 we present the measurements with opposite direction of the external magnetic field in Fig. 8.4, because the $k_{\mathrm{I}} + G_{12}$ MGC mode was only resolved for this magnetic field direction. Due to the nonreciprocity of the MGC mode obtained by the surface wave behavior in the YIG thin film this was not expected. Although the MGC mode $k_{\mathrm{I}} + G_{12}$ was not measured in MSSW configuration for H along $\theta = 0$ deg, we still assumed surface wave behavior for the MGC mode in this configuration. Because the periodicity of the Py nanodisks exceeds the thickness of the YIG film, we assumed that the SW on the surface without Py nanodisks could resolve the reciprocal lattice vectors of the Py nanodisk array. Thus the MGC mode $k_{\mathrm{I}} + G_{12}$ could exist on both sides of the YIG film. We suggest that the damping for propagating SWs was enhanced by the pres-

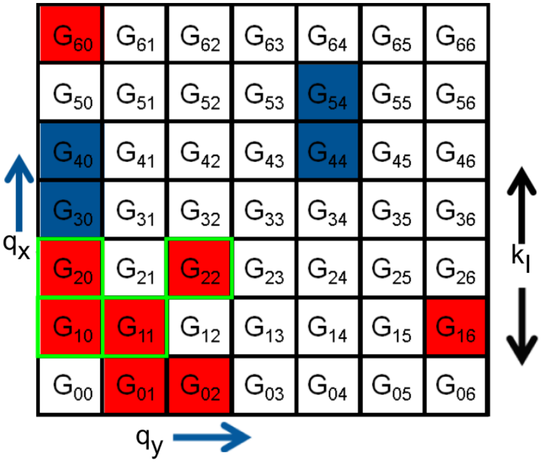

Figure 8.5: MGC modes observed in angle scan measurement [Fig. 8.1 (b)] and field sweep measurement [Fig. 8.3 (a)] plotted in reciprocal space. Every square denotes a Brillouin zone. The Brillouin zones are indicated with the corresponding reciprocal wave vector following Ref. [YDH$^+$13]. The k_I wave vector of the CPW was parallel to the axis of q_x. MGC modes unambiguously identified in the angle scan measurement [Fig. 8.1 (b)] are highlighted in red color. Further MGC modes are not highlighted due to ambiguity. MGC modes that are additionally resolved in propagation measurement [Fig. 8.3 (a)] are highlighted in blue color. The definition of the G_{00} reciprocal lattice vector is given in section 2.3.6.

ence of the Py nanodisks. Thus the SW on the side without Py nanodisks might be affected less by the Py nanodisks than the SW on the side with Py nanodisks, because of the surface wave behavior of the SW [Fig. 8.6]. Therefore the SW on the side of the YIG film without Py nanodisk was damped less and showed a larger decay length.

Most of the MGC modes resolved in propagation [Fig. 8.3 (a)] overlap with the resonance frequency of the Py nanodisks. If the MGC mode and the Py nanodisks had the same resonance frequency at a distinct external magnetic field the coupling of the electromagnetic wave of the CPW with the SW was enhanced by the dynamic susceptibility of the Py nanodisks. Therefore this SW is enhanced compared to the SW whose resonance frequency differed from the resonance frequency of the Py nano-

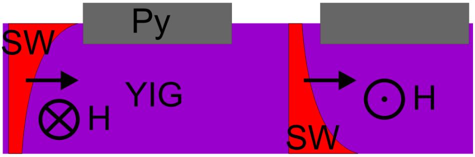

Figure 8.6: SWs with surface wave behavior (red color) are depicted propagating through the YIG film. Due to the nonreciprocity for opposing direction of H the SWs are affected differently by the Py nanodisks.

disks [YdKC$^+$16]. The reciprocal effect took place as well, i.e., the detection efficiency of grating coupler modes is enhanced compared to the bare CPW. Due to the reciprocal effect of the CPWs [SLCR99] it was important that the emitter and detector of SWs contained identical arrays.

8.2 Micro-focused Brillouin light scattering measurements on magnonic grating-coupler

The samples MGC01 and MGC03 [Fig. 4.3 (a) and (c)] were investigated with μBLS (section 3.2). The same CPWs excited the sample as in the section before, but the SWs were detected with a laser.

8.2.1 Magnonic grating-coupler modes in a large Permalloy nanodisk array

In this section micro-focused BLS data was obtained for sample MGC03 shown in Fig. 4.3 (c). We investigated an area of 1.4 x 5.0 μm^2 with a step width of 100 nm. SWs measured in Fig. 8.7 should behave as in an infinite MGC, because the lateral extension of the Py nanodisk array in propagation direction was 26 μm.

Figure 8.7 (a) shows BSWS spectra obtained on the corresponding CPW used for the μBLS measurements for MGC03. The red open circles denote the frequency and external magnetic field used for μBLS. The inset in Fig. 8.7 (a) shows the spatial resolved reflectivity scan of the investigated area. In Fig. 8.7 (b) bright areas indicated large spin precessional amplitudes excited at a frequency of 2.80 GHz at 35 mT. The excitation was not ho-

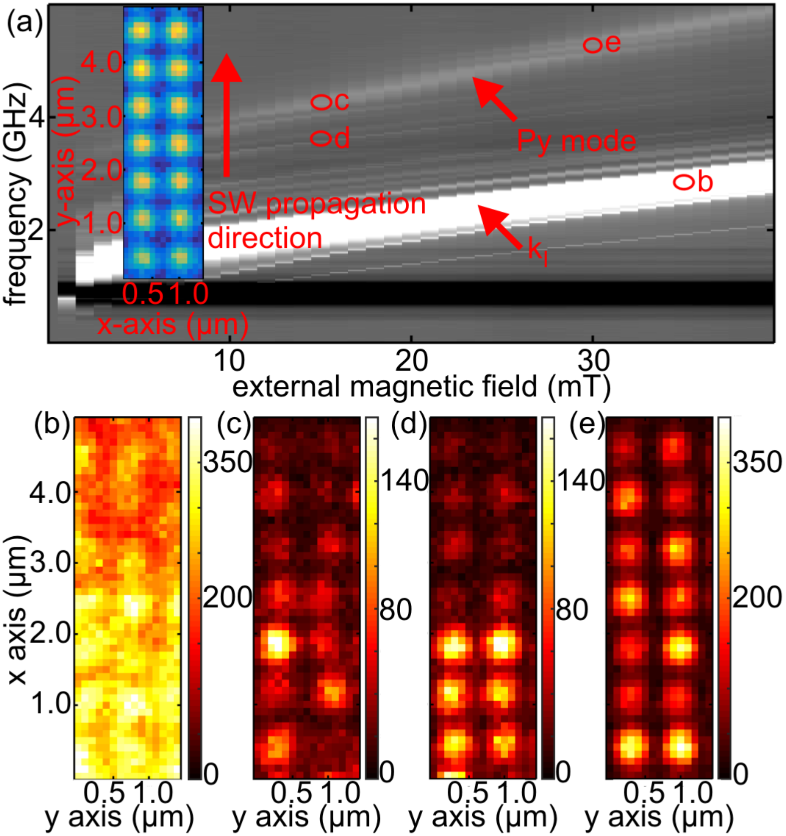

Figure 8.7: Linear magnitude of ΔS_{11} and μBLS obtained for sample MGC03 of Fig. 4.3 (c). SWs were excited by the CPW with the Py nanodisk lattice underneath. (a) ΔS_{11} spectrum with red open circles indicating the external magnetic field and excitation frequency used for μBLS (white - positive values, black - negative values). For the calculation of the spectra we applied method 1 in section 3.1.8. The inset shows the spatial resolved reflectivity scan of the investigated area. The external magnetic field was applied to the left hand side. The outer edge of the CPWs ground line is at the bottom of the investigated area. The following parameters were applied: (b) 35 mT and 2.80 GHz, (c) 15 mT and 4.20 GHz, (d) 15 mT and 3.65 GHz and (e) 30 mT and 5.30 GHz.

mogenous. We attributed this observation to the nanostructuring and the presence of the Py nanodisks. The SW intensity between the nanodisks was larger than at the position of the nanodisks. The SW mode was attributed to the k_I excitation of the CPW.

In Fig. 8.7 (c) a larger frequency was applied ($f = 4.20$ GHz at $\mu_0 H = 15$ mT). Here large signals were formed at the positions of the nanodisks. The signal strength varied from nanodisk to nanodisk. We attributed this observation to unintentional variations in the lateral dimension of nanodisks due to e.g. roughness. The roughness varied locally demagnetization factors and thereby the individual resonance frequencies of nanodisks. The variations in signal strength from nanodisk to nanodisk illustrated the inhomogeneous broadening of resonance frequencies in the nanodisk array.

In Fig. 8.7 (d) we applied an excitation frequency of 3.65 GHz at 15 mT. Signals were resolved at the position of the nanodisks. The signal strength at the position of the nanodisks between 0 to 2 μm along the x axis was larger compared to the signal strength above 2 μm. The large signals of the nanodisks between 0 to 2 μm were attributed to forced oscillation of the Py nanodisks by the CPW. In comparison the signal of the Py nanodisks above 2 μm was smaller, because Py nanodisks possessed a resonance frequency above 3.65 GHz for $\mu_0 H = 15$ mT. The SW mode investigated in Fig. 8.7 (d) corresponded to the wave vector $k_\mathrm{I} + G_{30}$.

In Fig. 8.7 (e) we applied an excitation frequency of 5.30 GHz at 30 mT. Signals were resolved at the position of the nanodisks. The signal strength was approximately constant over the whole Py nanodisk array. We suggest that in this measurement the Py nanodisk were excited at their resonance frequency at $\mu_0 H = 30$ mT. The SW mode investigated in Fig. 8.7 (e) corresponded to the wave vector $k_\mathrm{I} + G_{43}$. The assignment is not finally possible, because we could not identify this mode unambiguously in the angle scan measurement (not shown). Because the MGC mode exhibited the same resonance frequency as the Py nanodisks this SW mode was assigned as resonant MGC mode.

Interestingly in the measurements presented in Fig. 8.7 (d) and (e) we did not resolve signal from the SW modes at the position of the YIG film.

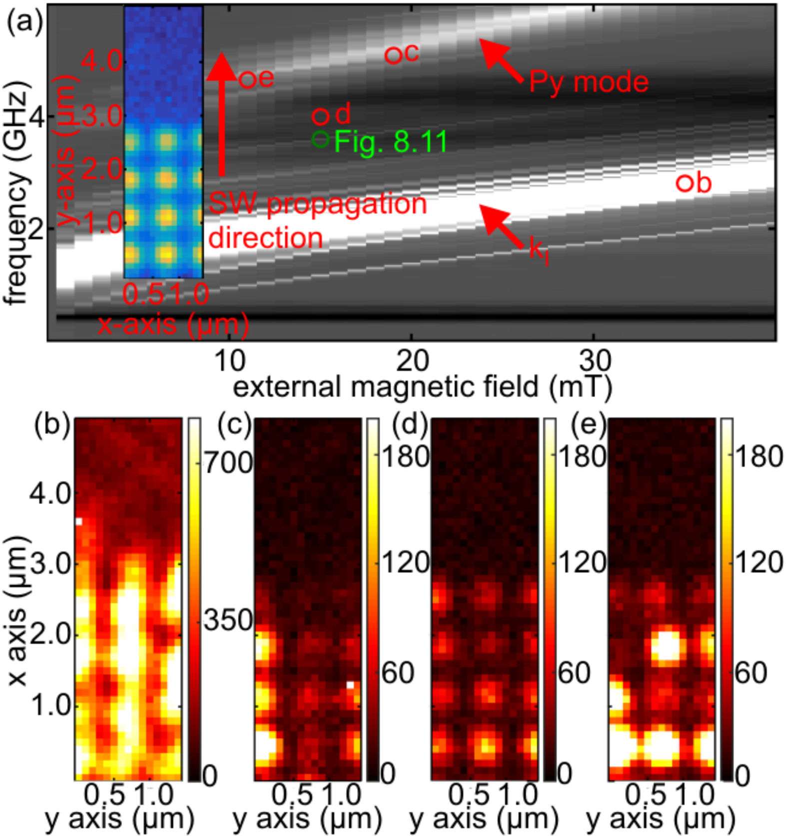

Figure 8.8: Linear magnitude of ΔS_{11} and μBLS obtained for sample MGC01 depicted in Fig. 4.3 (a). SWs were excited by the CPW with the Py nanodisk lattice underneath. (a) ΔS_{11} spectrum with red open circles indicating the external magnetic field and excitation frequency used for μBLS (white - positive values, black - negative values). For the calculation of the spectra we applied method 1 in section 3.1.8. The inset shows the spatial resolved reflectivity scan of the investigated area. The external magnetic field for the μBLS measurements was applied to the left hand side. The outer edge of the CPWs ground line is at the bottom of the investigated area. The following parameters were applied: (b) 35 mT and 2.80 GHz, (c) 19 mT and 5.09 GHz, (d) 15 mT and 4.00 GHz and (e) 11 mT and 4.65 GHz.

8.2.2 Magnonic grating-coupler modes in a limited Permalloy nanodisk array

In Fig. 8.8 we present μBLS data obtained for sample MGC01 [Fig. 4.3 (a)]. We investigated an area of 1.4 x 5.0 μm^2 with a step width of 100 nm. For this experiment the Py nanodisk did not cover the whole investigated area. The inset in Fig. 8.8 (a) shows the spatial resolved reflectivity scan of the investigated area. Figure 8.8 (a) shows a BSWS spectrum of the CPW used to excite sample MGC01. The red open circles denote frequencies and external magnetic fields used for μBLS measurements.
The resonance frequency of the Py nanodisks of MGC03 was 1.0 GHz lower at 100 mT as the resonance frequency of the Py nanodisks of MGC01. We suggest that this is provoked by two effects:

1. The saturation magnetization of the Py of MGC03 was smaller compared to the saturation magnetization of the Py of MGC01 used for the fabrication of the Py nanodisks [section 4.2.1].

2. The Py nanodisks of MGC03 did not show a modified SW mode profile as the Py nanodisks of MGC01 [section 8.1] and therefore a smaller resonance frequency.

In Fig. 8.8 (b) we applied a frequency of 2.80 GHz at 35 mT. Bright areas indicate large spin precessional amplitude. The excitation was not homogeneous. This was attributed to the nanostructuring and the presence of the Py nanodisks. The SW intensity is largest at the position of the nanodisk. The SW mode was attributed to the k_I excitation of the CPW.
For the measurement in Fig. 8.8 (c) a larger frequency was applied ($f = 5.09$ GHz at $\mu_0 H = 19$ mT). The signal strength varied from nanodisk to nanodisk. This was attributed to inhomogeneous broadening as for the measurement in Fig. 8.7 (c) in section 8.2.1. The SW mode was attributed to the resonance of the Py nanodisks.
In Fig. 8.8 (d) we applied 4.00 GHz and 15 mT. We resolved signals from the positions of the nanodisks and the signal strength decreased along the *x* axis. The SW mode investigated in Fig. 8.8 (d) corresponded to the wave vector $-k_\mathrm{I} + G_{40}$.
In Fig. 8.8 (e) we applied 4.65 GHz and 11 mT. We resolved signals from the positions of the nanodisks. But the signal strength at the position of the nanodisk varied. The SW mode investigated in Fig. 8.72 (d) corresponds

to the wave vector $k_{\mathrm{I}} + G_{43}$. The assignment was not finally possible, because we could not identify this mode unambiguously in the angle scan measurement [Fig. 8.1 (b)]. Because the MGC mode exhibited the same resonance frequency as the Py nanodisks this SW mode was assigned as resonant MGC mode.

Interestingly in the measurements in Fig. 8.8 (d) and (e) we did not resolve signal from the SW modes at the position of the YIG film.

In Fig. 8.8 (b) we resolved a standing wave pattern above the Py nanodisk lattice. To investigate this behavior in more detail we conducted further measurements for the nominally identical area at the same external magnetic field (35 mT). But this time we swept the excitation frequency from 2.7 GHz to 3.0 GHz in steps of 0.1 GHz. For comparison we show the same measurement for a bare YIG film excited with the same CPW.

For the bare YIG film [Fig. 8.9, Fig. 8.10 upper row] using the excitation frequency of 2.7 GHz we obtained an exponentially decaying SW attributed to the k_{I} excitation. But by increasing the excitation frequency we resolved a standing wave pattern for 2.8 and 2.9 GHz. This standing wave pattern occurred due to an anticrossing of the PSSW of first order ($p = 1$) and the k_{I} excitation as already discussed in chapter 7. At 3.0 GHz the SW intensity goes to zero. For the sample MGC01 [Fig. 8.9, Fig. 8.10 lower row] we obtained a similar results as for the bare YIG film but the distribution of the SW intensity was superimposed by the presence of the Py nanodisks and their stray field. Therefore we concluded that for the nominally identical measurement of Fig. 8.8 (b) in Fig. 8.9 (f) the standing wave pattern originated from the anticrossing of the PSSW of first order ($p = 1$) and the k_{I} excitation. In Fig. 8.9 (f) and Fig. 8.10 (f) we find large spin precession amplitude in parallel stripes underneath and between the nanodisks, respectively. This observation is already investigated and discussed in Ref. [DMN^{+}11].

8.2.3 Magnonic grating-coupler modes at a spin-wave interface

Figure 8.11 (a) shows μBLS data of MGC01 for parameter marked in Fig. 8.8 (a) with a green open circle. The data of the particular MGC mode shown in Fig. 8.11 (a) started at the nominally identical spatial point as the other μBLS measurement of MGC01 but the investigated area was enlarged (2.8 x 10.0 μm^2). Therefore we provided a spatial resolved re-

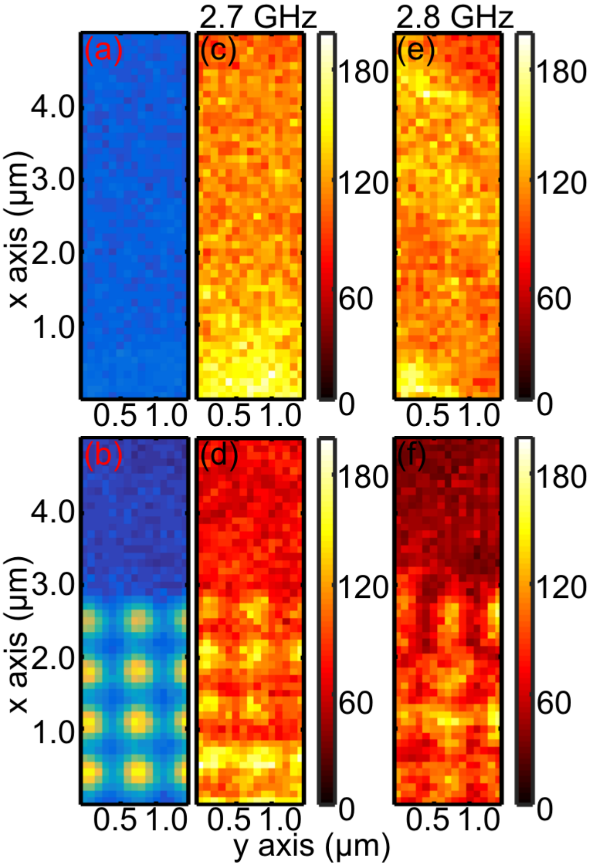

Figure 8.9: (a) and (b) Spatial resolved reflectivity scan of the investigated area for the bare YIG film and MGC01. The external magnetic field (35 mT) for the μBLS measurements was applied to the left hand side. The outer edge of the CPWs ground line is at the bottom of the investigated area. The following excitation frequencies were applied: (c),(d) 2.7 GHz, (e),(f) 2.8 GHz.

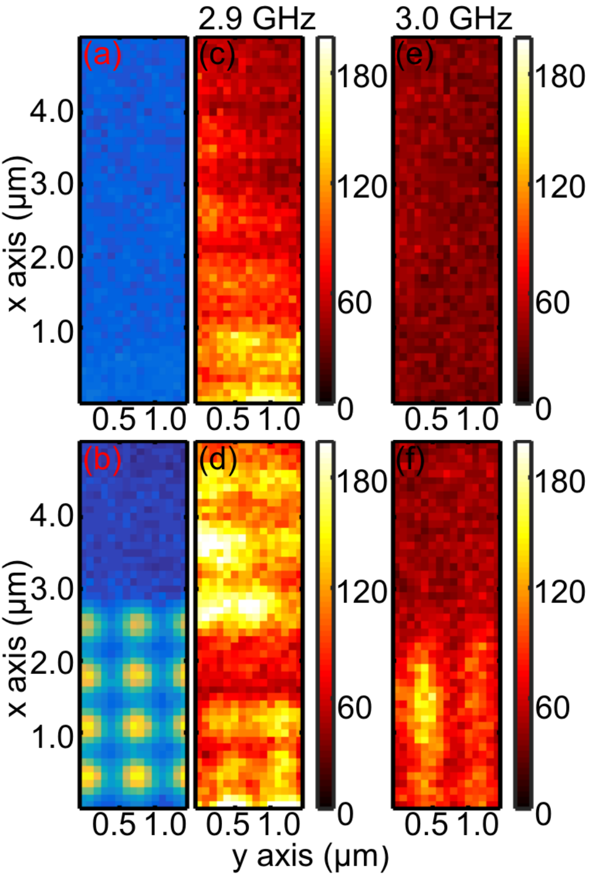

Figure 8.10: (a) and (b) Spatial resolved reflectivity scan of the investigated area for the bare YIG film and MGC01. The external magnetic field (35 mT) for the μBLS measurements was applied to the left hand side. The outer edge of the CPWs ground line is at the bottom of the investigated area. The following excitation frequencies were applied: (c),(d) 2.9 GHz, (e),(f) 3.0 GHz.

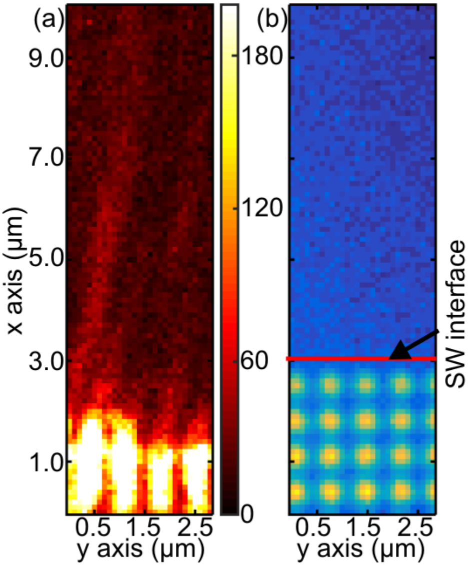

Figure 8.11: (a) μBLS data obtained with the same CPW as the BSWS spectrum shown in Fig. 8.8 (a). The excitation frequency was 3.60 GHz and the applied external magnetic field was 15 mT. (b) Spatial resolved reflectivity scan of the investigated area.

flectivity scan of the investigated area [Fig. 8.11 (b)]. The step width is again 100 nm. In this experiment we resolved signal from the YIG film. The SWs formed channels in the YIG film above the Py nanodisk array and were observed up to a distance of 7.0 μm to the CPW. We attributed the SW signal to a standing wave pattern formed by two MGC modes. At $\mu_0 H = 15$ mT applied along $\theta = 0$ deg the calculated eigenfrequency of $k_{\mathrm{I}} + G_{30}$ and $k_{\mathrm{I}} + G_{31}$ differs by only 30 MHz. We suggest that in Fig. 8.11 (a) both modes are excited by the CPW and form the standing wave pattern. The data further showed that MGC modes are not suppressed at a SW interface [definition of SW interface see section 2.4.3].

8.2.4 Discussion

In μBLS measurements we observed different properties for MGC modes and resonant MGC modes. The microscopic reason for the different properties was the resonance frequency and dynamic susceptibility of the Py nanodisks.

Magnonic grating-coupler mode

MGC modes exhibited resonance frequencies different to the resonance frequency of the Py nanodisks at a distinct external magnetic field. If the MGC mode was excited, the Py nanodisks were excited off-resonant and we suggest their dynamic magnetic susceptibility is small. In Fig. 8.7 (d) we resolved a small precession amplitude above 2 μm of the magnetic moments of the Py nanodisks. We suggest that by the small precession amplitude the MGC mode is not influenced.

Resonant magnonic grating-coupler mode

Resonant MGC modes exhibited resonance frequencies similar to the resonance frequency of the Py nanodisks at a distinct external magnetic field. If a resonant MGC mode was excited, the Py nanodisks were excited resonant and we suggest their dynamic magnetic susceptibility was large. In Fig. 8.7 (e) we resolved a large precession amplitude of the magnetic moments of the Py nanodisk. We suggest that by the large precession amplitude the MGC mode is enhanced. The enhancement of the MGC mode by the stray field of the nanodisk array is described in Ref. [YdKC^{+}16]. But in contrast to Ref. [YdKC^{+}16] we have observed this effect on the microscale.

8.2.5 Conclusion

In this chapter we have shown that by adding an array of magnetic nanodisks to a ferrimagnetic thin film we created MGC modes in the dipole-exchange regime. The MGC modes showed a wavelength down to 110 nm and group velocity up to 1 km/s. The SWs were detected over a distance of up to 86 μm. We point out that the group velocity increased with decreasing SW wavelength in the exchange regime. This is crucial for creating SWs that combine large group velocity and small SW wavelength. We further showed that the detection efficiency of the CPW was enhanced for MGC modes if the exciting CPW and the detecting CPW had the same emission characteristic.

In μBLS measurements we elaborated that MGC modes and resonant MGC modes showed different characteristics on the microscale. This is caused by the dynamic susceptibility of the Py nanodisk. The resonant MGC mode was enhanced compared to the MGC mode. The μBLS measurements revealed that MGC modes were not suppressed at SW interfaces.

9 Investigation of columnar crystal lattice distortions in a 200 nm thick yttrium iron garnet film produced with helium ion microscopy

In this chapter the nominal identical 200 nm thick YIG film presented in chapter 7 was exploited by a 40 μm long CPW. We investigated the samples as for the bare YIG film in chapter 7 and of the MGC effect in chapter 8. The experiments were based on the setup in chapter 3.1. To know about the excitation spectrum of the short CPW we present spectra obtained for a bare YIG film with the 40 μm long CPW, before we investigated different lattices fabricated with HIM. We show a different type of MGC not investigated so far in literature to the best knowledge of the author. We discuss absorption data, namely the linear magnitude of ΔS_{11}. We also discuss propagation data as ΔS_{12}. The microwave power amounted to -20 dBm and the external magnetic field was applied in the sample plane. If not stated differently we show ΔS_{11} spectra.

The sample consisted of a YIG thin film with a thickness $t = 200$ nm with CLDs arranged in a periodic lattice using HIM (chapter 3.3). Both sample fabrication and geometric parameters are given in section 4.3. The geometric parameters and the excitation amplitudes of the CPW are given in section 3.1.5. For the CPW ($w = 2.1$ μm) a maximum excitation amplitude occurs at $k_\mathrm{I} = 0.9$ rad/μm.

9.1 Broadband spin-wave spectroscopy on yttrium iron garnet film using a 40 micrometer long coplanar waveguide

In this section we investigate the spectrum of sample H00 consisting of a bare 200 nm thick YIG film excited with a 40 μm long CPW. In Fig 9.1 (a) and (b) we show spectra of two field sweep measurements with $\theta = 0$ deg and $\theta = 90$ deg, respectively. The blue (red) line in Fig. 9.1

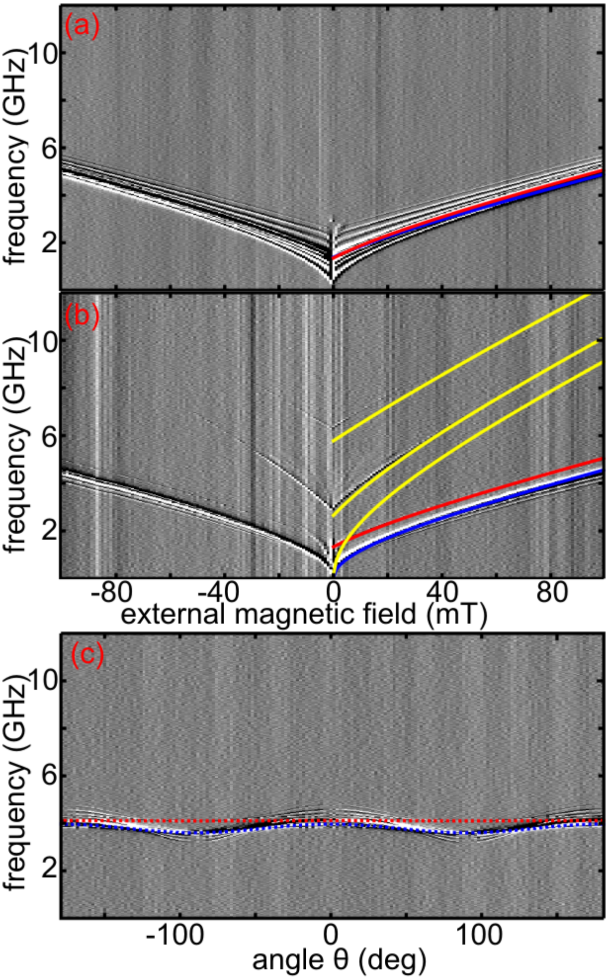

Figure 9.1: Spectra obtained for sample H00 with the short CPW (40 μm) prepared on a bare YIG thin film (white - positive values, black - negative values). The blue and red lines were calculated following Ref. [KS86] and corresponded to the fundamental SW ($p = 0$) and the PSSW mode of first order ($p = 1$), respectively. With the yellow lines we modeled mode branches induced by parallel parametric pumping following Eq. 2.41. (a) Field sweep measurement with $\theta = 0$ deg. (b) Field sweep measurement with $\theta = 90$ deg. (c) Angle scan measurement with an external magnetic field of 70 mT. We intentionally have chosen the y scale from 1 to 11 GHz. This is instructively for the following sections.

denote the eigenfrequency for the k_{I} excitation (PSSW mode) calculated with Ref. [KS86] using the same parameter as in chapter 7. The resonances fitted with the yellow lines were attributed to parallel parametric pumping. For the calculation of the yellow lines we applied Eq. 2.41 based on the formalism of Ref. [KS86]. We show the calculation for parallel parametric pumping for the fundamental spin wave mode ($p = 0$), for the PSSW mode of first ($p = 1$) and second ($p = 2$) order.

9.2 Investigation of a 200 nm thick YIG film with periodic arranged columnar crystal lattice distortions

Now we discuss sample H01 fabricated with the periodicities $a_{\mathrm{x}} = 100$ nm and $a_{\mathrm{y}} = 400$ nm [Fig. 4.5 (a)]. We performed field sweep measurements with $\theta = 0$ deg [Fig. 9.2 (a)] and $\theta = 90$ deg [Fig. 9.2 (b)] and an angle scan measurement at an external magnetic field of 70 mT [Fig. 9.3 (a)]. A series of SW modes were resolved in Fig. 9.2 and Fig. 9.3 that were not resolved in the bare YIG film using the nominally identical CPW. In Fig. 9.2 (a) we obtained SW modes below and above the k_{I} excitation for $\theta = 0$ deg. The field sweep measurement was obtained from -100 mT to 100 mT. The SW modes for an external magnetic field $\mu_0 H$<-45 mT and $\mu_0 H$>50 mT could be described by the formalism of Ref. [KS86] (see below). But for -45 mT< $\mu_0 H$ <50 mT the evolution of the SW modes changed. We suggest that SW resonances were modified due to hard axis behavior induced by nanostructuring with the HIM. We omitted theoretical calculations for this magnetic field regime, because we did not know the state of the magnetization.
The main mode highlighted by orange arrows in the spectra of Fig. 9.2 and 9.3 was attributed to the plain film resonance. We intentionally prepared a CPW probing the nanostructured sample and the bare film. Therefore we obtained the k_{I} excitation as reference in all spectra in this chapter.

In the spectra of the angle scan measurement we obtained a mode with minima at 0 and 90 (-90) deg highlighted by blue arrows in Fig. 9.3 (a). For an external magnetic field pointing along $\theta = 0$ deg direction (along the y axis) we obtained a resonance frequency below the k_{I} excitation [blue arrows in Fig. 9.2 (a)]. For an external magnetic field pointing along $\theta = 90$ deg direction (along the x axis) we obtained resonance frequency in

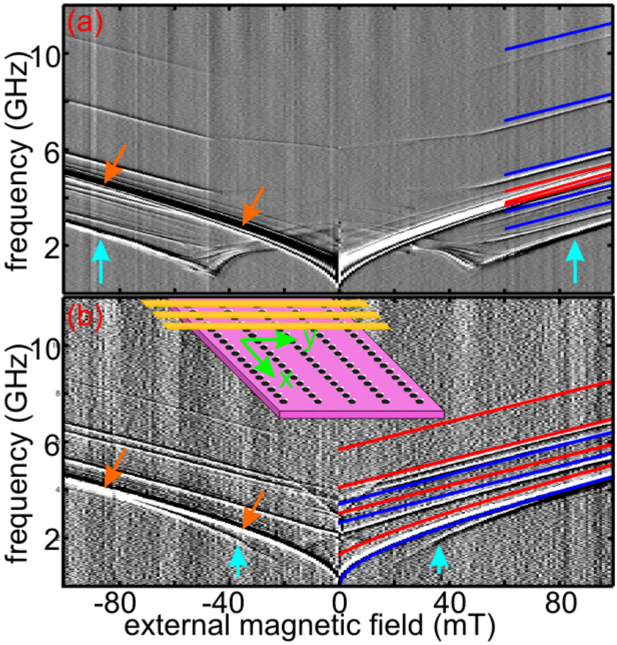

Figure 9.2: Spectra obtained for sample H01 prepared with the HIM. The periodicities amounted to $a_\mathrm{x} = 100$ nm and $a_\mathrm{y} = 400$ nm (white - positive values, black - negative values). The blue and red lines are calculated following Ref. [KS86] with corresponding reciprocal lattice vectors. The blue lines corresponded to the fundamental SW ($p = 0$) and the red lines corresponded to the PSSW mode of first order ($p = 1$) respectively. (a) Field sweep measurement with $\theta = 0$ deg. (b) Field sweep measurement with $\theta = 90$ deg. The inset shows a sketch of the sample and indicates the lattice symmetry of the CLDs compared to the CPW.

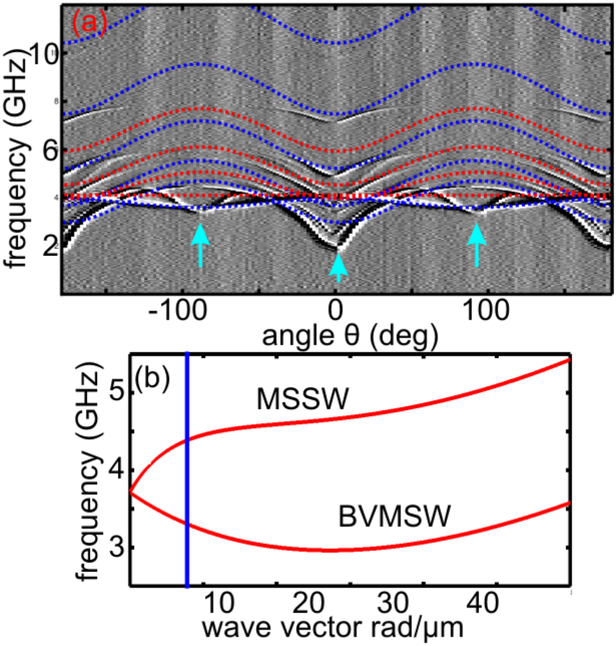

Figure 9.3: Spectra obtained for sample H01 prepared with the HIM. The periodicities amounted to $a_{\mathrm{x}} = 100$ nm and $a_{\mathrm{y}} = 400$ nm (white - positive values, black - negative values). The blue and red lines were calculated following Ref. [KS86] with corresponding reciprocal lattice vectors. The blue lines corresponded to the fundamental SW ($p = 0$) and the red lines corresponded to the PSSW mode of first order ($p = 1$) respectively. (a) Angle scan measurement with an external magnetic field of 70 mT. (b) Calculated dispersion relation with an external magnetic field of 70 mT applied in MSSW and BVMSW configuration following Ref. [KS86].

$\mathbf{k}$ (p = 0)	λ (nm)	$\mathbf{k}$ (p = 1)	λ (nm)	γ (deg)
$\mathbf{k}_\mathrm{I} + G_{01}$	399	$\mathbf{k}_\mathrm{I} + \boldsymbol{\kappa}_\mathrm{p} + \mathbf{G}_{01}$	283	45
$\mathbf{k}_\mathrm{I} + \mathbf{G}_{02}$	200	$\mathbf{k}_\mathrm{I} + \boldsymbol{\kappa}_\mathrm{p} + \mathbf{G}_{02}$	179	27
$\mathbf{k}_\mathrm{I} + \mathbf{G}_{03}$	133	$\mathbf{k}_\mathrm{I} + \boldsymbol{\kappa}_\mathrm{p} + \mathbf{G}_{03}$	127	18
$\mathbf{k}_\mathrm{I} + \mathbf{G}_{04}$	100			
$\mathbf{k}_\mathrm{I} + \mathbf{G}_{05}$	80			

Table 9.1: Wave vectors of MGC modes evaluated from the spectra of sample H01. The wavelength was calculated with $\lambda = 2\pi/k$. The angle γ denotes the out-of-plane orientation of the wave vector. The definition of γ is given in Fig. 2.3

the same frequency range as the k_I excitation [blue arrows in Fig. 9.2 (b)]. This mode was attributed to confined SWs. In Fig. 9.3 (b) we calculated the SW dispersion relation for MSSW and BVMSW configuration. We assumed that the wave vector of the SW was confined along the *y* axis. We suggest a wave vector of $k = 2\pi/(2a_\mathrm{y}) = 8$ rad/μm for the confined SW [blue line in Fig. 9.3 (b)]. For an external magnetic field pointing along $\theta = 0$ deg direction (along the *y* axis) the confined SW is in BVMSW configuration. The SW frequency decreased with increasing wave vector [Fig. 9.3 (b)] and as a result the resonance frequency was below the frequency of the k_I excitation. For an external magnetic field pointing along $\theta = 90(-90)$ deg direction (along the *x* axis) we obtained MSSW configuration for the confined SW. Therefore the resonance frequency increased with increasing wave vector and as a result the resonance frequency was in the same frequency range as the k_I excitation. This became apparent in the angle scan for $\theta = 90(-90)$ deg in Fig. 9.3 (a). However the local minimum of the confined SW around $\theta = 90(-90)$ deg was not expected. We suggest that the CLDs modified the internal field so that the SW resonance was decreased. We point out that the angle scan measurement was performed near the anisotropy field induced by hard axis behavior of the sample. This might have influenced the experimental result of the angle scan measurement.

Now we compare the experimental data to theoretical data using the formalism of Ref. [KS86] and the magnetic parameters used in chapter 7.

$\mathbf{k}\ p = 0$	λ (nm)	$\mathbf{k}\ p = 1$	λ (nm)	γ (deg)
$\mathbf{k}_\mathrm{I} + \mathbf{G}_{10}$	378	$\mathbf{k}_\mathrm{I} + \boldsymbol{\kappa}_\mathrm{p} + \mathbf{G}_{10}$	275	43
$\mathbf{k}_\mathrm{I} + \mathbf{G}_{20}$	194	$\mathbf{k}_\mathrm{I} + \boldsymbol{\kappa}_\mathrm{p} + \mathbf{G}_{20}$	175	26
$\mathbf{k}_\mathrm{I} + \mathbf{G}_{30}$	131	$\mathbf{k}_\mathrm{I} + \boldsymbol{\kappa}_\mathrm{p} + \mathbf{G}_{30}$	124	18

Table 9.2: Wave vectors of MGC modes evaluated from the spectra of sample H02. The wavelength was calculated with $\lambda = 2\pi/k$. The angle γ denotes the out-of-plane orientation of the wave vector. The definition of γ is given in Fig. 2.3

For the blue lines we assumed a fundamental SW with $p = 0$ approaching the dipole-exchange regime due to the reciprocal lattice vectors originating from the CLDs. For the red lines we used the same approach, but instead of the fundamental SW ($p = 0$) we assumed a PSSW mode of first order ($p = 1$) with the additional wave vector contribution $\kappa_\mathrm{p} = p\pi/t$. The wave vector κ_p points out-of-plane. The wave vectors of the resolved MGC modes are listed in Tab. 9.1. The corresponding wavelengths range from 400 nm to 80 nm. In Tab. 9.1 we calculated the out-of-plane orientation γ of the wave vector provoked by the out-of-plane component κ_p. Using the combined mode nature of fundamental SW ($p = 0$) and PSSW ($p = 1$) we obtained theoretical data that shows reasonable agreement with the SW resonances found in experiment.

For further studies we fabricated a nominal identical sample [H02 in Fig. 4.5 (b)] with the lattice rotated by 90 deg so that $a_\mathrm{x} = 400$ nm and $a_\mathrm{y} = 100$ nm. Sample H02 was measured with the same orientation of CPW and external magnetic field as sample H01. For this sample we observed a partly similar set of modes. Experimental data is fitted with the same approach [blue and red lines in Fig. 9.4] as the sample H01. The evaluated wave vectors of MGC modes and the out-of-plane orientations γ of the wave vector are listed in Tab. 9.2.

Now we compare the observed MGC modes of H02 to the ones of H01. For H01 [Tab. 9.1] we observed MGC modes with the reciprocal lattice vectors G_{0i} with $i = 1,2,...$ whereas for H02 [Tab. 9.2] we observed MGC modes with the reciprocal lattice vectors $G_{\mathrm{i}0}$. By rotating the lattice of H02 by 90 deg also the orientation of the reciprocal lattice vectors rotated. Therefore we concluded that the MGC modes observed in H01 and H02

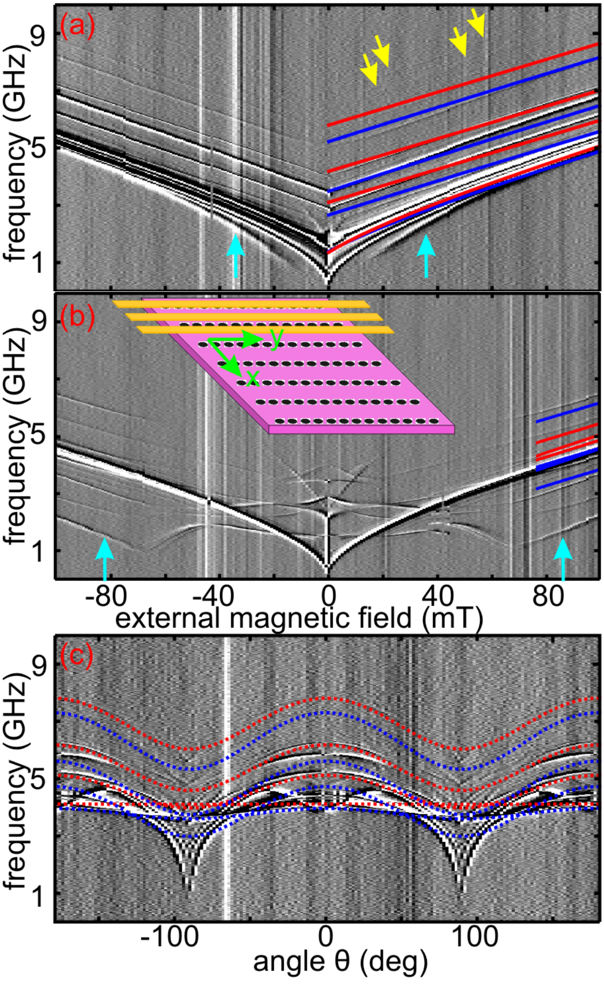

Figure 9.4: Spectra obtained for sample H02 prepared with the HIM. The periodicities amounted to $a_\mathrm{x} = 400$ nm and $a_\mathrm{y} = 100$ nm (white - positive values, black - negative values). The blue and red lines were calculated following Ref. [KS86] with corresponding reciprocal lattice vectors. The blue lines corresponded to the fundamental SW ($p = 0$) and the red lines corresponded to the PSSW mode of first order ($p = 1$) respectively. (a) Field sweep measurement with $\theta = 0$ deg. (b) Field sweep measurement with $\theta = 90$ deg. The inset shows a sketch of the sample and indicates the lattice symmetry of the CLDs compared to the CPW. (c) Angle scan measurement with an external magnetic field of 70 mT.

are of geometrical origin and created via the arrays of HIM induced CLDs. Similar to H01 we observed confined SWs in H02 [indicated by blue arrows in Fig. 9.4]. The confined SWs with low resonance frequency were observed for $\theta = 90(-90)$ deg. The confined SWs with high resonance frequency appeared for $\theta = 0$ deg. The occurrence of the confined SWs in H02 was rotated by 90 deg compared to H01. Furthermore the confined SWs for H01 had a minimum frequency of around 2 GHz at 70 mT in the angle scan measurement. For H02 the confined SWs showed a minimum frequency of 1 GHz in the angle scan measurement at 70 mT. As mentioned in chapter 4.3, we deposited aluminum on top of the YIG film. We suggest that the aluminum layers for H01 and H02 had a different morphology. Thus the interaction of the helium ions with the sample might vary. In consequence parameters as the penetration depth and scattering length of the helium ions in the YIG film might be different. We suggest that the YIG film was modified differently by the punctual penetration of the helium ions in the case of the samples H01 and H02.

For sample H02 two further SW modes highlighted by yellow arrows in Fig. 9.4 (a) were observed. We suggest that this modes originated from the reciprocal lattice vectors G_{01} and G_{11} with $p = 1$. These wave vectors were associated with the periodicity of 100 nm. But we did not resolve these modes in the angle scan measurement. Therefore we could not identify these modes unambiguously.

The third sample of this type (H03) in Fig. 9.5 was fabricated with similar parameter for the HIM and the same geometric dimensions as H02. Additionally H03 was measured simultaneously to H02. Nevertheless if we compared of H02 and H03 in detail we observed differences. The mode of H03 highlighted by green arrows in Fig. 9.5 (a) was shifted by 200 MHz to a larger frequency compared to H02. If we used the same approach as for H02 to fit the data in H03 we could not obtain a reasonable agreement (not shown). To obtain the result in Fig. 9.5 we had to vary the magnetic parameter that were used to fit the experimental data. For M_{S} we used 135 kA/m and for $\gamma/2\pi$ we used 29.5 GHz/T. With these magnetic parameter we obtained a reasonable agreement for H03 [Fig. 9.5]. From literature we extracted that helium irradiation influences the morphology of materials [HNS12]. We suggest that due to the nanostructuring with the HIM the crystal structure of the YIG film was modified by the helium ions and therefore the magnetic parameters varied. But as already stated we used the similar parameters for sample H02 and H03. Still it might

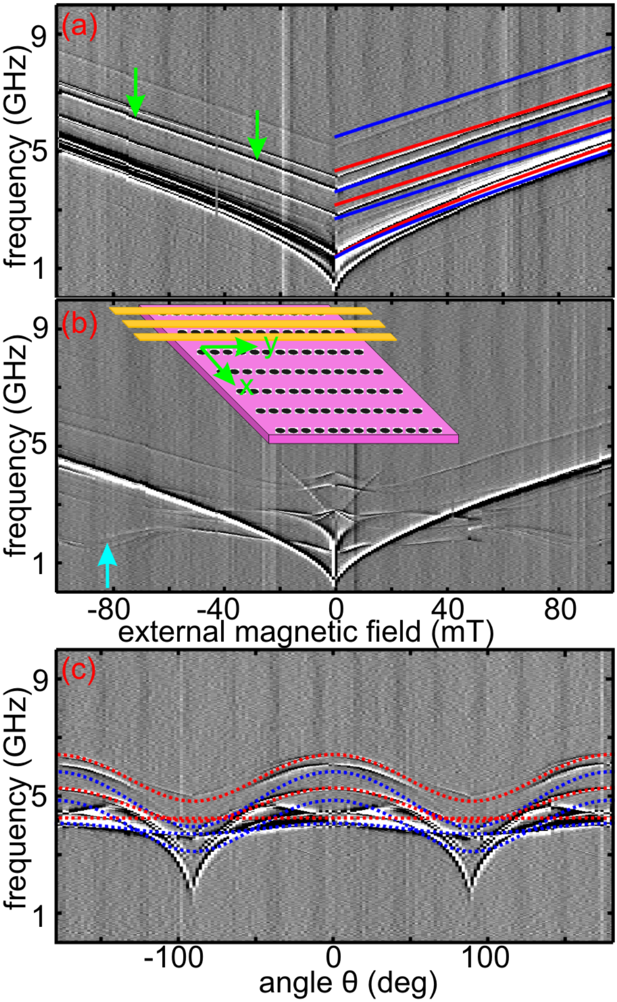

Figure 9.5: Spectra obtained for sample H03 prepared with the HIM. The periodicities amount to $a_\mathrm{x} = 400$ nm and $a_\mathrm{y} = 100$ nm (white - positive values, black - negative values). The blue and red lines are calculated following Ref. [KS86] with corresponding reciprocal lattice vectors. The blue lines corresponded to the fundamental SW ($p = 0$) and the red lines corresponded to the PSSW mode of first order ($p = 1$) respectively. (a) Field sweep measurement with $\theta = 0$ deg. (b) Field sweep measurement with $\theta = 90$ deg. The inset shows a sketch of the sample and indicates the lattice symmetry of the CLDs compared to the CPW. (c) Angle scan measurement with an external magnetic field of 70 mT.

be possible that during fabrication sample H03 was irradiated by a larger overall dose as H02. This could happen for example by taking a different number of pictures with the HIM.

9.3 Spin-wave propagation in periodic arranged columnar crystal lattice distortions

We investigated the propagation characteristics of SWs excited using the sample geometries depicted in Fig. 4.6. For the sample geometry depicted in Fig. 4.6 (a) the propagation signal between the bare YIG film of sample H00 (CPW1) and the magnonic lattice of sample H01 (CPW2) is measured. We show the spectra ΔS_{12} in Fig. 9.6 (a). In the spectra we observed the k_{I} excitation. Because the lattice was fabricated only underneath CPW2 [Fig. 4.6 (a)], the emission and detection characteristics of the two CPWs were different. But for ideal detection of MGC modes the CPWs should have the same characteristics as already discussed in chapter 8. For the next experiment we investigated the sample geometry in Fig. 4.6 (b). The propagation signal measured between the magnonic lattices of sample H02 and H03 is depicted in Fig. 9.6 (b). We show spectra of ΔS_{12}. We observed the k_{I} excitation. For this experiment we expected propagation signal of the MGC modes because underneath both CPWs periodic arranged CLDs were prepared. But we did not resolve any propagation signal of MGC modes in experiment. We had shown that the two lattices of H02 and H03 did not exhibit the same SW resonance frequencies (section 9.2). In consequence the emission and detection characteristic of the two CPWs were different. But for ideal detection of MGC modes in propagation measurement the CPWs should have the same the emission and detection characteristics as already discussed in chapter 8.

In Fig. 9.7 we simulated the displacement of the atoms in the YIG film by the helium ions penetrating the sample using the software SRIM [ZZB08]. The simulated sample consisted of 10 nm Al, 200 nm YIG and, 500 nm GGG. The material parameters used for simulation are listed in Tab. 9.3 as extracted from Ref. [HD94, GG58, LSP^{+}12]. The simulation in Fig. 9.7 revealed that the helium ion beam of the HIM produces a major change in the underlying YIG thin film. Therefore we suggest that due to the helium ion beam the crystal structure of the YIG thin film is locally distorted and helium ions were implemented. This might increase the damping of the

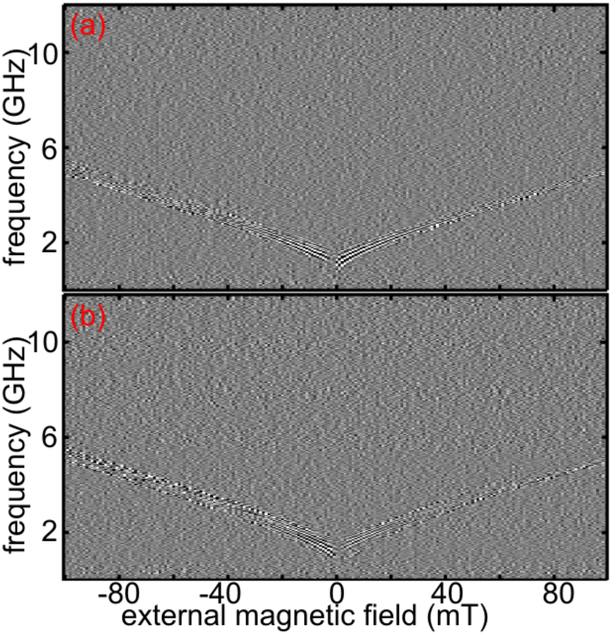

Figure 9.6: Imaginary part of ΔS_{12} obtained for the YIG thin film samples nanostructured with the HIM. The measurements were performed in MSSW configuration. (a) ΔS_{12} obtained for sample geometry in Fig. 4.6 (a). (b) ΔS_{12} obtained for sample geometry in Fig. 4.6 (b)

YIG film and thus the propagation of MGC modes was further suppressed. For both sample geometries we suggest that the resolved propagation signal of the k_I excitation originated from the bare YIG film. As shown in Fig. 4.6 the CPW was partially or completely located on a bare YIG film for all samples H00-H03.

9.4 Discussion

The spectra of samples H01 to H02 revealed that we resolved MGC modes originating mainly from reciprocal lattice vectors along one distinct direction of the lattice. For H01 we observed MGC modes corresponding to

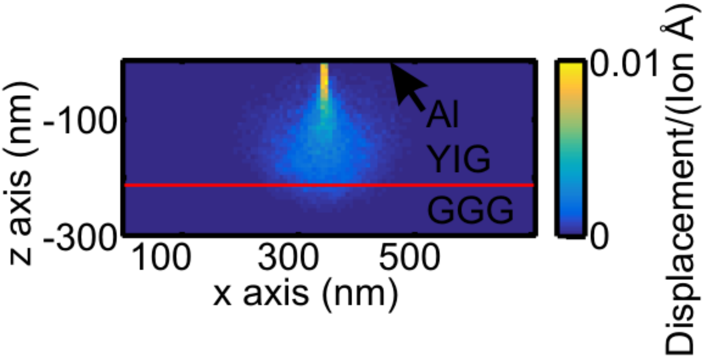

Figure 9.7: Simulated displacement of the atoms in the YIG film by helium ions penetrating the sample composed of 10 nm Al, 200 nm YIG and, 500 nm GGG using the software SRIM2013 [ZZB08]. We simulated 6000 helium ions penetrating the sample. We assumed a accleration voltage of 30 keV. The red line depicts the boundary between the YIG and the GGG. The position of the Al layer on top of the sample is indicated by a black arrow. The parameters of Tab. 9.3 were used.

G_{0i} with i = 1,2,... and for H02 MGC modes corresponding to $G_{\mathrm{i}0}$. The corresponding reciprocal lattice vectors were associated with the periodicity of 400 nm. We suggest that this effect was due to the depth profile of the helium ions used to nanostructure the sample. In Fig. 9.7 the simulated displacement is bell-shaped. The maximum width of this bell exceeds 100 nm, what was the lattice constant of the array in one direction. Therefore we concluded that underneath the surface the bell-shaped profiles connected and formed a line of modified YIG. Still we saw separate points in the HIM microscope picture on the sample surface [Fig. 4.5 (a)

material	density [g/cm^3]
Al	2.70
YIG	5.17
GGG	7.08

Table 9.3: Material parameter used for the simulation with the software SRIM2013 [ZZB08].

and (b)]. In consequence we had a periodic array of stripes in the large part of the YIG film. But on the surface of the YIG film we might still had a two dimensional lattice. Therefore we observed MGC modes with a large signal strength of the reciprocal lattice vectors associated with the periodicity of 400 nm and obtained only a weak signal of the reciprocal lattice vectors associated with the periodicity of 100 nm.
Now we discuss the MGC effect in combination with the PSSW mode of the YIG film. As already stated we observed that the wave vector of the PSSW mode of first order (p = 1) added up with the reciprocal lattice vector with $\mathbf{k} = \mathbf{k}_\mathrm{I} + \mathbf{k}_\mathrm{MGC} + \boldsymbol{\kappa}_\mathrm{p}$. The wave vector k_MGC indicates an arbitrary reciprocal lattice vector and was located in-plane just as k_I. The wave vector κ_p for the PSSW pointed out-of-plane.

We suggest that this effect also applies for PSSW modes of higher order (p = 2,3,...) with $\kappa_\mathrm{p} = p\pi/t$. By going to higher order PSSW modes one can drastically reduce the angular dependence of the frequency for an in-plane magnetic field. In Fig. 9.8 (a) we depict the dispersion relation for an in-plane wave vector assuming a fundamental SW (p = 0) and a PSSW mode (p = 7) in 200 nm YIG thin film for $\theta = 0$ deg and $\theta = 90$ deg at an external magnetic field of 1 mT. The calculated angular frequency dependence for PSSWs with p = 7 is reasonable smaller than for fundamental SWs with p = 0. Further the PSSW mode with p = 7 shows only a small angular dependence of the SW group velocity [Fig. 9.8 (b)]. Therefore higher order PSSW modes in combination with the MGC effect can be used to provide SWs with a small wavelength that show only small dependence on the direction of the external magnetic field in the sample plane. This is particular interesting for the use in Mach-Zehnder-type SW interferometer or for guiding SWs with the external magnetic field in the sample plane [LK08, Sch13, KPB$^+$14, VSJ$^+$12, CVS$^+$11]. Nevertheless we assume that the detection of a PSSW mode with p = 7 is challenging, because the induced voltage in the CPW might be small.

9.5 Conclusion

In this chapter we have shown that it is possible to nanostructure a ferrimagnetic material with the HIM. We observed different MGC modes for the fundamental SW mode (p = 0) with a wavelength down to 80 nm. We

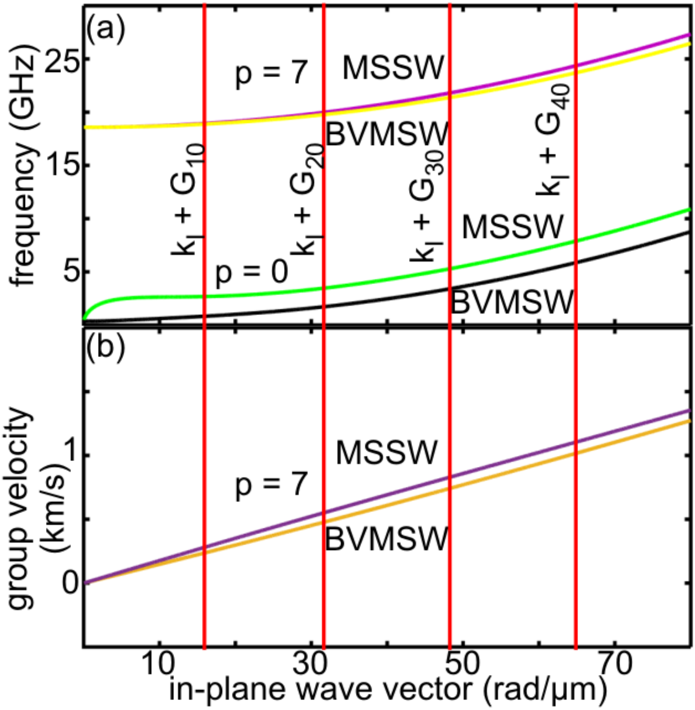

Figure 9.8: (a) Calculated dispersion relation for an in-plane wave vector following Ref. [KS86] assuming a fundamental SW ($p = 0$) and a PSSW mode ($p = 7$). (b) Calculated group velocity following Ref. [KS86] for the PSSW mode $p = 7$. We used an external magnetic field of 1 mT and the same magnetic parameters as in chapter 7. The red lines indicate the wave vector of different MGC modes assuming a lattice constant of 400 nm.

could further show that the MGC effect also modified the SW spectrum of the PSSW mode of first order ($p = 1$). This observation is intriguing. By using PSSWs in combination with the MGC effect the angular dependence of the SW frequency on the direction of the external magnetic field in the sample plane can be reduced. Thus the combination of PSSW mode and MGC effect can be used to provide SWs with small wavelength that show only small dependence of the group velocity on the direction of the external magnetic field. This might be interesting for future use in Mach-Zehnder-type SW interferometer or for guiding SWs with the external magnetic field in the sample plane.

10 Summary and outlook

Within the scope of this thesis YIG films of different thickness were investigated. The samples consisted of bare YIG films or were nanostructured using electron beam lithography and helium ion microscopy. In case of electron beam lithography we fabricated magnetic nanodisks arranged in a square lattice. Using helium ion microscopy we manufactured columnar crystal lattice distortions arranged in a rectangular lattice. We applied the experimental techniques broadband spin wave spectroscopy and micro-focused Brillouin light scattering to investigate the samples. To obtain microscopic insight we used micro-magnetic simulations.

We analyzed a 20 nm thick yttrium iron garnet film using similar preparation and experimental techniques as already reported in literature. The yttrium iron garnet film was fabricated with pulsed laser deposition and nanostructured using electron beam lithography. We resolved magnonic grating-coupler modes. But although the yttrium iron garnet film exhibited the lowest Gilbert damping found up to now, we did not resolve propagating SWs. But the yttrium iron garnet film exhibited an increased linewidth at zero magnetic field compared to YIG films reported in literature. We concluded the linewidth at zero magnetic field limited the propagation of SWs.

To gain microscopic understanding of the recently found magnonic grating-coupler effect, we applied micro-magnetic simulations. Using periodic boundary conditions we were able to model magonic grating-coupler modes. In simulations we observed the wavefront of the magnonic grating-coupler mode and extracted the wavelength. We showed that the wavelength of the observed magnonic grating-coupler mode corresponded to the lattice constant of the simulated structure. Therefore the magnonic grating-coupler effect was consistent with the geometry provided by the periodic modulation of the magnetic parameters. We further showed that beside the magnonic grating-coupler mode the resonant magnonic grating-coupler mode occurred in simulations. The micro-magnetic simulations substantiated the recent experiments attributed to the magnonic grating-coupler effect with spin waves.

To study the magnonic grating-coupler effect also in experiment we used a yttrium iron garnet film grown with liquid phase epitaxy. Previously yttrium iron garnet films commercially grown with liquid phase epitaxy had a thickness above 1 μm. The thickness of the yttrium iron garnet film we applied amounted to 200 nm and was grown at wafer scale. We characterized the bare yttrium iron garnet film and found small damping $\alpha = 1.0 \cdot 10^{-4}$. We further observed a large decay length $l_\mathrm{d} = 0.86$ mm, a group velocity up to 5.4 km/s and a large nonreciprocity $\beta = 0.9$. The group velocity decreased with decreasing wavelength, not suitable for future applications. By adding a periodic lattice of magnetic nanodisks composed of Permalloy to the yttrium iron garnet film we overcame this problem. Due to the large wave vector induced by the magnetic lattice we entered the regime of dipole-exchange SWs. In this regime the group velocity increased with decreasing wavelength. We observed wavelengths down to 110 nm with group velocities of up to 1 km/s. The SWs were detected over a distance of up to 86 μm. We further showed that the detection efficiency of the coplanar waveguide was enhanced for magnonic grating-coupler modes if the exciting coplanar waveguide and the detecting coplanar waveguide had the same emission characteristic. With μBLS we showed experimentally the difference between the magnonic grating-coupler mode and the resonant magnonic grating-coupler mode on the microscale.

In the scope of this work we exploited helium ion microscopy for nanostructuring of the yttrium iron garnet thin film. With the helium ion microscopy we induced columnar crystal lattice distortions in the yttrium iron garnet film to periodically modulate the magnetic parameters of the yttrium iron garnet film. We showed that the lattice induced magnonic grating-coupler modes. We found SWs with wavelengths down to 80 nm. Further we showed the magnonic grating-coupler effect was effective also for the PSSW of first order ($p = 1$). Using PSSW modes of higher order ($p = 2, 3, ...$) in combination with the magnonic grating-coupler effect reduces in theoretical calculations the angular dependency of the spin wave frequency on the direction of the external magnetic field in the sample plane. Using this approach might lead to spin waves with small wavelength and small angular dependence of the spin wave group velocity. This might be interesting for future use in Mach-Zehnder-type spin wave interferometer for guiding spin waves in the sample plane.

In the experiments conducted within this thesis we could not resolve propagating magnonic grating-coupler modes in lattices fabricated with the helium ion microscopy. But propagating SWs are indispensable. Therefore fabricating lattices with the helium ion microscopy has to be further investigated. For future experiments the author suggests to use smaller doses for the helium ion microscopy. The high doses used throughout this thesis verified that the SWs are modified by nanostructuring with the helium ion microscopy. To generate propagating spin waves we suggest to use smaller doses which might be advantageous. Using a smaller dose might reduce the local crystal lattice distortions of the yttrium iron garnet film induced by the helium ion microscope and less helium ions are implemented. We assume this might be favorable for spin wave propagation.

Bibliography

[Aha00] A. Aharoni. *Introduction to the Theory of Ferromagnetism*. Clarendon Press, 2000.

[AM99] R. Arias and D.L. Mills. Extrinsic contributions to the ferromagnetic resonance response of ultrathin films. *Phys. Rev. B*, 60(10):7395, 1999.

[ASG97] D. Anderson, L. Smith, and J. Gruszynski. S-parameter techniques for faster, more accurate network design. *Hewlett Packard, application note 95-1 edn.*, 1997.

[Bet41] A. Bethe. Minutes of the washington, dc, meeting may 1-3, 1941. *Phys. Rev.*, 59:913–945, 1941.

[BG] D. V. Berkov and N. L. Gorn. Micromagus, software for micromagnetic simulations.

[Bil07] C. Bilzer. *Microwave susceptibility of thin ferromagnetic films: metrology and insight into magnetization dynamics*. PhD thesis, Université Paris Sud-Paris 11, 2007.

[BOF03] M. Bailleul, D. Olligs, and C. Fermon. Propagating spin wave spectroscopy in a permalloy film: A quantitative analysis. *Appl. Phys. Lett.*, 83(5):972–974, 2003.

[BOFD01] M. Bailleul, D. Olligs, C. Fermon, and S.O. Demokritov. Spin waves propagation and confinement in conducting films at the micrometer scale. *Europhys. Lett.*, 56(5):741, 2001.

[CGE$^+$17] M. Collet, O. Gladii, M. Evelt, V. Bessonov, L. Soumah, P. Bortolotti, S.O. Demokritov, Y. Henry, V. Cros, M. Bailleul, V.E. Demidov, and A. Anane. Spin-wave propagation in ultra-thin YIG based waveguides. *Appl. Phys. Lett.*, 110(9):092408, 2017.

[Chi99] S. Chikazumi. Magnetism-from fundamentals to nanoscale dynamics, 1999.

[CKD+04] G. Counil, J.V. Kim, T. Devolder, C. Chappert, K. Shigeto, and Y. Otani. Spin wave contributions to the high-frequency magnetic response of thin films obtained with inductive methods. *J. Appl. Phys.*, 95(10):5646–5652, 2004.

[CLZ+14] H. Chang, P. Li, W. Zhang, T. Liu, A. Hoffmann, L. Deng, and M. Wu. Nanometer-thick yttrium iron garnet films with extremely low damping. *IEEE Magn. Lett.*, 5:1–4, 2014.

[CSHK08] A.V. Chumak, A.A. Serga, B. Hillebrands, and M.P. Kostylev. Scattering of backward spin waves in a one-dimensional magnonic crystal. *Appl. Phys. Lett.*, 93(2):022508, 2008.

[CST] *CST Microwave Studio 2014, CST Computer Simulation Technology, www.cst.com.*

[CTK+10] A.V. Chumak, V.S. Tiberkevich, A.D. Karenowska, A.A. Serga, J.F. Gregg, A.N. Slavin, and B. Hillebrands. All-linear time reversal by a dynamic artificial crystal. *Nat. Commun.*, 1:141, 2010.

[CVS+11] P. Clausen, K. Vogt, H. Schultheiss, S. Schäfer, B. Obry, G. Wolf, P. Pirro, B. Leven, and B. Hillebrands. Mode conversion by symmetry breaking of propagating spin waves. *Appl. Phys. Lett.*, 99(16):162505, 2011.

[CVSH15] A.V. Chumak, V.I. Vasyuchka, A.A. Serga, and B. Hillebrands. Magnon spintronics. *Nat. Phys.*, 11:453, 2015.

[CVvWY12] V. Castel, N. Vlietstra, B.J. van Wees, and J.B. Youssef. Frequency and power dependence of spin-current emission by spin pumping in a thin-film YIG/Pt system. *Phys. Rev. B*, 86(13):134419, 2012.

[DD08] S.O. Demokritov and V.E. Demidov. Micro-brillouin light scattering spectroscopy of magnetic nanostructures. *IEEE Trans. Magn.*, 44(1):6–12, 2008.

[DDH+04] V.E. Demidov, S.O. Demokritov, B. Hillebrands, M. Laufenberg, and P.P. Freitas. Radiation of spin waves by a single micrometer-sized magnetic element. *Appl. Phys. Lett.*, 85(14):2866–2868, 2004.

[DE61] R.F.W. Damon and J.R. Eshbach. Magnetostatic modes of a ferromagnet slab. *J. Phys. Chem. Solids*, 19(3-4):308–320, 1961.

[DHS01] S.O. Demokritov, B. Hillebrands, and A.N. Slavin. Brillouin light scattering studies of confined spin waves: linear and nonlinear confinement. *Phys. Rep.*, 348(6):441–489, 2001.

[dKAB+13] O. d'Allivy Kelly, A. Anane, R. Bernard, J.B. Youssef, C. Hahn, A. H. Molpeceres, C. Carrétéro, E. Jacquet, C. Deranlot, P. Bortolotti, et al. Inverse spin hall effect in nanometer-thick yttrium iron garnet/Pt system. *Appl. Phys. Lett.*, 103(8):082408, 2013.

[DKR+09] V.E. Demidov, M.P. Kostylev, K. Rott, P. Krzysteczko, G. Reiss, and S.O. Demokritov. Excitation of microwaveguide modes by a stripe antenna. *Appl. Phys. Lett.*, 95(11):112509, 2009.

[DMN+11] G. Duerr, M. Madami, S. Neusser, S. Tacchi, G. Gubbiotti, G. Carlotti, and D. Grundler. Spatial control of spin-wave modes in $Ni_{80}Fe_{20}$ antidot lattices by embedded co nanodisks. *Appl. Phys. Lett.*, 99(20):202502, 2011.

[DSL+17] C. Dubs, O. Surzhenko, R. Linke, A. Danilewsky, U. Brückner, and J. Dellith. Sub-micrometer yttrium iron garnet LPE films with low ferromagnetic resonance losses. *J. Phys. D: Appl. Phys.*, 50(20):204005, 2017.

[Dür12] G.F. Dürr. *Spin Waves in Nanochannels, Created by Individual and Periodic Bi-Component Ferromagnetic Devices*. PhD thesis, Technische Universität München, 2012.

[DVHVDA81] J.G. Dil, N.C.J.A. Van Hijningen, F. Van Dorst, and R.M. Aarts. Tandem multipass fabry-perot interferometer for brillouin scattering. *Applied Optics*, 20(8):1374–1381, 1981.

[EP59] D. T. Edmonds and R. G. Petersen. Effective exchange constant in yttrium iron garnet. *Phys. Rev. Lett.*, 2:499–500, Jun 1959.

[EWKW12] M.M. Eshaghian-Wilner, A. Khitun, and K.L. Wang. Spin-wave architectures. *US Patent*, 8,193,598:B2, June 5 2012.

[GG58] M.A. Gilleo and S. Geller. Magnetic and crystallographic properties of substituted yttrium-iron garnet, $3\mathrm{Y}_2\mathrm{O}_3 \cdot x\mathrm{M}_2\mathrm{O}_3 \cdot (5-x)\mathrm{Fe}_2\mathrm{O}_3$. *Phys. Rev.*, 110(1):73, 1958.

[Gie05] F. Giesen. *Magnetization dynamics of nanostructured ferromagnetic rings and rectangular elements*. PhD thesis, Universität Hamburg, 2005.

[Gil55] T.L. Gilbert. A lagrangian formulation of the gyromagnetic equation of the magnetization field. *Phys. Rev.*, 100:1243, 1955.

[Gil04] T.L. Gilbert. A phenomenological theory of damping in ferromagnetic materials. *IEEE Trans. Magn.*, 40(6):3443–3449, 2004.

[GKFK15] F. Gertz, A. Kozhevnikov, Y. Filimonov, and A. Khitun. Magnonic holographic memory. *IEEE Trans. Magn.*, 51(4):1–5, 2015.

[GM96] A.G. Gurevich and G.A. Melkov. *Magnetization Oscillations and Waves*. CRC Press, 1996.

[Grü89] P. Grünberg. Light scattering from spin waves in thin films and layered magnetic structures. In *Light Scattering in Solids V*, pages 303–305. Springer, 1989.

[GZG$^+$00] I. Guedes, N.J. Zaluzec, M. Grimsditch, V. Metlushko, P. Vavassori, B. Ilic, P. Neuzil, and R. Kumar. Magnetization of negative magnetic arrays: Elliptical holes on a square lattice. *Phys. Rev. B*, 62(17):11719, 2000.

[HBM⁺11] B. Heinrich, C. Burrowes, E. Montoya, B. Kardasz, E. Girt, Y.Y. Song, Y. Sun, and M. Wu. Spin pumping at the magnetic insulator (YIG)/normal metal (Au) interfaces. *Phys. Rev. Lett.*, 107:066604, Aug 2011.

[HD94] F. Hansen and W.W. Duley. Attenuation of laser radiation by particles during laser materials processing. *J. Laser Appl.*, 6(3):137–143, 1994.

[Hil00] B. Hillebrands. Brillouin light scattering from layered magnetic structures. In *Light scattering in Solids VII*, pages 174–289. Springer, 2000.

[HNS12] R. Hill, J.A. Notte, and L. Scipioni. Scanning helium ion microscopy. *Adv. Imag. Elec. Phys.*, 170:65, 2012.

[HNW08] R. Hill, J. Notte, and B. Ward. The ALIS He ion source and its application to high resolution microscopy. *Phys Procedia*, 1(1):135–141, 2008.

[HRH⁺16] C. Hauser, T. Richter, N. Homonnay, C. Eisenschmidt, M. Qaid, H. Deniz, D. Hesse, M. Sawicki, S.G. Ebbinghaus, and G. Schmidt. Yttrium iron garnet thin films with very low damping obtained by recrystallization of amorphous material. *Sci. Rep.*, 6:20827, 2016.

[HS98] A. Hubert and R. Schäfer. *Magnetic domains: the analysis of magnetic microstructure*. Springer, Berlin, 1998.

[HSG13] R. Huber, T. Schwarze, and D. Grundler. Nanostripe of subwavelength width as a switchable semitransparent mirror for spin waves in a magnonic crystal. *Phys. Rev. B*, 88(10):100405, 2013.

[Hub13] Rupert Huber. *Control of spin waves on the nanoscale in one-dimensional magnonic crystals and atomic layer deposition of metallic ferromagnets for second generation of nanomaterials*. PhD thesis, Technische Universität München, 2013.

[HVvGP14] G. Hlawacek, V. Veligura, R. van Gastel, and B. Poelsema. Helium ion microscopy. *J. Vac. Sci. Technol. B*, 32(2):020801, 2014.

[Jac60] P. Jacquinot. New developments in interference spectroscopy. *Reports on progress in physics*, 23(1):267, 1960.

[JKS+13] M. Jamali, J.H. Kwon, S.M. Seo, K.J. Lee, and H. Yang. Spin wave nonreciprocity for logic device applications. *Sci. Rep.*, 3:3160, 2013.

[JZJ+15] M.B. Jungfleisch, W. Zhang, W. Jiang, H. Chang, J. Sklenar, S.M. Wu, J.E. Pearson, A. Bhattacharya, J.B. Ketterson, M. Wu, and A. Hoffmann. Spin waves in microstructured yttrium iron garnet nanometer-thick films. *J. Appl. Phys.*, 117(17):17D128, 2015.

[KBBG02] B.K. Kuanr, M. Buchmeier, D.E. Bürgler, and P. Grünberg. Exchange coupling of molecular-beam-epitaxy-grown Fe/Al/Fe trilayers by dynamic techniques. *J. Appl. Phys.*, 91(10):7209–7211, 2002.

[KBL+08] A. Khitun, M. Bao, J.Y. Lee, K.L. Wang, D.W. Lee, S.X. Wang, and I.V. Roshchin. Inductively coupled circuits with spin wave bus for information processing. *J. Nanoelectron. Optoe.*, 3(1):24–34, 2008.

[KBW+08] A. Khitun, M. Bao, Y. Wu, J.Y. Kim, A. Hong, A. Jacob, K. Galatsis, and K.L. Wang. Spin wave logic circuit on silicon platform. In *Information Technology: New Generations, 2008. ITNG 2008. Fifth International Conference on*, pages 1107–1110. IEEE, 2008.

[KBW10] A. Khitun, M. Bao, and K.L. Wang. Magnonic logic circuits. *J. Phys. D: Appl. Phys.*, 43(26):264005, 2010.

[KGK+17] A. Krysztofik, H. Glowinski, P. Kuswik, S. Zietek, L.E. Coy, J.N. Rychly, S. Jurga, T.W. Stobiecki, and J Dubowik. Characterization of spin wave propagation in (111) YIG thin films with large anisotropy. *J. Phys. D: Appl. Phys.*, 50(23), 2017.

[Kit48] C. Kittel. On the theory of ferromagnetic resonance absorption. *Phys. Rev.*, 73(2):155, 1948.

[Kit05] C. Kittel. *Introduction to solid state physics*. Wiley, 2005.

[KNB$^+$07] A. Khitun, D.E. Nikonov, M. Bao, K. Galatsis, and K.L. Wang. Feasibility study of logic circuits with a spin wave bus. *Nanotechnol.*, 18(46):465202, 2007.

[KOW02] A. Khitun, R. Ostroumov, and K.L. Wang. Feasibility study of the spin wave quantum network. In *Proceedings of SPIE*, volume 5023, pages 449–451, 2002.

[KP75] V. Kambersky and C.E. Patton. Spin-wave relaxation and phenomenological damping in ferromagnetic resonance. *Phys. Rev. B*, 11(7):2668, 1975.

[KPB$^+$14] S. Klingler, P. Pirro, T. Brächer, B. Leven, B. Hillebrands, and A.V. Chumak. Design of a spin-wave majority gate employing mode selection. *Appl. Phys. Lett.*, 105(15):152410, 2014.

[KS86] B.A. Kalinikos and A.N. Slavin. Theory of dipole-exchange spin wave spectrum for ferromagnetic films with mixed exchange boundary conditions. *J. Phys. C: Solid State Phys.*, 19(35):7013, 1986.

[KWG60] J.E. Kunzler, L.R. Walker, and J.K. Galt. Adiabatic demagnetization and specific heat in ferrimagnets. *Phys. Rev.*, 119:1609–1614, Sep 1960.

[LAS81] S.M. Lindsay, M.W. Anderson, and J.R. Sandercock. Construction and alignment of a high performance multipass vernier tandem fabry–perot interferometer. *Review of scientific instruments*, 52(10):1478–1486, 1981.

[LK08] Ki Suk Lee and Sang Koog Kim. Conceptual design of spin wave logic gates based on a mach–zehnder-type spin wave interferometer for universal logic functions. *J. Appl. Phys.*, 104(5):053909, 2008.

[LKB$^+$16] L.V. Lutsev, A.M. Korovin, V.E. Bursian, S.V. Gastev, V.V. Fedorov, S.M. Suturin, and N.S. Sokolov. Low-relaxation spin waves in laser-molecular-beam epitaxy grown nanosized yttrium iron garnet films. *Appl. Phys. Lett.*, 108(18):182402, 2016.

[LL35] L. Landau and E. Lifshitz. On the theory of the dispersion of magnetic permeability in ferromagnetic bodies. *Phys. Z. Sowjetunion*, 8(153):101–114, 1935.

[LSP$^+$12] G. Lorusso, J.W. Sharples, E. Palacios, O. Roubeau, E.K. Brechin, R. Sessoli, A. Rossin, F. Tuna, E.J.L. McInnes, D. Collison, and Evangelisti M. Magnetic cryocooling with Gd^{3+} centers in a light and compact framework. *arXiv:1212.2877*, 2012.

[Mat] Matesy GmbH, Otto-Schott-Str. 13, 07745 Jena, Germany.

[MAT02] J. Miltat, G. Albuquerque, and A. Thiaville. An introduction to micromagnetics in the dynamic regime. in B. Hillebrands and K. Ounadjela, editors, Spin Dynamics in Confined Magnetic Structures I. *Spin Dynamics in Confined Magnetic Structures I*, pages 1–33, 2002.

[Mav96] R. Mavaddat. *Network scattering parameters*, volume 2. World Scientific, 1996.

[MVC$^+$06] G.A. Melkov, V.I. Vasyuchka, A.V. Chumak, V.S. Tiberkevich, and A.N. Slavin. Wave front reversal of nonreciprocal surface dipolar spin waves. *J. Appl. Phys.*, 99(8):08P513, 2006.

[NBB$^+$08] S. Neusser, B. Botters, M. Becherer, D. Schmitt-Landsiedel, and D. Grundler. Spin-wave localization between nearest and next-nearest neighboring holes in an antidot lattice. *Appl. Phys. Lett.*, 93(12):122501, 2008.

[NDB$^+$10] S. Neusser, G. Duerr, H.G. Bauer, S. Tacchi, M. Madami, G. Woltersdorf, G. Gubbiotti, C.H. Back, and D. Grundler. Anisotropic propagation and damping of spin waves in a nanopatterned antidot lattice. *Phys. Rev. Lett.*, 105(6):067208, 2010.

[NDT$^+$11] S Neusser, G Duerr, S Tacchi, M Madami, ML Sokolovskyy, G Gubbiotti, Maciej Krawczyk, and D Grundler. Magnonic minibands in antidot lattices with large spin-wave propagation velocities. *Physical Review B*, 84(9):094454, 2011.

[Neu11] S. Neusser. *Spin waves in antidot lattices: From quantization to magnonic crystals*. PhD thesis, Technische Universität München, 2011.

[NTT01] S.A. Nikitov, P. Tailhades, and C.S. Tsai. Spin waves in periodic magnetic structures–magnonic crystals. *J. Magn. Magn. Mater.*, 236(3):320–330, 2001.

[Pol48] D. Polder. On the quantum theory of ferromagnetic resonance. *Phys. Rev.*, 73(9):1116, 1948.

[RGJ09] R. Ramachandra, B. Griffin, and D. Joy. A model of secondary electron imaging in the helium ion scanning microscope. *Ultramicroscopy*, 109(6):748–757, 2009.

[SCA$^+$07] A.A. Serga, A.V. Chumak, A. Andre, G.A. Melkov, A.N. Slavin, S.O. Demokritov, and B. Hillebrands. Parametrically stimulated recovery of a microwave signal stored in standing spin-wave modes of a magnetic film. *Phys. Rev. lett.*, 99(22):227202, 2007.

[SCH10] A.A. Serga, A.V. Chumak, and B. Hillebrands. YIG magnonics. *J. Phys. D: Appl. Phys.*, 43(26):264002, 2010.

[Sch13] T. Schwarze. *Spin Waves in 2D and 3D Magnonic Crystals: From Nanostructured Ferromagnetic Materials to Chiral Helimagnets*. PhD thesis, Technische Universität München, 2013.

[Sim01] R.N. Simons. Coplanar waveguide circuits, components, and systems. *John Wiley & Sons, New York*, 2001.

[Sla34] J.C. Slater. Electronic energy bands in metals. *Phys. Rev.*, 45(11):794, 1934.

[SLCR99] T.J. Silva, C.S. Lee, T.M. Crawford, and C.T. Rogers. Inductive measurement of ultrafast magnetization dynamics in thin-film permalloy. *J. Appl. Phys.*, 85(11):7849–7862, 1999.

[SPS88] W. Stoecklein, S.S.P. Parkin, and J.C. Scott. Ferromagnetic resonance studies of exchange-biased permalloy thin films. *Phys. Rev. B*, 38(10):6847, 1988.

[SSC$^+$12] Y. Sun, Y.Y. Song, H. Chang, M. Kabatek, M. Jantz, W. Schneider, M. Wu, H. Schultheiss, and A. Hoffmann. Growth and ferromagnetic resonance properties of nanometer-thick yttrium iron garnet films. *Appl. Phys. Lett.*, 101(15):152405, 2012.

[SSO$^+$15] T. Sebastian, K. Schultheiss, B. Obry, B. Hillebrands, and H. Schultheiss. Micro-focused Brillouin light scattering: imaging spin waves at the nanoscale. *Front Phys.*, 3:35, 2015.

[Sta93] D.D. Stancil. *Theory of magnetostatic waves*. Springer, New York, 1993.

[SYS$^+$10] K. Sekiguchi, K. Yamada, S.M. Seo, K.J. Lee, D. Chiba, K. Kobayashi, and T. Ono. Nonreciprocal emission of spin-wave packet in FeNi film. *Appl. Phys. Lett.*, 97(2):022508, 2010.

[TDS$^+$17] A. Talalaevskij, M. Decker, J. Stigloher, A. Mitra, H.S. Körner, O. Cespedes, C.H. Back, and B.J. Hickey. Magnetic properties of spin waves in thin yttrium iron garnet films. *Phys. Rev. B*, 95(6):064409, 2017.

[THKG10] J. Topp, D. Heitmann, M.P. Kostylev, and D. Grundler. Making a reconfigurable artificial crystal by ordering bistable magnetic nanowires. *Phys. Rev. lett.*, 104(20):207205, 2010.

[VB10] V. Vlaminck and M. Bailleul. Spin-wave transduction at the submicrometer scale: Experiment and modeling. *Phys. Rev. B*, 81(1):014425, 2010.

[VSJ+12] K. Vogt, H. Schultheiss, S. Jain, J.E. Pearson, A. Hoffmann, S.D. Bader, and B. Hillebrands. Spin waves turning a corner. *Appl. Phys. Lett.*, 101(4):042410, 2012.

[Wal57] L.R. Walker. Magnetostatic modes in ferromagnetic resonance. *Phys. Rev.*, 105(2):390, 1957.

[WO90] Y.C. Wang and J.A. Okoro. Impedance calculations for modified coplanar waveguides. *Int. J. Electron.*, 68(5):861–875, 1990.

[WZL+09] Z.K. Wang, V.L. Zhang, H.S. Lim, S.C. Ng, M.H. Kuok, S. Jain, and A.O. Adeyeye. Observation of frequency band gaps in a one-dimensional nanostructured magnonic crystal. *Appl. Phys. Lett.*, 94(8):083112, 2009.

[YDH+13] H. Yu, G. Duerr, R. Huber, M. Bahr, T. Schwarze, F. Brandl, and D. Grundler. Omnidirectional spin-wave nanograting coupler. *Nat. Commun.*, 4:3702, 2013.

[YdKC+14] H. Yu, O. d'Allivy Kelly, V. Cros, R. Bernard, P. Bortolotti, A. Anane, F. Brandl, R. Huber, I. Stasinopoulos, and D. Grundler. Magnetic thin-film insulator with ultralow spin wave damping for coherent nanomagnonics. *Sci. Rep.*, 4:6848, 2014.

[YdKC+16] H. Yu, O. d'Allivy Kelly, V. Cros, R. Bernard, P. Bortolotti, A. Anane, F. Brandl, F. Heimbach, and D. Grundler. Approaching soft x-ray wavelengths in nanomagnet-based microwave technology. *Nat. Commun.*, 7:11255, 2016.

[YHS+12] H. Yu, R. Huber, T. Schwarze, F. Brandl, T. Rapp, P. Berberich, G. Duerr, and D. Grundler. High propagating velocity of spin waves and temperature dependent damping in a CoFeB thin film. *Appl. Phys. Lett.*, 100(26):262412, 2012.

[ZZB08] J.F. Ziegler, M.D. Ziegler, and J.P. Biersack. *SRIM: the stopping and range of ions in matter*. Cadence Design Systems, 2008.

Publications

- I. Stasinopoulos, S. Weichselbaumer, A. Bauer, J. Waizner, H. Berger, S. Maendl, M. Garst, C. Pfleiderer and D. Grundler: Low spin wave damping in the insulating chiral magnet $\mathrm{Cu_2OSeO_3}$, Appl. Phys. Lett. **111**, 032408 (2017)
- S. Maendl, I. Stasinopoulos and D. Grundler: Spin waves with large decay length and few 100 nm wavelenghts in thin yttrium iron garnet grown at the wafer scale, Appl. Phys. Lett. **111**, 012403 (2017)
- K. Baumgaertl, F. Heimbach, S. Maendl, D. Rueffer, A. Fontcuberta i Morral and D. Grundler: Magnetization reversal in individual Py and CoFeB nanotubes locally probed via anisotropic magnetoresistance and anomalous Nernst effect, Appl. Phys. Lett. **108**, 132408 (2016)

Acknowledgments

I would like to express my gratitude to all people who contributed with their knowledge and know-how to the success of this thesis. In particular:

- Prof. Dr. Frank Pollmann for the supervision of my examination, Prof. Dr. Dirk Grundler for being first examiner, Prof. Dr. Peter Böni for being second examiner and Priv.-Doz. Dr. Christoph P. Hugenschmidt for being second examiner in the oral exam.

- Prof. Dr. Dirk Grundler for giving me the opportunity to do research at the chair E10, many intense discussions and a lot of helpful advices.

- Ioannis Stasinopoulos for experimental support, fruitful discussions and providing simulations obtained with CST microwave studio.

- Dr. Marc Wilde for many helpful advices.

- All members of the E10 group for support and great working atmosphere: Schorsch Sauther, Florian Heimbach, Florian Brandl, Thomas Schwarze, Korbinian Baumgärtl, Florian Herzog, Stephan Albert, Matthias Brasse, Stefanos Chalkidis, Rupert Huber, Arthur Niedermayr, Johannes Mendil, Filip Lisiecki, Markus Kleinhans, Dr. Vinayak Bhat and Dr. Haiming Yu.

- Thomas Rapp, Thomas Neukel, Stephan Lichtenauer and Johannes Seitz for continuous technical support.

- Claudine Völcker for organizational support.

- Prof. Dr. Georg Schmidt and Christoph Hauser for providing high quality Yittrium Iron Garnet films.

- Prof. Dr. Alexander Holleitner and Peter Weiser for providing all the facilities needed for nanostructuring.

- Paul Seifert and Marcus Altzschner for supporting the sample fabrication with the helium ion microscope.
- Dr. Vladislav Demidov for building up the Brillouin light scattering setup and continuous support when problems occurred.
- Last but not least I thank my family and friends for their support and encouragement.

The funding used for the research of this thesis has been received from the DFG via GR1640/5-2 in the SPP 1538, the Cluster of Excellence "Nanosystems Initiative Munich" and TRR80 (From Electronic Correlations to Functionality). The funding is gratefully acknowledged. I acknowledge the support of CST microwave studio.